

**Materials: Technology and
Applications
Series 1**

Materials : Technology and Applications Series 1

EDITOR:

**MAZATUSZIHA BINTI AHMAD
NUR HANIS HAYATI BINTI HAIROM
SITI AMIRA BINTI OTHMAN**



©Penerbit UTHM
First Published 2019

Copyright reserved. Reproduction of any articles, illustrations and content of this book in any form be it electronic, mechanical photocopy, recording or any other form without any prior written permission from The Publisher's Office of Universiti Tun Hussein Onn Malaysia, Parit Raja, Batu Pahat, Johor is prohibited. Any negotiations are subjected to calculations of royalty and honorarium.

Perpustakaan Negara Malaysia

Cataloguing in Publication Data

Materials : Technology and Applications. Series 1 / EDITOR:MAZATUSZIHA BINTI AHMAD, NUR HANIS HAYATI BINTI HAIROM, SITI AMIRA BINTI OTHMAN.

ISBN 978-967-2389-09-5

1. Materials.

2. Technology.

3. Government publications--Malaysia.

I. Mazatusziha Ahmad.

II. Nur Hanis Hayati Hairom.

III. Siti Amira Othman.

620.11

Published by:
Penerbit UTHM
Universiti Tun Hussein Onn Malaysia
86400 Parit Raja,
Batu Pahat, Johor
Tel: 07-453 7051
Fax: 07-453 6145

Website: <http://penerbit.uthm.edu.my>

E-mail: pt@uthm.edu.my

<http://e-bookstore.uthm.edu.my>

Penerbit UTHM is a member of
Majlis Penerbitan Ilmiah Malaysia
(MAPIM)

CONTENTS

PREFACE		vii
CHAPTER 1	Tensile and Thermogravimetry Analysis of Pullulan/Cellulose Films Incorporated with Carica Papaya Seeds Extract. <i>Naz Suzieha Wan Long, Mazatusziha Ahmad, Nur Hanis Hayati Hairom</i>	1
CHAPTER 2	Polyurethane Material for Synthetic Tibia Bone Application <i>Siti Adawiyah Zulkefli, Maryam Hanim Mohamad Shaikhan, Ahmad Kafrawi Nasution, Gan Hong Seng, Muhammad Hanif Ramlee</i>	20
CHAPTER 3	The Effect of Polyethylene Glycol on Precipitation of Zinc Oxide Nanoparticles for Photocatalytic Degradation of Dye <i>Nur Hanis Hayati Hairom, Abdul Wahab Mohammad</i>	37
CHAPTER 4	Materials Processing and Characterization in Biodegradable Implants Development <i>Ahmad Kafrawi Nasution, Abdul Hakim Md Yuso, Muhammad Hanif Ramlee</i>	61
CHAPTER 5	Characterization of Nitrogen and Magnesium Doped with Titanium Dioxide at Different Calcination Temperature using X-ray Diffraction (XRD) <i>Nur' Aliaa Razali and Siti Amira Othman</i>	88
CHAPTER 6	On The Mechanical Behaviour of Hyperelastic Functionally Graded Polymer <i>Ahmad Wisnu Sulaiman,, Mohd Ayub</i>	97

Sulong

CHAPTER 7	A Comprehensive Review of Collagen Scaffold in Musculoskeletal Tissue Engineering <i>Mohd Syahir Anwar Hamzah, Syuhaimi Yusof, Syahirah Mohd Noor, Saiful Izwan Abd Raza and Nadirul Hasraf Mat Nayan</i>	119
CHAPTER 8	Hydroxyapatite in Bone Tissue Applications <i>Norhana Jusoh</i>	153
CHAPTER 9	Different Materials of Implant Affecting The Biomechanics Behaviour of Fibula Fracture : A Finite Element Study <i>Amir Mustakim Ab Rashid, Mohamad Hafiz, Mohamad Afandi, Gan Hong Seng, Mohammed Rafiq Abdul Kadir, Muhammad Hanif Ramlee</i>	169

PREFACE

Materials: Technology and Applications, Series 1 is a comprehensive compilation of chapters on the current research of materials such as polymeric, metals, ceramic and composite materials for various applications. It provide an understanding on the fundamental mechanisms to synthesize the materials, leading to processing, characterization, property evaluation and the technology used. The book will be of great use to students, researchers and practitioners in materials technology field.

Mazatusziha Ahmad

CHAPTER 1

TENSILE AND THERMOGRAVIMETRY ANALYSIS OF PULLULAN/CELLULOSE FILMS INCORPORATED WITH CARICA PAPAYA SEEDS EXTRACT

Naz Suzieha Binti Wan Long¹, Mazatusziha Binti Ahmad¹

¹ Department of Chemical Engineering Technology,
Biotechnology – Sustainable Material Focus Group
(B-SMAT),
Faculty of Engineering Technology,
Universiti Tun Hussein Onn Malaysia,
Pagoh Higher Education Hub,
84600 , Pagoh Muar, Johor, Malaysia.

1.0 ABSTRACT

Pullulan is a non-ionic exopolysaccharide produced by polymorphic fungus known as *Aureobasidium pullulans*. Pullulan have a great potential to be develop as biodegradable food packaging films in order to reduce environmental pollutions and health issues. It has an excellent adhesive properties, high transparency, non-toxicity and heat sealable. However, high cost and high water solubility of pullulan has hindered its widely applications. Therefore, in this study, the pullulan based film was modified with cellulose and *Carica Papaya* seeds extract (CPSE) to improve the properties of the pure pullulan film. The addition of CPSE as antimicrobial agent can improve antimicrobial properties of the films in order to increase the food shelf-life and reduce food spoilage. Three types of films were prepared via casting technique, which are pullulan, pullulan/cellulose and pullulan/cellulose/CPSE. The thermal properties of these films were assessed via Thermo gravimetric Analysis (TGA), observation of film surface morphology by Scanning Electron Microscope (SEM), mechanical properties of films by Universal Testing Machine as well as characterization of films were evaluated by using

Fourier Transform Infrared Spectroscopy (FTIR). The addition of cellulose enhanced the tensile strength of the films and reduces the elongation at break. CPSE have shown no significance changes on the films mechanical properties as its function as antimicrobial agent.

Keywords: food packaging, pullulan, cellulose, papaya seed, antimicrobial

1.1 INTRODUCTION

Recently, the dumping of conventional packaging in disposal area had becoming a serious threat to the global health and environment. Thus, several biopolymers made of pullulan, starch and cellulose have received tremendous attentions by many researchers and industries due to their biodegradable capability to be develop as food packaging applications (Dhall, 2013). Pullulan is such a favourable alternative to replace synthetic based materials because it has an excellent film forming ability, sustainable, good oxygen barrier properties and oil resistant. However, despite of all advantages, it is high cost and highly water soluble, where the films become sticky by absorbing atmospheric moisture (Conca *et al.*, 1993). Thus, those drawbacks have restricted its wider usage to form a pure pullulan film for plastic packaging applications.

Hence, researches have been carried out on blending pullulan based film with other biopolymers such as chitosan (Biliaderis *et al.*, 2002), collagen (Gurtner GC *et al.*, 2011) and cellulose (Ferreira *et al.*, 2016) to improve film properties and more cost effective. Cellulose has been chosen in this study in order to improve the mechanical properties of the pullulan films. According to a study conducted by Eliane Trovatti (2011) who investigated on nanofibrillated cellulose–pullulan composite materials has proved that incorporation of pullulan with cellulose will improve the thermal and mechanical properties of the films.

Besides, special attention also had been given on *Carica Papaya* seeds extract (CPSE) as antimicrobial agent to be used in active food packaging industry. It is rich in phytochemical, especially phenolic compound which has antimicrobial properties, acts as natural antioxidant to extend food shelf-life. Films incorporated with CPSE show a strong antimicrobial activity particularly effective against *E. coli*, *Salmonella* and *Staphylococcus* infections (Mitscher *et al.*, 1992). The pungent and

peppery characteristics of *Carica Papaya* seeds have repressive ability over the metabolic activities of a wide range of microorganism. Thus, it shows a considerable potential as microbial inhibitors in order to maintain food quality and reduce food spoilage.

Thus, in this study, the effects of the addition of cellulose and CPSE into pullulan films were investigated upon the thermal and mechanical properties of films. Three types of films which are pullulan, three different ratios of pullulan/cellulose and pullulan/cellulose/CPSE were prepared via casting technique. These blends films were further characterized in terms of their thermal stabilities and mechanical properties such as Thermo gravimetric Analysis and tensile strength respectively, chemical interaction between the films component were evaluated via Fourier Transform Infrared Spectroscopy (FTIR) and film surface morphology were observed through Scanning Electron Microscope (SEM).

1.2 BIODEGRADABLE BASED MATERIALS FOR ACTIVE FOOD PACKAGING

Accumulation of petroleum based packaging films in the environment are the driving force behind the development of biodegradable materials based active food packaging. Natural compounds, for instance animal and plant-based polysaccharides, biodegradable polymers and proteins are considered as the best alternatives to synthetic polymers (Boredes *et al.*, 2009). Biodegradable polymers are defined as materials where chemical and physical characteristics undergo deterioration and completely degrade upon disposal by the action of living organisms such as microorganisms, aerobic and anaerobic processes. They are made of natural resources such as starch, cellulose and lactic acid. Modern-day food manufacturers not only demands for the food packaging that may improve solid waste disposal but also cost-effective in order to replace conventional plastics.

1.2.1 Active Food Packaging (AFP)

Packaging may be termed active when it performs some desired role in food preservation other than providing an inert barrier to external conditions (Hutton, 2003). AFP is an innovative solution for increasing foodborne diseases and changes in food habits. It refers to the incorporation of certain additives into packaging film or containers with the aim of maintaining and prolonging shelf life (Ahvenainen, 2003). In addition, it also includes additives or freshness enhancers that are capable of adsorbing carbon dioxide, moisture, scavenging oxygen, releasing ethanol, sorbets or other preservatives and temperature control to maximize the shelf-life of food products, delay microbial, enzymatic and oxidative spoilage, minimize contamination, weight loss and to ensure the colour and integrity of the products during storage while ensuring their quality, safety and integrity (Vital *et al.*, 2016; Chong *et al.*, 2015; Kerry *et al.*, 2006).

1.2.2 Pullulan

Pullulan is an extracellular bacterial polysaccharide which is produced from starch by the fungus *Aureobasidium pullulans*. It is biodegradable and easily soluble in water to make clear and viscous solution. Pullulan is a white powder which is edible, tasteless, odourless and thermally stable. It is also particularly low oxygen permeability and has a high stability of various properties over storage such as mechanical and dissolution properties. Despite all of these advantages of pullulan, it is more expensive compared to other polysaccharides which is approximately RM80/kg. Figure 1.1 shows the chemical structure of pullulan.

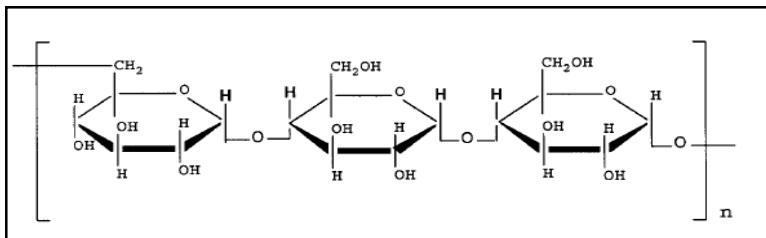


Figure 1.1: Chemical structure of pullulan (Farris *et al.*, 2014)

1.2.3 Cellulose

Cellulose is a polymer of glucose that composed of linear chains of several 100 to over 10000 of β -1,4 linked d-glucose units. It has a good chemical stability, highly crystalline, renewable, odourless and soluble in water. Furthermore, cellulose also possesses many unique morphological aspects which are high specific strength, high aspect ratio, high surface area and unique optical transparency (Bledzki and Gassan, 1999).

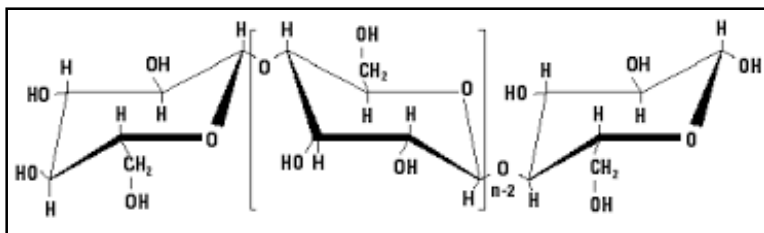


Figure 1.2: Chemical Structure of Cellulose (Brett and Waldron, 1990).

1.2.4 CPSE as Antimicrobial Agent

CPSE rich in phenolic compound which has antimicrobial properties, acts as natural antioxidant to enhance antioxidant function and extend food shelf-life. CPSE has a great potential as the antimicrobial agent to be used in food packaging industry because it have inhibitory effect on *Staphylococcus aureus*, *E. coli*, *Shigella dysentria* and *Salmonella typhi* (Ogunjobi & Elizabeth, 2011). Based on the study conducted by M.Vijayakumar (2015), the higher the concentration of CPSE, the greater diameter of microbial inhibition zone. This antimicrobial property gives advantages in food packaging industry as it acts as preservative, staving off oxidation and prevent spoilage (Mitrus *et al.*, 2010).

1.3 METHODOLOGY

1.3.1 Materials:

Pullulan, cellulose (Sigma Aldrich, Malaysia), Ethanol 95 % and Papaya seed (Malaysia)

1.3.2 *Carica Papaya* seeds extraction

Fresh ripe *Carica papaya* was bought at the fruit stall to get the seeds. The fruit were cut into two and their seeds were put in the beaker for cleaning process. The debris of the seeds was removed and they were dried in the microwave oven at 60 °C. After 3 days (or constant weight), the dry seeds were blend by using an electric blender in order to get the seed powder. Next, 15g of powder was mixed with 200 mL of ethanol 95 % and left for 48 hours. Then, the mixture was filtered by passing through the Whatman no. 1 filter paper. The liquid solution was put in the glass bottle to be used as antimicrobial agent.

1.3.3 Film Preparation

Pullulan based films were formed via casting method by using film applicator. For pure pullulan film, 5.0 g of pullulan was mixed and dispersed in 200ml of water. Next, the step was repeated with the addition of cellulose and CPSE. Table 1.1 and 1.2 show the composition of pullulan/cellulose and CPSE, respectively at different ratios [9:1, 8:2, 7:3 of pullulan/cellulose (w/w)] 8% of CPSE is added based on the percentage of pullulan (g fatty acid per g pullulan). The solution is mixed gently by stirring with a magnetic stir bar until pullulan was dissolved. Then, the solution was homogenized for about 15 minutes with addition of slow heating. Stirring and heating was stopped when the solution reaches temperature of 80 – 86°C. Next, 50ml of the film forming solution was spread evenly onto glass sheet (A4 paper size). The thickness of the films was set on the film applicator (0.25mm) and the films were air-dried at room temperature for three days.

Table 1.1: Percent composition of pullulan and cellulose.

Sample	Pullulan (wt %)	Cellulose (wt %)
PLC10	90	10
PLC20	80	20
PLC30	70	30

Table 1.2: Percent composition of pullulan and cellulose with addition of CPSE.

Sample	Pullulan (wt %)	Cellulose (wt %)	CPSE (wt %)
PLC10C8	90	10	8
PLC20C8	80	20	8
PLC30C8	70	30	8

1.3.4 Thermo gravimetric Analysis (TGA)

Thermo gravimetric testing of films was conducted using TGA 550 at Instrumentation Laboratory, Department of Chemical Engineering Technology in UTHM. 4 mg sample of films was placed in a ceramic crucible, heated from 30 °C to 500 °C in nitrogen atmosphere with a constant heating rate of 20 °C/min. N₂ was used as purge gas with flow rate of 20 mL/min.

1.3.5 Universal Testing Machine

Tensile strength (TS) [MPa], Young modulus (ϵ) (MPa) and elongation at break (EL) [%] were evaluated according to the ASTM standard method (ASTM D882-02) and were conducted at Textile Testing Laboratory, Department of Mechanical Engineering Technology, UTHM. The samples (100 mm x 15 mm) were cut from each formulation of films and are mounted between the grips of the equipment for testing. Initial gauge length and speed are set to 75 mm and 0.05 m/min respectively.

1.3.6 Fourier Transform Infrared Spectroscopy (FTIR)

The interactions or bonds of the functional groups between pullulan, cellulose and CPSE were determined. The FTIR spectra of the films were recorded in an IR spectrometer (Perkin Almer) in the range of 4000-650 cm^{-1} . This test was conducted at Downstream Bioprocessing 1 Laboratory, Department of Chemical Engineering Technology, UTHM.

1.3.7 Scanning Electron Microscope (SEM)

Film surface morphology was examined by using SEM at Material Characterization Laboratory, Department of Materials and Design Engineering, Faculty of Mechanical and Manufacturing Engineering, UTHM. The dried film samples are mounted on a metal stub with double-sided adhesive tape. The morphological structures of the films are studied by a JSM-5600 LV SEM of JEOL, Tokyo, Japan and the images are taken at accelerating voltage 10kV and magnification of 20-23 times of origin specimen size.

1.4 Results and Discussions

1.4.1 Thermogravimetry Analysis

Figure 1.3 and Figure 1.4 display the TG curves of pullulan/CPSE (PL/P8) and pullulan/cellulose/CPSE at ratio 7:3 (PL/C30/P8). The results appeared in one stage of degradation process. The initial decomposition temperature or the onset weight loss of the film was about 58.68°C and 49.59°C for PL/P8 and PL/C30/P8 respectively. It is due to the dehydration. The prolonged weight loss of water above 100 °C is due to the presence of hydrogen bonding between functional groups in pullulan, cellulose and CPSE. The continuous degradation process with a broad curve was observed and slowed down after reaching 300°C, possibly due to the theoretical maximum degradation of pullulan, which is about 295°C. The end set degradation temperature for PL/P8 and PL/C30/P8 was about 299.31°C and 476.26°C respectively. The presence of CPSE extended the end set degradation temperature. It was found that the thermal stability of the films is greatly affected by the presence of water for as all the components are hydrophilic materials.

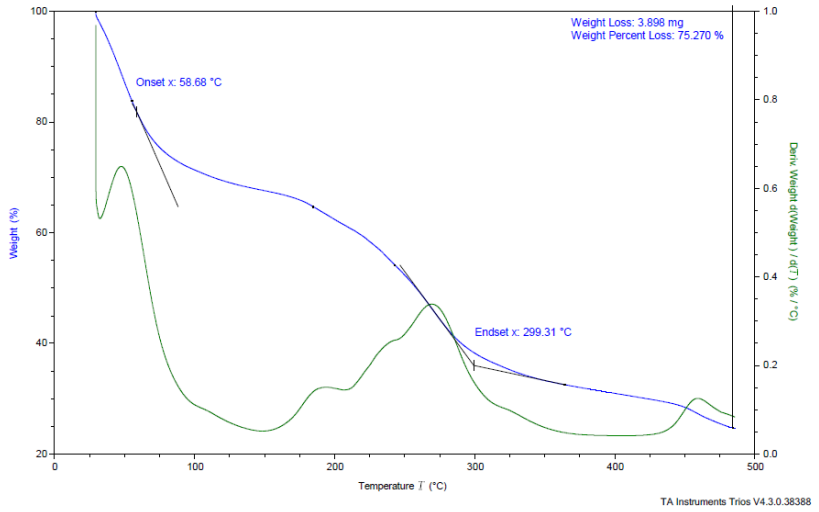


Figure 1.3: Isothermal spectra of PL/P8.

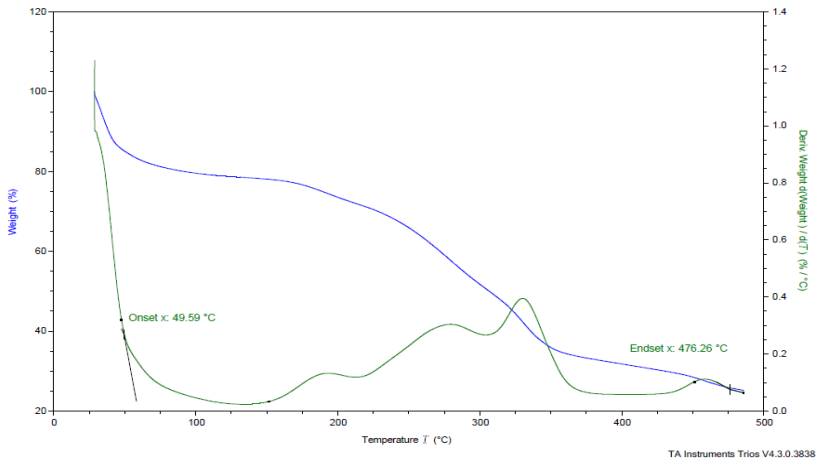


Figure 1.4: Isothermal spectra of PL/C30/P8.

1.4.2 Tensile Properties of Films

Table 1.3 shows the tensile strength (TS), Young Modulus (ϵ) and elongation at break (EL) for pullulan, pullulan/cellulose and pullulan/cellulose/CPSE films composition. Pullulan film (PL) shows the lowest tensile strength (5.12 Mpa) and elongation at break (12.3 %) compared to other compositions. Pullulan is a linear molecule, consists of a large number of side chains which resulted in easier molecules sliding and chain slippage. Thus the stress transfer ability among polymer chain is reduced. It can be observed that, tensile strength and elongation at break were slightly increased with increasing cellulose content from 10% to 30% for pullulan/cellulose films. The increment is about 4% and 1.2% for tensile strength and elongation at break, respectively. The improvement on tensile strength was due to the crystalline structure of the cellulose. Cellulose is known as a straight chain polymer, with no coiling or branching occurs. Thus, the molecule align and form a stiff rod-like conformation. In addition, the presence of multiple hydroxyl groups, hydrogen bonds with oxygen atoms holding the chains firmly together side-by-side and forming micro-fibrils which contribute to higher tensile strength. The results is in agreement with study reported by Turhan and Şahbaz (2004) who investigated on the tensile properties of different methylcellulose concentrations. They confirmed that the higher concentration of cellulose, results in higher tensile strength and elongation at break of the film.

Further enhancement observed for tensile strength and elongation at break of pullulan/cellulose films with presence of CPSE. Pullulan/cellulose/CPSE film at 30% cellulose (PL/C30/P8) shows the highest tensile strength and elongation at break, which is 5.97 Mpa and 15.6% respectively. Addition of CPSE indicated synergistic interactions between the polysaccharides in pullulan/cellulose films. It is possibly due to the increasing of film moisture content with addition of CPSE, which consequently increased the tendency to form a looser molecular network and molecular movement. Thus, when stress is applied, producing more flexible films as compared to pullulan/cellulose films. The increase in strain at break is probably caused by the breaking of hydrogen bonds, which allows more extension (Sun *et al*, 2010). It can be concluded that combining pullulan with cellulose and CPSE strengthen the film structure.

Table 1.3: Tensile strength, Young modulus and elongation at break values for each film composition

Sample	Tensile Strength (MPa)	Young Modulus (MPa)	Elongation at Break (%)
PL	5.12	5.42	12.3
PLC10	5.41	4.94	13.5
PLC20	5.53	4.87	13.7
PLC30	5.64	4.63	14.4
PLC10C8	5.72	4.44	15.0
PLC20C8	5.89	4.33	15.4
PLC30C8	5.97	4.27	15.6

However, addition of cellulose decreased the Young Modulus of pullulan films, up to 8%. Further reduction observed in Young Modulus with increasing cellulose content from 10% to 30%. The reduction is about 6%. A slight reduction of Young Modulus was observed for films with presence of CPSE. It is expected that moisture give an effect to Young Modulus of pullulan/cellulose/CPSE films as it is well known that cellulose and CPSE are categorized as hydrophilic materials. According to Sun *et al*, (2010), cellulose can be divided into amorphous, intermediate, and crystalline region. The intermediate region has an important role in determining the effect of moisture on the structures of cellulose. Water molecules can enter the intermediate regions causing swelling of the cellulose molecules and converting the crystalline regions into amorphous structures which break hydrogen bonds in the crystalline region. Thus, the ductility of the cellulose films was increased and modulus of pullulan/cellulose/CPSE films were reduced.

1.4.3 Morphological Analysis of SEM

Figure 1.5(a) to (d) show the surface morphology of the pullulan films and different ratios of pullulan/cellulose films. It can be observed in Figure 1.5(a) , there was small white spot dispersed in the surface of pullulan film. The similar result was obtained by Rinrada Pattanayaiying, (2014) who investigated on the optimisation and formulation of pullulan films with preservative additions.

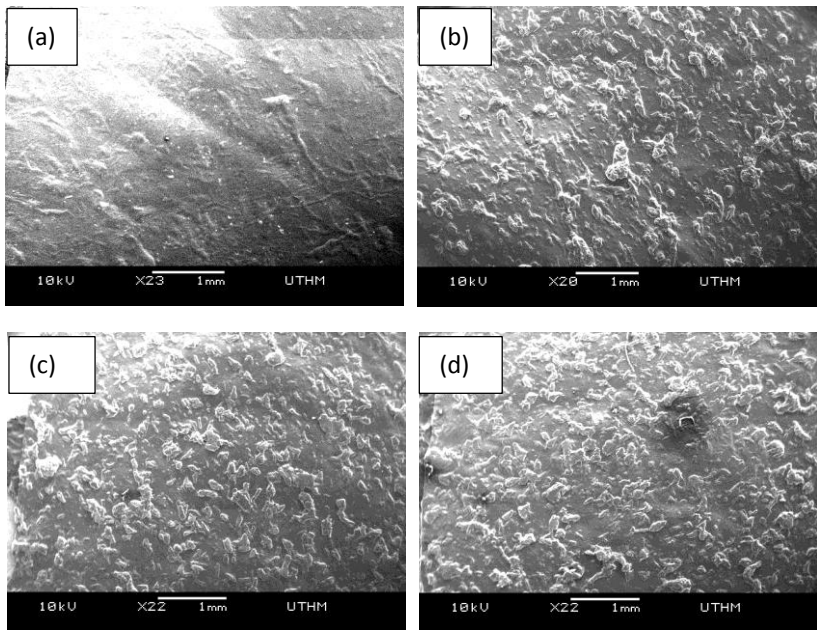


Figure 1.5: SEM morphology of a) PL, b) PL/C10, c) PL/C20, d) PL/C30

As shown in Figure 1.5 (b) to (d), addition of cellulose results in a rough surface of pullulan films. Numerous number of cellulose granules can be clearly observed on the surface of pullulan/cellulose films. Increasing of cellulose content from 10 % to 30 % contribute to a compact structure of the film surface.

Figure 1.6(a) to (d) represented the surface morphology of the pullulan films and different ratios of pullulan/cellulose/CPSE films. It can be observed that pullulan/cellulose/CPSE films (Figure 1.6c to 1.6d) appear a rough surface and almost similar with pullulan/cellulose films (Figure 1.6a). However, the cellulose granules are more compact as compared to pullulan/cellulose films. The addition of CPSE give no significance difference on the surface morphology of the films. The dispersion of reinforcing elements into polymeric matrices and their compatibility displayed vital aspects as their final properties and applicability give a significant effect on the homogeneity and mechanical performance of the materials (Eliane Trovatti *et al.* (2012).

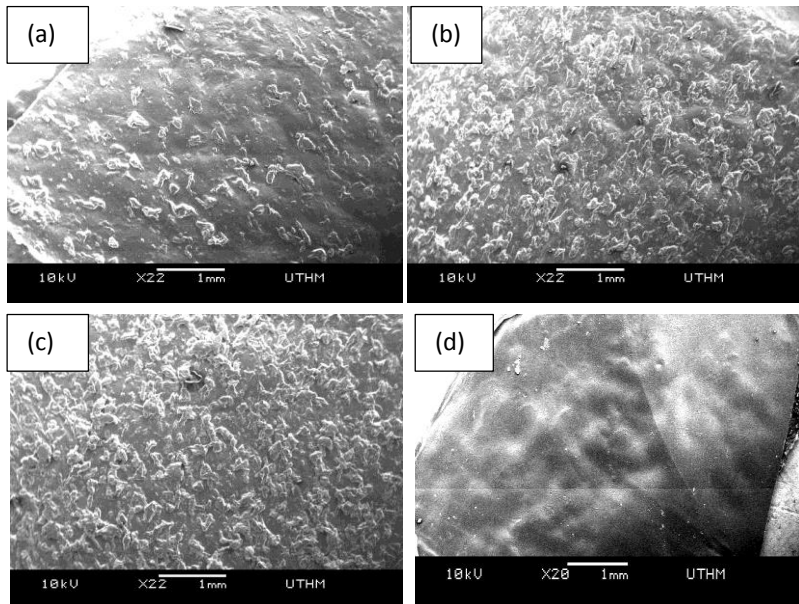


Figure 1.6: SEM morphology of a) PL/C10/P8, b) PL/C20/P8, c) PL/C30/P8, d) PL/P8.

1.4.5 FTIR Analysis

Figure 1.7(a) to (d) presented the possible chemical interaction between pullulan, cellulose and CPSE. A broad and strong absorption peak was observed at 3286 cm^{-1} for pullulan film (Figure 1.7a), indicating the stretching vibration of the hydroxyl groups (O-H).

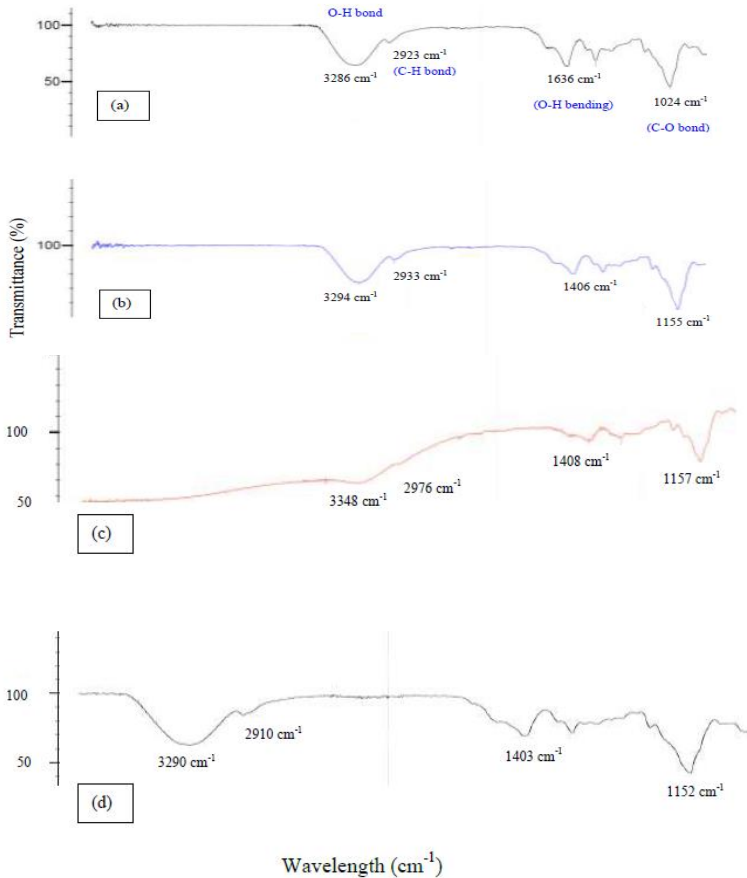


Figure 1.7: FTIR spectrum of a) PL, b) PL/C10 c) PL/C20 and d) PL/C30.

A shoulder peak at 2923 cm^{-1} represented the characteristics of C-H. The peak is almost similar to the result obtained by Jung, Jeong and Kim (2003), who found that the O-H and C-H stretching frequency of pure pullulan exhibits at peaks of 3356 cm^{-1} and 2943 cm^{-1} . The band at 1636 cm^{-1} attributes to the O-H bending (water absorption bond) as the similar bond was reported by Chen *et al.*, (2008) at 1630 cm^{-1} . A single peak assigned at 1024 cm^{-1} is possibly due to the presence of the (C-O) bond stretching frequency. Kirill I. Shingel (2002) confirmed that pullulan characteristics with high intensity peak were found at 1024 cm^{-1} . The peak at 918 cm^{-1} corresponded to C-O-H bending vibrations at C-6 position (amylose) which indicates the strength of interchain interaction via hydrogen bonding. Moreover, the main linkage of pullulan (α -(1, 4) and α -(1, 6)-D-glucosidic bonds) was observed at 918 cm^{-1} (Trovatti *et al.*, 2012).

The infrared spectrum for pullulan/cellulose samples (Figure 1.7b to 1.7d) at 9:1(PL/C10), 8:2(PL/C20) and 7:3(PL/C30), appears peak at 3294 cm^{-1} , 3348 cm^{-1} and 3290 cm^{-1} respectively. The peaks shifted to higher wavelength, which indicates the repeating units of -OH. Based on the previous study conducted by Diana Ciolacu, Florin and Valentin I. Popa (2005), they also found the broad band in the 3600 to 3100 cm^{-1} region, which is due to the OH-stretching vibration that gives considerable cellulose structure which can be correlated with the scission of the intramolecular and intermolecular hydrogen bonds. In addition, it is well known that cellulose is rich in hydroxyl groups that are prone to absorb moisture and it is likely that H_2O was responsible for this peak (Pandey, 1999). All the pullulan/cellulose samples portrays almost a similar spectrum. Another peak observed at 2933 cm^{-1} , 2976 cm^{-1} , 2910 cm^{-1} for sample PL/C10, PL/C20 and PL/C30 respectively. The peaks indicates the bending of alkane compound(C-H bond) which exist in the samples. The presence of amorphous cellulosic samples can be further confirmed by the shift of the band from 2900 cm^{-1} , corresponding to the C-H stretching vibration, to higher wavenumber values and by the strong decrease in the intensity of this band (D. Ciolacu *et al.* 2005). Based on the IR spectra for pullulan/cellulose, a vibrational peak was found which corresponding to symmetrical stretching of ether bond C-O-C that depicts the typical structure of cellulose which appears at 1155 cm^{-1} , 1157 cm^{-1} 1152 cm^{-1} for PL/C10, PL/C20 and PL/C30 respectively. Peaks at 1406 cm^{-1} , 1408 cm^{-1} and 1403 cm^{-1} for sample PL/C10, PL/C20 and PL/C30 respectively, indicated the symmetric stretching of CH_2 . The

forming of intermolecular hydrogen bonded hydroxyl groups between pullulan and cellulose may cause the breaking down of extensive hydrogen bonding network in the cellulose molecular chains itself causing their crystalline structure to be changed (Cao *et al.*,1999). As the fibre content in the blended film increases, the absorption peaks becomes more prominent. This may be due to the increased of cellulose content in the blended films which were from 10% to 30%.

The IR spectra for pullulan/cellulose/CPSE results almost a similar peaks as compared to pullulan and pullulan/cellulose samples. The broad absorption peaks among the three different ratios of samples were also relatively similar at 3294 cm^{-1} . The broad vibration peak was observed at 3330 cm^{-1} for pullulan/CPSE sample. The CPSE characterization via FTIR was reported by Prasetya *et al.* (2007). They proved that the presence of an aromatic C=C group is indicated by absorption at wavenumbers 1457.41 cm^{-1} and 1404.62 cm^{-1} . For pullulan/CPSE sample, the sharp peak of C-H stretch absorption appears at 1406 cm^{-1} . From the results, it can be concluded that there are a presence of chemical interaction between each component observed in the films.

1.5 CONCLUSIONS

From this study, it was revealed that the addition of CPSE improved the mechanical properties of the pullulan/cellulose/CPSE films. A significance increment of tensile strength and elongation at break was observed at ratio 7:3 with increment up to 85.7 % and 78.8 %, respectively. The presence of CPSE extended the end set degradation temperature. A rough surface was observed for pullulan/cellulose/CPSE films. However, the cellulose granules are more compact as compared to pullulan/cellulose films. The addition of CPSE give no significance difference on the surface morphology of the films. The composition of the film also exhibit an adequate strength and good thermal properties. Therefore, films with good thermal stabilities and high tensile strength provide potential indication to be commercialized as an alternative to replace the synthetic food packaging.

REFERENCES

- [1] ASTM Standard D638M-91a, Standard test method for tensile properties of plastics (metric). *Annual Book of ASTM Standards*, Vol. 10.01, 1992, pp. 172-180.
- [2] Akiyoshi, K., & Sunamoto, J. (1996). *Supramolecular assembly of hydrophobized polysaccharide*. *Supramolecular Science*, 3, 157–163.
- [3] Boredes P, Pollet E, Avérous L (2009). *Nano-biocomposites: biodegradable polyester/nanoclay systems*. *Prog Polym Sci* 34:125–155.
- [4] Cao, H.; Sun, H.; Liang, F.; Guo, H.; Liu, L.(1999). *Purification and determination of the structure of pullulan polysaccharide*. *Chem. J. Chin. Univ.*, 20, 1729–1732.
- [5] Cheng KC, Demirci A, Catchmark JM. (2011a). *Pullulan: biosynthesis, production, and applications*. *Appl Microbiol Biotechnol* 92:29–44.
- [6] Cheng KC, Demirci A, Catchmark JM. (2011b). *Evaluation of medium composition and fermentation parameters on pullulan production by Aureobasidium pullulans*. *Food Science Technology Intl* 17:99–109.
- [7] Dhall RK. (2013). *Advances in edible coatings for fresh fruits and vegetables: a review*. *Crit Rev Food Sci Nutr* 53:435–50.
- [8] Donabedian, D. H., Gross, R. A., & McCarthy, S. P. (1992). *Plasticization and reactive processing of pullulan*. *Polymeric Materials: Science and Engineering*, 67, 301–302.
- [9] Farris S, Unalan IU, Introzzi L, Fuentes-Alventosa JM, Cozzolino CA. (2014). *Pullulan-based films and coatings for food packaging: present applications, emerging opportunities and future challenges*. *J Appl Polym Sci* 131:40539.

- [10] Fei Z, Huang S, Yin J, Xu F, Zhang Y. (2015). *Preparation and characterization of bio-based degradable plastic films composed of cellulose acetate and starch acetate*. J Polym Environ 23:383–91.
- [11] Jung, S. W., Jeong, J. I., & Kim, S. H. (2003). *Characterization of hydrophobized pullulan with various hydrophobicities*. International Journal of Pharmaceutics, 254,109 121.
- [12] Kim JH, Kim MR, Lee JH, Lee JW, Kim SK (2000). *Production of high molecular weight pullulan by Aureobasidium pullulans using glucosamine*. Biotechnol Lett 22:987–990.
- [13] L. G. Hanu, G. P. Simon, J. Mansouri, R. P. Burford and Y.B. Cheng (2004). *Development of polymer–ceramic composites for improved fire resistance*. Journal of Materials Processing Technology, 153 401-407.
- [14] Mithilesh Yadav (2018). *Study on thermal and mechanical properties of cellulose/iron oxide bionanocomposites film*.Composites Communications,10).
- [15] Pandey, S., Goswami, G. K., & Nanda, K. K. (2012). *Green synthesis of biopolymer–silver nanoparticle nanocomposite: An optical sensor for ammonia detection*. International Journal of Biological Macromolecules, 51, 583–589.
- [16] Park, H. J., Weller, C. L., Vergano, P. L., & Testin, R. F. (1993). *Permeability and mechanical properties of cellulose-based edible films*. Journal of Food Science, 58.
- [17] Pattanayaiying, R., H-Kittikun, A., & Cutter, C. N. (2014a). *Effect of lauric arginate, nisin Z, and a combination against food-related bacteria*. International Journal of Food Microbiology.
- [18] Procedure ASTM D 882-91. *Standard test methods for tensile properties of thin plastic sheeting*. In Annual book of ASTM standards. Philadelphia: American Society for Testing and Materials.

- [19] Rhim J, Hong S, Park H, Ng P (2006). *Preparation and characterization of chitosan-based nanocomposite films with antimicrobial activity*. J Agric Food Chem 54:5814–5822.
- [20] Singh R, Gaur R, Bansal S, Biswas P, Pandey PK, Jamal F, Tiwari S, Gaur MK. (2015). *Aureobasidium pullulans—an industrially important pullulan producing black yeast*. Intl J Curr Microbiol App Sci 4(10):605–22.
- [21] Trinetta, V., Cutter, C. N., & Floros, J. D. (2011). *Effects of ingredient composition on optical and mechanical properties of pullulan film for food-packaging applications*. LWT Food Science and Technology, 44.
- [22] Zhou J, Zhang J, Ma Y, Tong J. (2008). *Surface photo-crosslinking of corn starch sheets*. Carbohydrate Polymer 74:405–10.

CHAPTER 2

POLYURETHANE MATERIAL FOR SYNTHETIC TIBIA BONE APPLICATION

*Siti Adawiyah Zulkefli¹, Maryam Hanim Mohamad Shaikhani¹, Ahmad
Kafrawi Nasution², Gan Hong Seng⁴, Muhammad Hanif Ramlee^{1,3}*

¹ Medical Devices and Technology Center (MEDITEC),
Institute of Human Centered Engineering (iHumen),
Universiti Teknologi Malaysia,
81310 UTM Johor Bahru, Johor, Malaysia.

² Department of Mechanical Engineering,
Faculty of Engineering,
Muhammadiyah University of Riau, Pekanbaru, Riau,
Indonesia.

³Bioinspired Innovation Group (BIOINSPIRA),
School of Biomedical Engineering and Health Sciences,
Faculty of Engineering,
Universiti Teknologi Malaysia,
81310 UTM Johor Bahru, Johor, Malaysia.

⁴Universiti Kuala Lumpur,
British Malaysian Institute,
Jalan Sungai Pusu,
53100 Gombak, Selangor, Malaysia.

2.1 INTRODUCTION

In human body, tibia is the second longest bone that essential for locomotion after femur bone. Based on the literature to the author's knowledge, tibia bone has high tendency to have injuries such as fractures (1,2). The fractures are varies depend on the cause of the injury which are from acute to chronic. In addition, the fractures could be an

oblique, transverse or stable fracture (2,3). As the consequence of the fractures, many treatment that had been introduced and recommended by the orthopedics practitioner in order to treat injuries involving tibia bone (4). For instance, bone grafting, external fixator and bone implant (3,5,6). Before prescribing a treatment to the patient, the treatment should have justification on injuries and the possibilities after having surgery. Undoubtedly, due to the requirement of justification by the surgeons it is proved that bone analogue is essential for orthopedics evaluation and assessment in biomechanics research.

In addition, a lot of research had been conducted from past until recent specifically in orthopedics biomechanics research (5). Subsequently, due to the increase in human population globally had been resulted in high demand of bone analogue in biomechanics orthopedics field (6). In order to conduct the experiment, cadaver are required and it had been challenging. As a consequence of the problem, a synthetic bone has been introduced by engineers (7,8). Recent, the existence of synthetic bone is to overcome the problem of using cadaver (8,9). In fact, synthetic bone had been main tool and widely used in vitro biomechanical evaluation. This experiment is to measure the accuracy of the estimated bone stresses along the dimension of synthetic tibia bone as the highlight within this area (10).

Admittedly, research regarding orthopaedics biomechanics research is extensively evolved and grew up until today (11). Realizing its significance, a study was conducted to replace the use of fresh cadaver bone as specimen for in vitro experimentation with a synthetic bone (8,12). The utilization of fresh human cadaver bone had been challenging due to its limitations. Consequently, the rate of success decreased when conducting in vitro evaluation for joint biomechanics and implant testing. The availability of storage for the fresh human cadaver bone is low and limited (8,13). Plus, to prevent defect to the cadaver, proper stores are required for the preservation purpose (9,14). As a result, the specimen needs to be stored in a proper storage. However, it costs nearly up to \$500 per specimen (13,15). From the previous report had mentioned that the cost for the whole cadaver ranges between \$1000 to \$1500 that is much higher (13). Nonetheless, this cost does not include the cost of the experiment and storage. Moreover, the tendency of being infected while using cadaver is high

(11). Thus, this condition are not favorable to the researcher as it will cause harm and may infected by the contagious disease.

Undoubtedly, the roles of tibia bone are importance to the human body. From the previous report stated that a lot of injuries related to tibia bone such as bone bruises, varus deformed tibia and tibial head depression fractures (16,17). Therefore, a validation must be properly justified in order to evaluate and analyse the joint biomechanics and implant testing before the medical devices can be used for real patients. A part from that, if the custom tibia bone is required, the in vitro assessment of tibia bone may be tougher. In other hand, there are a case where the bone are having osteogenesis imperfecta, where the long bones including tibiae is differing from the normal tibia bone as its shape is bowing and curvy(4). In consequence, a special tibia bone analogue is needed to evaluate its microstructural as well as its mechanical properties. Though, this requires a synthetic tibia bone with pathologies and it is very rare to find this kind of bone analogue.

2.1.1 TYPES OF SYNTHETIC BONE

Kinds of manufactured bone available in the market are changes relying upon its motivation of use. For example, a portion of the product are design for display and some of them are intended for testing reason. By and large, the model type is ordered as biomechanical and single fracture. Furthermore, the materials that been used to fabricate the synthetic bone also differ from others. It might have been made either for cortical or cancellous bone. Else, it is made of both cancellous and cortical bone. That is the reason, the materials utilized for the bone analogue is various relying upon its application. Every material that has been choose as the main component or minor component of the engineered bone must with a reason. Clearly, the materials must be able to characterize and mimic the structure and properties of the healthy human bone whether it be a cancellous or cortical bone. As shown in Figure 2.1, there are various type of synthetic bone that available in the market such as plastic cortical shell with cellular PU foam inside it. In addition, there are also synthetic bone made from PU foam cortical shell with cellular PU foam inside it. Another type of synthetic bone where the cortical are made with transparent plastic and the cancellous bone are made from cellular PU foam. There are also synthetic bone that develop by using only solid PU

foam. The best material delineates the succesful rate of in vitro experimentation as the material is an essential component that will appropriately be advocated in directing an investigation [15]. A terrible material will therefore prompt erroneous outcomes acquired

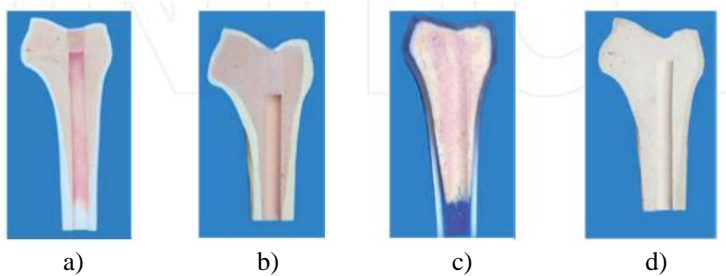


Figure 2.1: a) plastic cortical shell with cellular PU-foam inside b) rigid PU-foam cortical shell with cellular PU-foam inside c) transparent plastic cortical shell with cellular PU-foam inside and d) solid PU-foam throughout (18)

From previous report, it is discover that polymer foams as a testing substrate for the assessment of orthopaedic devices have prevalently used and popular over time (19). This may be due to the close resemblance of the polymer itself with cortical and cancellous bone. Subsequently, this clearly explains why polymer is favorable. Polymer have numerous categories to a numerous types of polymer such as polyethylene (PE), polystyrene (PS) and polypropylene (PP). However, among the types of polymers existed, PU had been acknowledging as a polymer that fits and compatible material for synthetic bone. The fabrication of commercial synthetic bone, Sawbones and Synbone has been prove as the material used is PU.

From the past decades, to develop synthetic bone there are many types of materials that be used. Moderately, some study utilized PU as the main material for the synthetic bone while others used PE. From the previous report stated that, the material can mimic the cancellous bone if only one material is used for the fabricated synthetic bone. In a contrary, the structure of cortical bone is not imitated by any materials. Alternatively, the composite bone analogue is use as a substrate in order to resemble both cancellous and cortical bone. Composite bone analogue also permit

an investigation of biomechanical through geometric as well as structural properties (2). In significant to that, one material resembles a cortical bone structure, conversely another material mimics the structure of cancellous bone. This is show by the common materials used as a composite is short glass fibre-reinforced epoxy with PU or else, the PU is substituted with PE. Precisely, to mimic the cancellous bone PU and PE is use while glass fibre-reinforced epoxy resembles the cortical structure of the bone.

In summary, the purpose of the study and application of the synthetic bone determine the type of materials that is used to fabricate the bone analogue. In addition, studies have proved that out of all polymer, PU is the best material that enables to mimic the properties of human wet bone (9). Furthermore, Figure 2.2 show the composite tibia from Sawbones. The fourth generation of large tibia composite model are manufactured by using pressure-injected technique made up from short glass fibre reinforced epoxy (as cortical bone) with PU (as cancellous bone).



Figure 2.2 Depicts fourth generation of large tibia composite model from Sawbones(2)

2.1.2 CURRENT APPLICATION OF SYNTHETIC BONE

The utilization of the bone analogue have given significant to the field of orthopaedic biomechanics. It is very useful for surgeons as an orthopaedic devices in their training. Futhermore, it would help the medical students and orthopaedic surgeon to familiarize with the tools as it can reduced the failure while doing the surgery (20). Not only to emphasize the important of synthetic bone for surgeons, it is also beneficial for the houseman-ship officer as well as the students of medicine in their medical studies (21,22). This is also can be used to help the junior doctors to have simulation in operating theatre before come to real surgery (20). In medical field, the utilization of bone analogue allows them to be exposed of the structure of the human real bones in the

process of learning of pathologies, fractures and bone grafting. Importantly, to use of cadaver for the medical students and orthopaedic practitioner to study orthopaedic is high in cost. Furthermore, the limitation of the human bone has limit the study in medical setting due to its variability, preservation, low availability and possibility of infection. This have made cadaver as the second choice in orthopaedic studies prior to synthetic bone (22). Nonetheless, the cadaver has cause problem as a tool for the experimental research. In contrast, researcher are use synthetic bone as an alternative for cadaver. Figure 2.3 depicts the application of synthetic bone in orthopaedic surgical simulation in order to investigate the effectiveness of low-cost orthopaedic drilling technique.

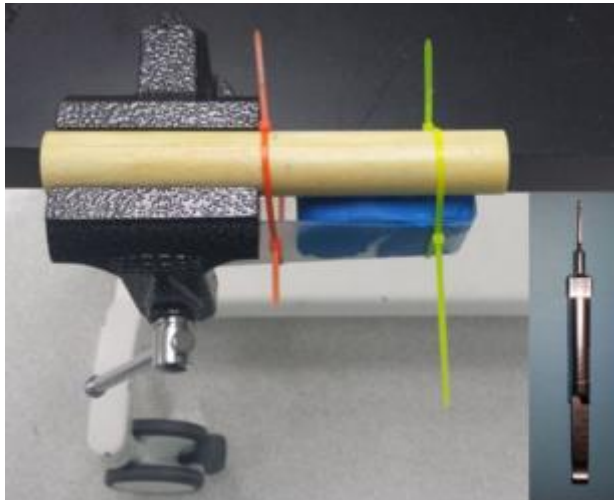


Figure 2.3 Portrays a synthetic bone model clamped by a clay mode to investigate the effectiveness of low-cost orthopaedic drilling technique during orthopaedic surgical simulation.(23).

Equally important in research into orthopedic biomechanics is the use of synthetic bone. Before applying to real patients, an experiment must be conducted in the assessment of pathologies, including bone fractures (4,13). This is to provide a proper justification for the patient's abnormalities. Instead of fresh human corpse bone as previously described, synthetic bone is preferable in *in vitro* experimentation. (23). The orthopedic *in vitro* assessment allows the researcher to estimate any effects of adverse events that may occur before the patient receives the treatment. (21). For example, the surgeon must know the appropriate fixator to be used by the patient, whether an external or internal fixator, when evaluating oblique tibia bone (21). A study was conducted by the researcher to analyze its safety, comfort and efficacy in order to propose the best configuration of the fixator. Again, these require bone analog and in a way to explain why the field of research on orthopedic biomechanics continues to develop.

2.1.3 BIOMECHANICAL STUDY USING SYNTHETIC BONE

Synthetic bone is recognized as orthopedics surgical techniques since 1950 and recent (6,22). Establishing synthetic bone as an orthopedic tool has overcome the challenges of using cadaver specimen. Firstly, the cadaver is not used due to bone analog is more consistent (8,22). This consistency allows bone substrates to be mass-produced. The cost is therefore minimal rather than the bone of the cadaver itself. Certainly, the cost of synthetic bone composite of the fourth generation is only \$ 170, implying indirectly a huge gap with the cost of the cadaver specimen (15,24). From the cost, it clearly describes the relatively cheap and widely available synthetic bone. Although the use of synthetic bone that lacks the 'true feeling' of the real human bone, it is useful in providing understanding and familiarity with the orthopedic equipment and instrument (22). It also allows orthopedic training for surgeons and trainees, such as fracture fixation (21). Its bone analog advantages orthopedic trainees in the development of experience, however they are incomparable with the senior surgeons (22). In a much more in-depth explanation is to say they lack fidelity and quality in order to be of value to senior surgeons. For the meantime, Figure 2.4 shows the use of synthetic bone for four-point bending tests which are useful in biomechanical environments.



Figure 2.4 Specifies four-point bending test setup of the fourth generation of Sawbones ' large tibia composite model (2)

2.2 FABRICATION OF CUSTOMIZED SYNTHETIC BONE

2.2.1 Bone Segmentation

The CT scan data, particularly, covered the whole human anatomy. Hence, To specify the ROI in tibia only, segmentation was performed. This step was accomplished using Mimics 10.01 software. A predefined threshold (ranging from 226 to 3071) was set to bone as the hub in this study was subsequently loaded into this software by a project (CT lower limb). In addition, only the bone area of the CT Scan data should be highlighted and focused. Moreover, a region growing tool was applied to focus on shinbone that was the required region. Particularly, in order for more convincing of manipulation and operation while segmenting tibia bone from the other bone in the software, different color is recommended for the tresholds. Next step was edit mask as the procedure is required to segment slice by slice by eliminating bones which are near the tibia bone such as calcaneus, femur, fibula and patella. As well as a sub software in Mimic which was Magix was used to applied the remesh technique for segmenting the tibia.

In addition, the three-dimensional mask was calculated and displayed a sole tibia. Clearly, in order to get better appearance, the smoothing process must be conducted. From that point forward, the ROI was estimated to get the rough length of Malaysian male tibia by choosing measure 3D distance devices on the recorded toolbar in Mimics and essentially drag start to finish on the veil. At instant, the value of tibia's length was popped out. Notably, before fabrication was continued both procedures required Mimics. Generally, Mimics was used to segment the bone (Figure 2.5).

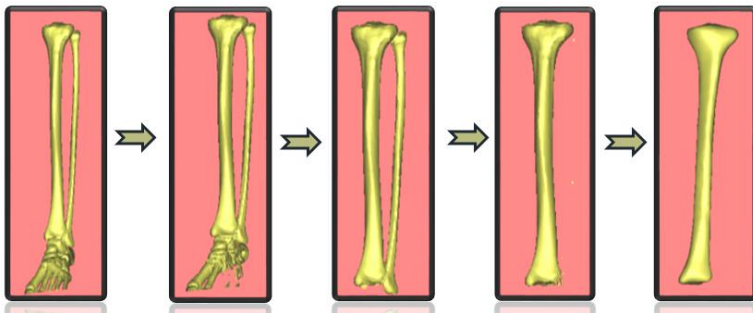


Figure 2.5: Illustrate Mimic software was utilize to do the process of segmentation.

2.2.3 Fabrication of Mold

In order to cast the first layer of the mould, ply woods, plasticine (approximately 15 boxes) As for the casting of first layer of mould, the equipment acquired were ply woods, plastiline (approximately 15 boxes), glove, master bone, vesaline, Moldmaker RTV silicone rubber and its hardener were required. Significantly, the reference for this project and preparation of mould was using synthetic bone from the Sawbone. The master bone as shown in Figure 2.6 used was a display product instead of the Sawbones test product. The dimensions were approximately similar (374.86 mm and 355 mm respectively in terms of length) after a comparative measurement between the CT scan data and the master bone. Therefore, during the whole process of molding technique, there was no significant changes were required. The tibia bone analog was

placed on a piece of flat wood in the process of developing the first layer of mould. Then, the the bone was by plastiline. Plasticine was used to assemble the ply woods and to build a container for moulding. Plus, the use of plastiline facilitated by adhering it around the tibia bone to create the bone pattern in a mould. Figure 2.6 revealed the initial process of adhering plastiline to assemble the plywood in a container.

It also grasped the bone in place to ensure even or regular plus a consistent bone moulding configuration (Figure 2.7). Whilst the silicon rubber was poures into the mold, it prevent the master bone from moving. Understandably, a custom-made ply wood was used as a container rather than a ready-made container as the container had to be dismantled as the dried mould and removed from the container. Additionally, to enclose the tibia bone, a rectangular box was constructed. Nonetheless, in order to prevent any leakage that could be happened while pouring the silicone rubber a precaution step was taken. A thick plasticine were applied to overlay the joints.

As precaution, assured that a thick plastiline were applied at the joints' area of ply woods box to avoid any leakages that might happened after the pouring of silicone rubber. The volume of the box would be measured approximately to confirm the size of the rectangular box. This was to ensure that the drying agent and silicon rubber mixture were properly filled into the rectangular box made of plywood. After that, the wholesurface of plasticine surrounded the master bone was applied vesaline (Figure 2.8). This was meant to ensure that the rubber of silicone would not adhere to these areas and for easier disassembling of ply wood container.



Figure 2.6: Depicted The plastiline adhering process to assemble the plywoods into a container .



Figure 2.7: Disclosed The master bone (Sawbones) used to create a mould.



Figure 2.8: Depicted the placement of tibia and fibula adhered by plastiline.

2.2.4 Preparation of Polyurethane

PU and its hardener were used as resin. PU usually consisted of two parts, Part A and Part B. Basically, PU usually consisted of two parts, Part A and Part B. Part A defined the PU solution itself (see Figure 2.9) while Part B defined the hardening agent. Based on manufacturer recommendations stated that the ration between PU and its hardener is 2:1. PU was chosen because of its popularity and widely use as resin for bone substrate (19,25). The recyclable materials were used as a safety measure during resin preparation to prevent damage to the laboratory equipment. The properties of PU used in this research execute high strength. Hence the damage that occur because the PU cannot be wash by universal solvent soon after it dried. In order to determine the volume of chemical solution (PU) for tibia acquired through this moulding method, water was filled in through the holes of the second moulding layer. Beforehand, rubber band is use to tighten both layer of the mould. This was to ensure no leakage happened once the mold were filled with resin.

After the mould was filled with water, the water was poured out into a beaker. This method used to measure the exact volume of resin that required to fill the tibia mould. Then, the water was transferred to a bottle. The bottle use was cut into half to make it as container. As the water was in the bottle, the level of the water was mark to indicate the

volume of required resin. As PU have two part which were Part A and Part B, two bottle were used. Two bottles were deployed for Part A and Part B. It was subsequently reported that the resin volume acquired was approximately 600 ml, referring to the volume of water poured out of the mould. According to the guidelines of the manufacturer, the ratio of Part A and Part B of the PU system was 2:1. Thus, the volume for part A and Part B were 400ml and 200ml respectively resulting in a total volume of 600ml.

Soon after both parts combined together, to make sure that the mixture was mixed well and blended it was continuously stirred about six to nine minutes. Plus, to prevent the presence of bubbles. The resin's inconsistency may affect the composition, structure and duration of the bone. In this regard, after being mixed together, Figure 2.10 reveals the composition between Part A and Part B. The mould was later filled with resin through the holes as soon as possible as its gel time took only 20 minutes. Generally, two to three days were usually sufficient to let the sample dry. Again, the first and second layer moulding process would be repeated for another four times as this project required a total of five tibia bone analogues. Notably, the hardest part of this experiment was to make five bone samples within seven days of the expiry date of the PU system being seven days after opening its container.



Figure 2.9: Portrayed PU (Part A) solution before mixing with the hardener (Part B)



Figure 2.10 Disclosed PU (Part A) solution after mixing with the hardener (Part B)

2.2.5 Synthetic Bone

Figure 2.11 shows the structure of physical synthetic bone after fabrication. The synthetic bone is normally will be used for the orthopaedic training and also for the biomechanical study of implant (Figure 2.11).

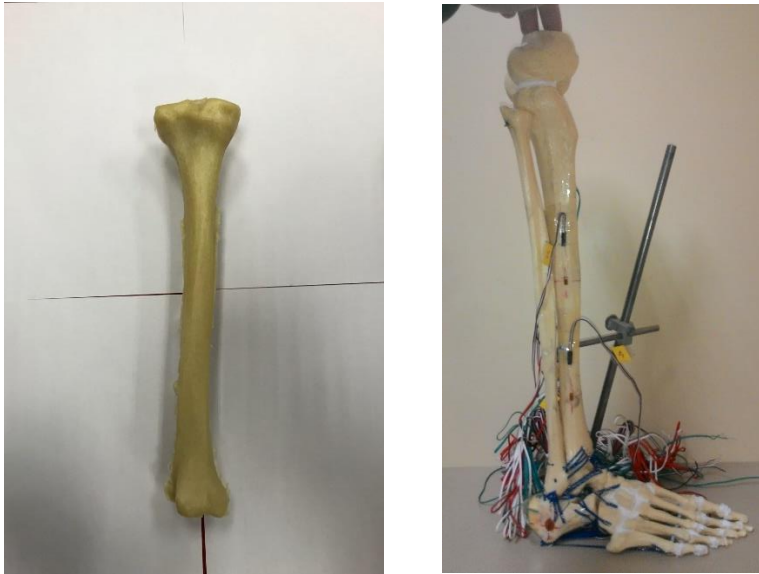


Figure 2.11 Tibia synthetic bone (left) and example of the application of synthetic bone for the external fixator analysis (right).

ACKNOWLEDGEMENT

The authors would like to thank to the Medical Devices and Technology Centre, School of Biomedical Engineering and Health Sciences, Faculty of Engineering and Universiti Teknologi Malaysia for the research facilities and laboratories. This work was financially supported by the Universiti Teknologi Malaysia under the Research University Grant (20H20, 4J358, 15J84 and 20H26), Ministry of Energy, Science, Technology, Environment and Climate Change (EF0618I1166 and 4S144) Fundamental Research Grant Scheme (FRGS) Ministry of Education Malaysia (278784-294883).

REFERENCES

1. Kaman MO, Celik N, Karakuzu S. Numerical Stress Analysis of the Plates Used to Treat the Tibia Bone Fracture. 2014;(May):304–9.
2. Gardner MP, Chong ACM, Pollock AG, Wooley PH. Mechanical evaluation of large-size fourth-generation composite femur and tibia models. *Ann Biomed Eng.* 2010;38(3):613–20.
3. Puha B, Gheorghievici TS, Carata E, Friedl W, Rares S, Sirbu P-D. OS5-35 Biomechanical analysis of three fixation methods in treatment of pilon fractures AO 43-C3. *Injury.* 2016;47:S13–4.
4. Caouette C, Ikin N, Villemure I, Arnoux PJ, Rauch F, Aubin CÉ. Geometry reconstruction method for patient-specific finite element models for the assessment of tibia fracture risk in osteogenesis imperfecta. *Med Biol Eng Comput.* 2017;55(4):549–60.
5. Lim CT, Ng DQK, Tan KJ, Ramruttun AK, Wang W, Chong DYR. A biomechanical study of proximal tibia bone grafting through the lateral approach. *Injury.* 2016;47(11):2407–14.
6. Campana V, Milano G, Pagano E, Barba M, Cicione C, Salonna G, et al. Bone substitutes in orthopaedic surgery : from basic science to clinical practice. 2014;2445–61.
7. Completo A, Fonseca F, Simões JA. Strain shielding in proximal tibia of stemmed knee prosthesis: Experimental study. *J Biomech.* 2008;41(3):560–6.
8. Cristofolini L, Viceconti M. Mechanical validation of whole bone composite tibia models. *J Biomech.* 2000;33(3):279–88.
9. Wong RCW, Tideman H, Merckx MAW, Jansen J, Goh SM, Liao K. Review of biomechanical models used in studying the biomechanics of reconstructed mandibles. *Int J Oral Maxillofac Surg.* 2011;40(4):393–400.
10. Taddei F, Cristofolini L, Martelli S, Gill HS, Viceconti M. Subject-specific finite element models of long bones : An in vitro evaluation of the overall accuracy. 2006;39:2457–67.
11. Articles R. Sawbones laboratory in orthopedic surgical training. 2016;37(C):348–53.
12. Bredbenner TL, Haug RH. Substitutes for human cadaveric bone in maxillofacial rigid fixation research. *Oral Surg Oral Med Oral Pathol Oral Radiol Endod.* 2000;90(5):574–80.

13. Jaber FT, Al-Jayyousi AB. A phantom for cadaverless evaluation of targeting systems for distal locking of intramedullary nails. Middle East Conf Biomed Eng MECBME. 2014;115–8.
14. Macleod AR, Gill HS. VARIATIONS IN CORTICAL THICKNESS OF COMPOSITE FEMUR TEST SPECIMENS. 2016;3282.
15. Martin R, Menorca G, Reed JD. NIH Public Access. 2014;22(2):111–20.
16. El-Zayat BF, Heyse TJ, Fanciullacci N, Labey L, Fuchs-Winkelmann S, Innocenti B. Fixation techniques and stem dimensions in hinged total knee arthroplasty: a finite element study. Arch Orthop Trauma Surg. 2016;136(12):1741–52.
17. Kim SM, Kim KW, Cha SM, Han KY. Proximal tibial resection in varus-deformed tibiae during total knee arthroplasty: an in vitro study using sawbone model. Int Orthop. 2015;39(3):429–34.
18. By P. World ' s largest Science , Technology & Medicine Open Access book publisher :
19. David F, Senck S, Hollensteiner M, Esterer B, Augat P, Eckstein F, et al. AC NU. 2017;
20. Goyal S, Radi MA, Ramadan IK, Said HG. Arthroscopic skills assessment and use of box model for training in arthroscopic surgery using Sawbones – “ FAST ” workstation. 2016;
21. Szyld D, Strauss EJ. Ac ce p te d us t. Injury. 2014;
22. Stirling ERB, Lewis TL, Ferran NA. Surgical skills simulation in trauma and orthopaedic training. 2014;1–9.
23. Ruder JA, Turvey B, Hsu JR, Scannell BP. Effectiveness of a Low-Cost Drilling Module in Orthopaedic Surgical Simulation. J Surg Educ. 2017;74(3):471–6.
24. Yehyawli TM, Thomas TP, Ohrt GT, Marsh JL, Karam MD, Brown TD, et al. Topics in Training. 2013;92:1–8.
25. Payne T, Mitchell S, Halkon B, Bibb R, Waters M. Development of a synthetic human thigh impact surrogate for sports personal protective equipment testing. Proc Inst Mech Eng Part P J Sport Eng Technol. 2016;230(1):5–16.

CHAPTER 3

THE EFFECT OF POLYETHYLENE GLYCOL ON PRECIPITATION OF ZINC OXIDE NANOPARTICLES FOR PHOTOCATALYTIC DEGRADATION OF DYE

Nur Hanis Hayati Hairom^{1}, Abdul Wahab Mohammad², Mohamad
Alif Hakimi Hamdan¹*

¹Department of Chemical Engineering Technology, Faculty of Engineering Technology, Universiti Tun Hussein Onn Malaysia, Hab Pendidikan Tinggi Pagoh, KM 1, Jalan Panchor, 84600 Muar, Johor, Malaysia.

²Centre for Sustainable Process Technology (CESPRO), Faculty of Engineering and Built Environment, Universiti Kebangsaan Malaysia, 43600 UKM Bangi, Selangor, Malaysia.

3.0 INTRODUCTION

Dyes are a substance that widely used in the textile and printing industries. These industrials consume a substantial amount of water in their manufacturing processes mainly in the dyeing and final operations of the plants (Babu, Parande, Raghu, & Kumar, 2007). Effluent from the operations was classified as one of the most polluting due to its highly colored, toxic, carcinogenic, mutagenic, non-biodegradable and consist of complex components (Carmen & Daniela, 2010). These unwanted features will bring some hazards that pose a risk to the environment and also affect to human health (Konstantinou & Albanis, 2004). In 2010, Wang and co-workers reported that about 1–20% of the total world production of dyes was lost during the dyeing process and consequently released in the effluents stream. Furthermore, the colored wastewater that has been discharged in the environment is a considerable source of eutrophication and can disrupt the aquatic community. Therefore, the purification of dye wastewater is very important for proper pollution control.

Traditional physical techniques such as ultrafiltration (Dong et al., 2011), reverse osmosis (Mustafa & Nakib, 2013) and adsorption (Rashed, 2013) have been applied for the removal of dye pollutants. However, there are several limitations of these methods to meet the discharge criterion of environmental quality. The traditional methods were only succeed in transferring organic compounds from water to another phase and lead to create secondary pollution that require a further treatment which will add more cost to the process (Akpan & Hameed, 2009). Therefore, developments of more advanced technologies are particularly required for better effluent discharge, principally to attain environmental cleanliness and human health safety.

One of the promising methods for dye wastewater treatment is photocatalysis process due to no formation of polycyclic product, quick oxidation and oxidation of pollution up to the parts per billion (ppb) level (T. Chen, Zheng, Lin, & Chen, 2008). In this method, photocatalyst absorbs a photon of light that more energetic than its bandgap. Subsequently, a hole electron pair will be formed from the excitation of electrons and leading to initiate the oxidation and reduction processes to generate the strong oxidizing hydroxyl radical ($\text{OH}\cdot$). The hydroxyl radical played a significant role for degradation of dyes and reduction of organic compounds to carbon dioxide (CO_2), clean water (H_2O) and inorganic constituents (Hairom, Mohammad, Ng, & Kadhum, 2014b). Metal oxides nanostructures including zinc oxide (ZnO), titanium dioxide (TiO_2) and copper oxide (CuO) with various morphologies have been receiving much attention in the photocatalytic activities studies (Talebian & Jafarinezhad, 2013). To date, some of literatures claimed that ZnO nanoparticles show the best efficiency as a photocatalyst in photocatalytic degradation of dyes (Hairom, Mohammad, & Kadhum, 2015; Jain, Bhargava, & Panwar, 2014; R. Khan et al., 2014; Tripathy et al., 2014).

ZnO is a semiconductive material that has unique physical and chemical properties, such as high chemical stability, broad range of radiation absorption and high photostability. It regularly used as a converter, energy generator, photocatalyst and adsorbent due to its piezo- and pyroelectric properties, low toxicity, biocompatibility and biodegradability (Kołodziejczak-Radzimska & Jesionowski, 2014). Moreover, ZnO has a broad energy band (3.37 eV) with high bond energy (60 meV) which is much larger than the thermal energy at room

temperature (26 meV). This strong excitation binding energy can easily realize the UV photo emission at room temperature, which leads to great potential application in photocatalysis process.

To date, various methods have been implemented for the production of ZnO nanoparticles such as precipitation (Kanade, Kale, Aiyer, & Das, 2006), sonochemical (Banerjee, Chakrabarti, Maitra, & Dutta, 2012), electrolysis (Nomura, Shibata, & Maeda, 2002) and hydrothermal synthesis (Sekiguchi, Miyashita, Obara, Shishido, & Sakagami, 2000). Among these methods, precipitation has been recognized as the preferable technique since it provides a simpler route, economical and occurs at moderately low temperatures (Hairom et al., 2015). Precipitation process is the production of a solid in solution through a chemical reaction between the reactants. The advantages of this simple process are inexpensive, energy saving (room temperature) and produce good yields with uniform shapes and sizes (Hairom et al., 2015).

However, one of the serious problems faced in the synthesis of nanoparticles is agglomeration. Agglomeration is the interaction between particles due to Ostwald ripening and Van Der Waals when the growth of particle is not controlled (Sharma & Kumara, 2008). It can be prevented by stabilising them electrostatically in suitable phases to achieve the selected size (Saravanan, Diwakar, & Mohankumar, 2011). In 2015, Dumbrava and his co-workers claimed that capping agent such as polyvinyl pyrrolidone (PVP) and polyethylene glycol (PEG) has a great tendency as a stabilizing agent to prevent the aggregation of particles.

Previously, Hairom, Mohammad, Ng, & Kadhum (2014a) confirmed that the ZnO synthesized via precipitation under stirring condition in the presence of PVP (ZnO-PVP-St) shows the great performance in membrane photocatalytic reactor (MPR) in terms of highest photodegradation efficiency and minimum membrane flux decline. However, recent study was revealed that PEG has attracted special attention as a green and inexpensive solvent in various chemical transformations (Vafaezadeh & Hashemi, 2015). Since the performance of nanoparticles may be influenced by the preparation method, this study intense to investigate the influence of PEG in synthesizing of ZnO nanoparticles via precipitation method for photocatalytic degradation of

dye wastewater. This simple and green approach is considered as a great potential application in industry.

3.1 RESULTS AND DISCUSSION

3.1.1 Introduction

This chapter discusses the results that have been collected from the experimental works according to procedure in chapter 3. The raw results collected were tabulated in the Appendix B. The data collected were analyzed and represented in form of table and graph. Then, it discusses the results and research findings by comparing them with the previous works mentioned in the literature review chapter.

3.1.2 Synthesis and characterization of ZnO-PEG-St nanoparticles

Till date, nanostructures have attracted attention of researchers for their many important technological applications. The synthesis of nanostructures is a growing area of research. The synthesis of nanostructures by a low-cost process and green method would be of great technological importance. The ZnO-PEG-St nanostructures were successfully synthesized by green precipitation method. Oxalic acid and zinc acetate were mixed together. After 5 minutes of the reaction, different amount of PEG was added into the solution and the solution was continuously stirred at 300 rpm for 24 hours. After that, the white precipitate formed was filtered by using vacuum suction and dried for 1 hour at 100°C by oven. This procedure was done to remove excess water in the solution. Then, the white powder was calcined at 500°C for 3 hours to remove impurity. In 2009, Akpan & Hameed reported that the calcination temperature effect on the photocatalytic activity of ZnO-TiO₂. They have investigated on the photocatalytic degradation of Rhodamine B. Their results also revealed that the photocatalytic activity of Zn-TiO₂ rapidly increased and was optimum at 500°C as the calcination temperature increased from 300°C to 500°C. Further increase in the calcination temperature from 500°C to 900°C resulted in lower photocatalytic activity of the prepared catalyst.

ZnO-PEG-St was characterized by using FTIR. Based on the Figure 3.1, the graph illustrates for FTIR spectrum of synthesized ZnO-PEG-St (0.010 g/L of PEG). The O-H bonding was shown at the peak 546.68 cm^{-1} and 3729.60 cm^{-1} . The band arises due to the O-H bending of the hydroxyl group of water that reveals the existence of a small amount of water absorbed by the ZnO-PEG-St nanostructures (Patra, 2007). The peak at 2337 cm^{-1} and 2360.41 cm^{-1} show the CO_2 bond. In 2005, Hlaing Oo and his co-worker reported that ZnO nanoparticles contain CO_2 impurities. He also claimed that the use of the precursor material such as zinc acetate can cause some of the impurities remaining in the ZnO because of the precursor material and reaction product. Furthermore, the peak at the 473.33 cm^{-1} show the characteristic absorption of Zn-O bonding and also authenticates presence of ZnO. The similar results were also reported by others researcher (Singh, Kumar, & Malhotra, 2012).

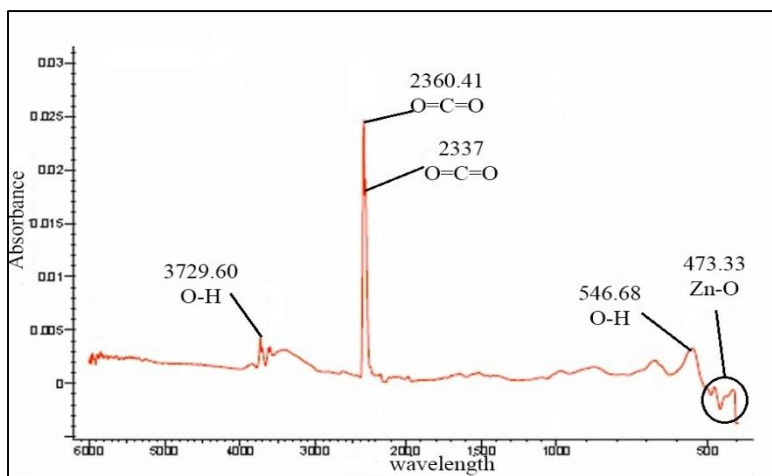


Figure 3.1: FTIR spectrum of synthesized ZnO-PEG-St (0.010 g/L of PEG).

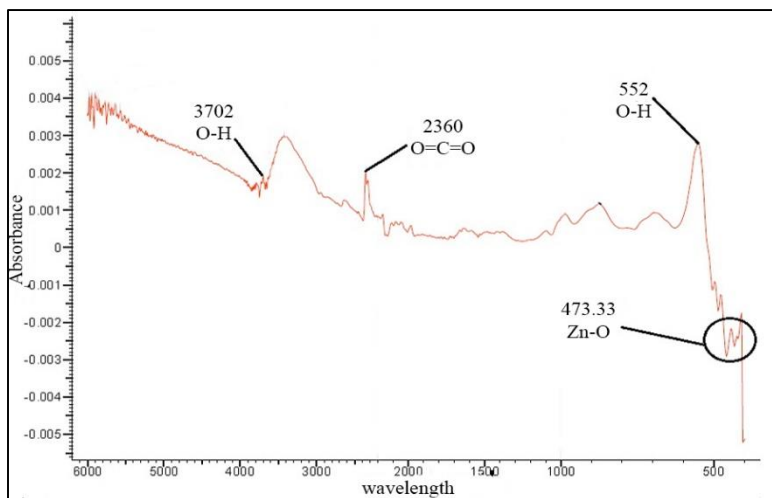


Figure 3.2: FTIR spectrum of synthesized ZnO-PEG-St (0.015 g/L of PEG).

Based on the Figure 3.2, the graph shows the FTIR spectrum of synthesized ZnO-PEG-St (0.015 g/L of PEG). The trend of the graph quite same compare in Figure 3.1. The O-H bonding was shown at the peak 552 cm^{-1} and 3702 cm^{-1} indicate the hydroxyl group in the water. The peak at 2360 cm^{-1} show the CO_2 bond that show the ZnO has CO_2 impurities. The peak at 473.33 cm^{-1} was assigned to the stretching band of Zn-O.

3.1.3 Photocatalytic activity for degradation of dye wastewater

Till to date, there are many types of semiconducting systems have been studied for photocatalysis including TiO_2 , ZnO, ZrO_2 , CdS, WO_3 , and other (Mondal & Sharma, 2014). Most of them have band gap in the UV (ultraviolet) region which equal to or greater than 3.36 eV (Thiruvengkatahari, Vigneswaran, & Moon, 2008). Thus, these catalysts promote photocatalytic reactions under the illumination of UV radiation (Sung-Suh, Choi, Hah, Koo, & Bae, 2004). Surface area, surface defects and band gap of the metal oxide nanostructured catalysts play an important role in the photocatalysis (Thiruvengkatahari et al., 2008). Zinc oxide is an excellent wide band gap, natural n-type semiconducting

material with binding energy (60 MeV), abundant in nature, nontoxic nature and environmental friendly photocatalyst (Jin, Wang, Sun, Blakesley, & Greenham, 2008).

It can absorb wider range of spectrum of radiation which also makes it more applicable for dye sensitized solar cells and solar photovoltaic applications (Thiruvengkatachari et al., 2008). The photocatalytic efficiency of ZnO nanomaterials is believed to be much better than normal photocatalysts (F. Lu, Cai, & Zhang, 2008). It is extensively used to treat wastewater, such as printing and dyeing wastes, dairy and food wastewater, drugs and pesticides wastewater, textile wastewater, papermaking wastewater, and other related (Thiruvengkatachari et al., 2008).

The mechanism of the photocatalytic degradation start with a hole electron pair will be formed from the excitation of electrons and leading to initiate the oxidation and reduction processes to generate the strong oxidizing hydroxyl radical (OH•). The hydroxyl radical played a significant role for degradation of dyes and reduction of organic compounds to carbon dioxide (CO₂), clean water (H₂O) and inorganic constituents (Hairom et al., 2014b).

Furthermore, ZnO nanoparticles in presence of PEG was successfully synthesized in this experiment. Then, the photocatalyst was used to treat wastewater in different light intensity (UV and fluorescent). The successful of synthesis ZnO nanoparticles can be measured when more than 46% of dye had been removed from the wastewater. Recently, Hairom et al., (2015a) had conducted experiment of membrane photocatalytic reactor (MPR) by and their result shows that they can remove 46% of dye from the wastewater. The result show that ZnO nanoparticles contain PEG has great potential to act as photocatalyst for wastewater treatment. In the photocatalytic activity for degradation of dyes in wastewaters, the parameters that need to be studied are the effect of light intensity under UV and fluorescent, the effect of different photocatalyst and the effect of pH of the solution to be degraded These parameters will be considered as they influenced the photocatalytic processes of the degradation of dyes in wastewaters.

3.1.4 Effect of light intensity

Light intensity is the important factor in the dye wastewater treatment. This is because every chemical compound absorbs, transmits or reflects light (Sanda, Victor, Monica, & Alina, 2012). In order to study the effect of light intensity on photocatalytic activity of ZnO-PEG-St (0.010 and 0.015 g/L of PEG), photocatalysis process have been carried out under the fluorescence and UV light. This is due to the different light intensity of the fluorescence (6W) and UV (15W). Figure 3.3 shows the changing pattern of dye degradation during photocatalysis process in the presence of ZnO-PEG-St (0.010 g/L of PEG) in 1-hour duration. The wastewater contain ZnO-PEG-St are exposed under different condition of light source, specifically ultraviolet (UV) lamp and fluorescent lamp. According to the result in Figure 3.3, photocatalysis process under fluorescent light demonstrate higher dye degradation rate in compared to under UV light in the first 10 minutes. However, the degradation rate under fluorescent light tends to become constant with 40.32% of dye removal until 60 minutes of the photocatalysis process. On the contrary, it was clearly observed that the dye degradation rate under UV light significantly increased until 20 minutes of the photocatalysis process and subsequently constant with 50% of dye removal up till 60 minutes of process. The result proves that the photocatalytic degradation process under UV light exposure is more efficient in compared to the condition under fluorescent light.

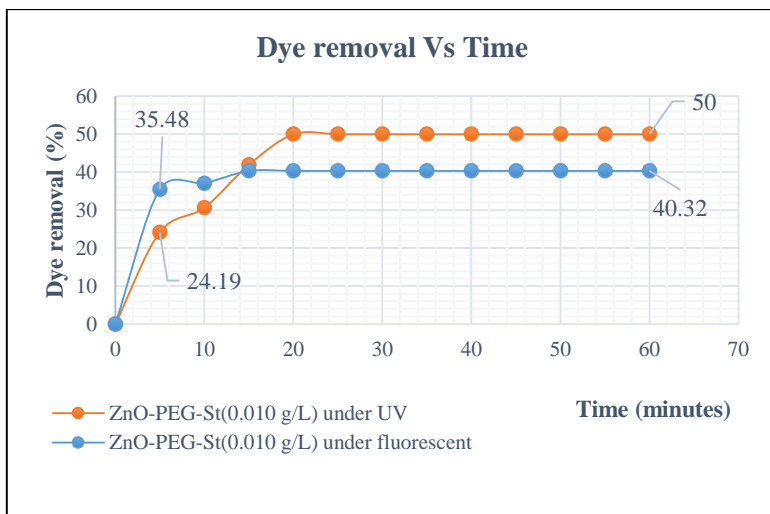


Figure 3.3: Dye removal versus time in the presence of ZnO-PEG-St (0.010 g/L of PEG).

Based on Figure 3.4, the graphs show the increment percentage of dissolve oxygen (DO) versus time for photocatalysis process in the presence of ZnO-PEG-St (0.010 g/L of PEG) under UV and fluorescent light. Dissolve oxygen is refer to the level of free, non-compound oxygen present in water or other liquids (Prasad M.P.D, Sridevi V, Aswini N, 2015). It is an important parameter in assessing water quality because it influences on the organisms living within a body of water. According to Figure 3.4, the percentage of dissolve oxygen for dye wastewater treated under UV and fluorescent light is 49.05% and 3.46%, respectively. The result indicates that photocatalytic degradation process under UV light not only improves the photocatalytic activity, but also increases the dissolve oxygen in water.

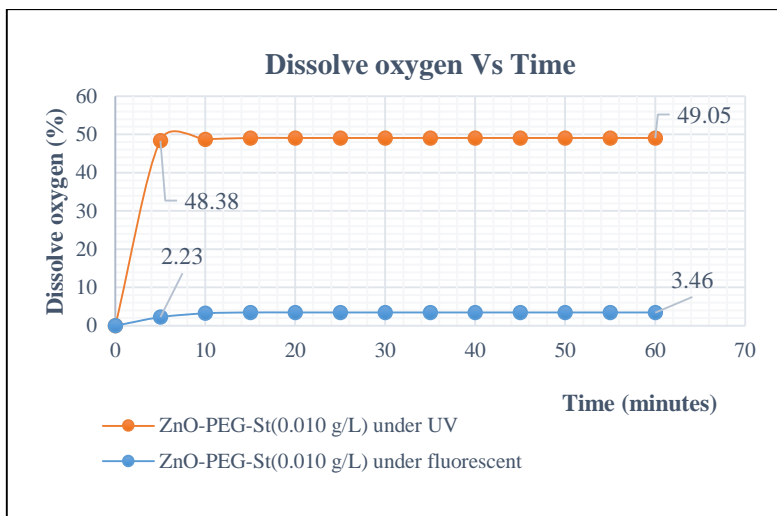


Figure 3.4: Percentage of dissolve oxygen increment versus time for photocatalysis process in the presence of ZnO-PEG-St (0.010 g/L of PEG) under UV and fluorescent light.

Figure 3.5 shows the trend of dye removal during photocatalysis process in the presence of ZnO-PEG-St (0.015 g/L of PEG) in 1-hour duration, under UV and fluorescent light. Under UV light condition, dye degradation rate increased rapidly for the first 15 minutes and consequently constant until 60 minutes of photocatalysis process with the maximum dye removal (56.45%). In contrast, dye degradation is not occurring for the first 10 minutes of photocatalysis process under fluorescent light condition. However, the dye degradation rate was increased after 10 minutes until 25 minutes of the process and become constant up till 1 hour with the maximum dye removal of 48.39%. Based on the results, it can be deduced that the photocatalytic activity of the photocatalyst used under UV light is more efficient than fluorescent light. This is because UV light can increase the photoexcitation of the ZnO-PEG-St faster than fluorescent light. These findings strongly support the results in sub topic

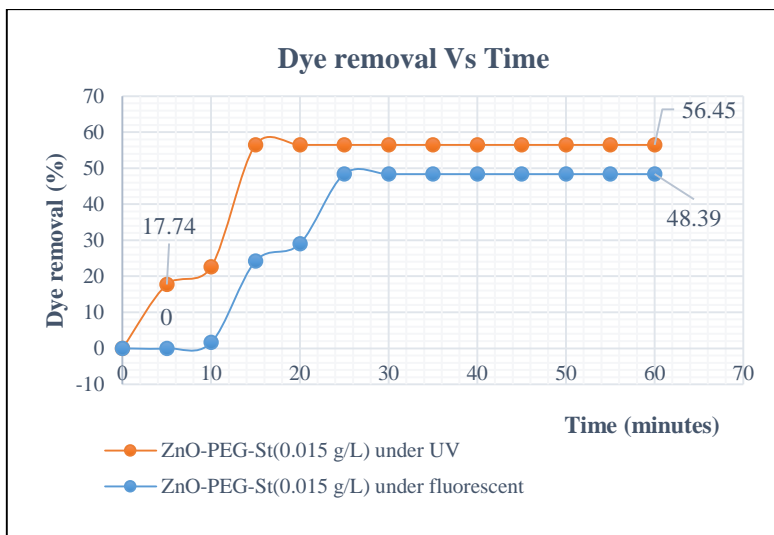


Figure 3.5: Dye removal versus time for photocatalysis process in the presence of ZnO-PEG-St (0.015 g/L of PEG) under UV and fluorescent light.

Based on Figure 3.6, the graphs show the changing pattern of increment percentage of dissolve oxygen versus time for photocatalysis process in the presence of ZnO-PEG-St (0.015 g/L of PEG) under UV and fluorescent. At the 5 minutes, the percentage of dissolve oxygen for ZnO-PEG-St (0.015 g/L of PEG) under UV is 62.88% while 2.23% under fluorescent. It was clearly seen that the percentage of dissolve oxygen for the wastewater treated under UV light is constant at 53.96% while 5.24% for the wastewater under fluorescent. This show that by treat the wastewater under UV is more effective than under fluorescent light. This is because more oxygen level produced after treated under UV.

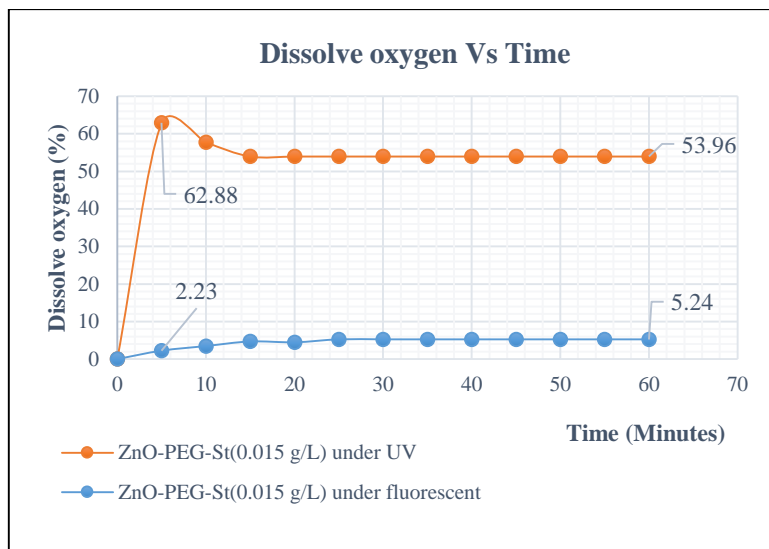


Figure 3.6: Percentage of dissolve oxygen increment versus time for photocatalysis process in the presence of ZnO-PEG-St (0.015 g/L of PEG) under UV and fluorescent light.

To discuss more about the comparison between the light intensity. The percentage degradation of dyes in wastewater improved with increasing exposed light intensity (Meena, R. C.; Pachwarya, R. B.; Meena, 2009). Mondal & Sharma (2014) state that under the elevated intensity of light irradiation, the enhancement was significantly higher since the electron-hole formation is predominant at high irradiation intensity and, therefore, electron-hole recombination probability is in significant. However, when irradiated light intensity becomes very poor, separation of electron-hole pair competes with recombination which consecutively decreases the formation of free radicals, thus, causing less result on the percentage degradation of the waste water. The greater part of photocatalytic degradation studies has been carried out at 600 nm. Furthermore, the amount of dissolve oxygen increases for both photocatalyst during the treatment. However, ZnO-PEG-St under UV light shows the higher increment of dissolve oxygen compare to fluorescent. The result show ZnO-PEG-St (0.015 g/L of PEG) under UV light has better performance compare to other photocatalyst. In conclusion, as the light intensity of UV light is much higher than the

fluorescent light, the photocatalytic degradation of dye wastewater is more suitable conducted under UV light compared to the fluorescent light.

3.1.5 Effect of different photocatalysts

Photocatalyst is a material that acts as catalyst when exposed to light. There are various materials that show photocatalytic capability, such as titanium dioxide (TiO_2), zinc oxide (ZnO), and tin oxide (SnO_2) (He & Zhou, 2013). However, nanosized ZnO has been shown as the most efficient functional materials for photocatalytic applications due to available at low cost, exhibit mild reaction conditions and high photochemical reactivity, while affording the use of UV and fluorescent (Mondal & Sharma, 2014). The photocatalytic reactions happens in such treatment somehow identical to heterogeneous catalysis which includes the simultaneous adsorption of oxygen and organic reactant species present on the waste, followed by the oxidation on the ZnO photocatalyst surfaces. Zinc oxide is a photoactive semiconducting material oxide and able to activate itself by taking energy for the photocatalytic reaction from photons. It also has known as an effective photocatalyst for water detoxification, organic pollutant decomposition and other photolysis because it produces hydrogen peroxide (H_2O_2) more proficiently. However, the performance of different photocatalysts will depend on the types of materials and their preparation method (Hairom et al., 2014 and 2015). Therefore, the efficiency of different ZnO -PEG-St (0.010g/L and 0.015 g/L of PEG) as photocatalyst was investigated in this study to treat the dye wastewater under UV and fluorescent light. Significant of this study is to examine the optimum amount of PEG for preparation method of ZnO -PEG-St nanoparticles.

3.1.6 Photocatalysis under UV light

Figure 3.7 reveals the trend of dye removal against time for photocatalysis process under UV light condition in the presence of different photocatalyst, ZnO-PEG-St (0.010 g/L of PEG) and ZnO-PEG-St (0.015 g/L of PEG). Based on the result, the wastewater contains ZnO-PEG-St (0.010 g/L of PEG) degraded faster for the first 10 minutes with 24.19-30.00% of dye removal. In compared to the presence of ZnO-PEG-St (0.015 g/L of PEG), dye removal was achieved in the range of 17.74-22.00% for the first 10 minutes. However, the dye degradation rate was found to increase rapidly until 15 minutes and consequently constant at 56.45% of dye removal until 60 minutes of photocatalysis process, in the presence of ZnO-PEG-St (0.015 g/L of PEG). For the case of ZnO-PEG-St (0.010 g/L of PEG), it was clearly observed that the dye degradation rate increases slightly after 10 min until 20 min and become constant at 50.00% of dye removal. Therefore, the results proved that the photocatalysis process in the presence of ZnO-PEG-St (0.015 g/L of PEG) is more efficient in compared to ZnO-PEG-St (0.010 g/L of PEG) under the same UV light intensity.

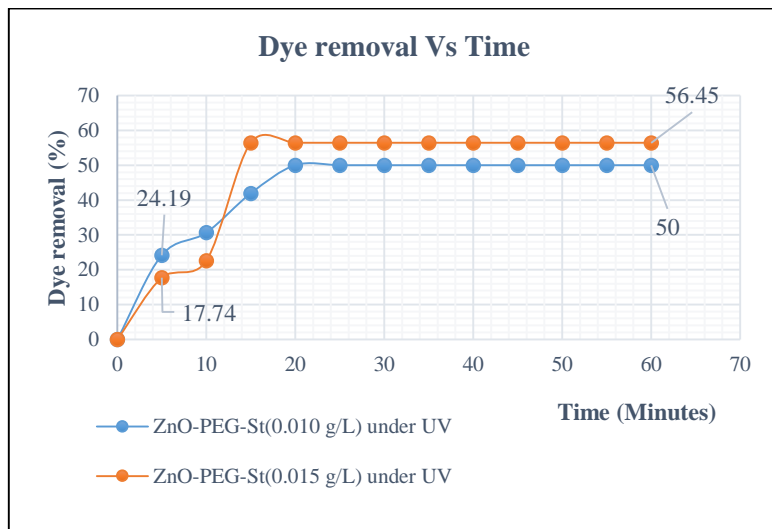


Figure 3.7: Dye removal versus time for photocatalysis process in the presence of ZnO-PEG-St (0.015 g/L and 0.010 g/L of PEG) under UV.

The graphs in Figure 3.8 show the changing pattern of DO increment percentage against time for photocatalysis process under UV light condition in the presence of different photocatalyst. Based on the Figure 3.8, increment percentage of dissolve oxygen for the wastewater in the presence of ZnO-PEG-St (0.010 g/L of PEG) and ZnO-PEG-St (0.015 g/L of PEG) after 5 min is 48.38% and 62.88%, respectively. Consequently, the DO percentage was slightly declined and become constant at 49.05% and 53.96%, respectively starting from 15th min to 60 min. Hence, it was found that the DO increment for photocatalysis process in the presence of ZnO-PEG-St (0.015 g/L of PEG) is higher than ZnO-PEG-St (0.010 g/L of PEG) under ultraviolet (UV) light condition.

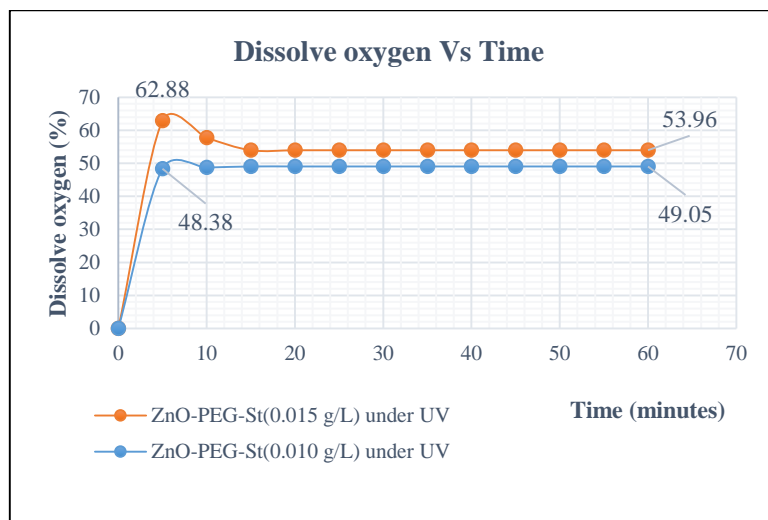


Figure 3.8: Percentage of dissolve oxygen increment versus time for photocatalysis process in the presence of ZnO-PEG-St (0.015 g/L and 0.010 g/L of PEG) under UV.

In the UV light condition, the percentage of dye removal for ZnO-PEG-St contain 0.010 g/L amount of PEG is 50% whilst ZnO-PEG-St contain 0.015 g/L of PEG reads 56.45% of dye removal. ZnO-PEG-St contain 0.015 g/L of PEG can be proved to be more effective compared to ZnO-PEG-St contain 0.010 g/L of PEG under the same UV light. This is because the amount of PEG that act as capping agent influence the effect of photocatalysis process. Based on the literature, capping agent

can solve the serious problems faced in the synthesis of ZnO nanoparticles, which is agglomeration.

In 2013, W. Wang and his co-workers state that one of the way to reduce the agglomeration is by using PEG. Thus, the smallest particles of ZnO nanoparticles can be produce with low tendency of agglomeration. From the result, we can conclude that more amount of PEG can increase the efficiency of the dye removal by reducing the size particle of ZnO nanoparticles. Furthermore, the amount of dissolve oxygen increases for both photocatalyst during the treatment. However, ZnO-PEG-St contain 0.015 g/L of PEG shows the higher increment of dissolve oxygen compare to the ZnO-PEG-St contain 0.010 g/L of PEG. This show the positive result of the experiment for the dye wastewater treatment.

3.1.7 Photocatalysis under fluorescent light

Figure 3.9 demonstrates the trend of dye against time for photocatalysis process under fluorescent light condition in the presence of different photocatalyst, ZnO-PEG-St (0.010 g/L of PEG) and ZnO-PEG-St (0.015 g/L of PEG). Based on the result, the wastewater contains ZnO-PEG-St (0.010 g/L of PEG) degraded faster for the first 10 minutes with 35.48-37.00% of dye removal. In compared to the presence of ZnO-PEG-St (0.015 g/L of PEG), dye removal was achieved in the range of 0-5.00% for the first 10 minutes. However, the dye degradation rate was found to increase rapidly until 30 minutes and consequently constant at 48.39% of dye removal until 60 minutes of photoctalysis process, in the presence of ZnO-PEG-St (0.015 g/L of PEG). For the case of ZnO-PEG-St (0.010 g/L of PEG), it was clearly observed that the dye degradation rate increases slightly after 10 min until 15 min and become constant at 40.32% of dye removal. Therefore, the results proved that the photocatalysis process in the presence of ZnO-PEG-St (0.015 g/L of PEG) is more efficient in compared to ZnO-PEG-St (0.010 g/L of PEG) under the same fluorescent light intensity.

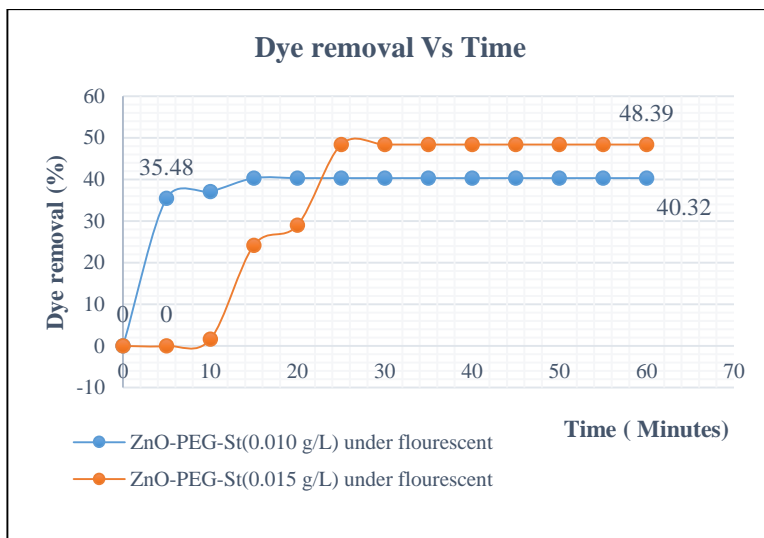


Figure 3.9: Dye removal versus time for photocatalysis process in the presence of ZnO-PEG-St (0.015 g/L and 0.010 g/L of PEG) under fluorescent.

Figure 3.10 demonstrates the trend of percentage of dissolve oxygen against time for photocatalysis process under fluorescent light condition in the presence of different photocatalyst, ZnO-PEG-St (0.010 g/L of PEG) and ZnO-PEG-St (0.015 g/L of PEG). Based on the Figure, increment percentage of dissolve oxygen for the wastewater in the presence of ZnO-PEG-St (0.010 g/L of PEG) and ZnO-PEG-St (0.015 g/L of PEG) after 5 min is 2.33% respectively. The, increment percentage for ZnO-PEG-St (0.010 g/L of PEG) start to become constant after 10 minutes the the value 3.46%. Consequently, the DO percentage was slightly declined at 20 minutes for ZnO-PEG-St (0.015 g/L of PEG) and become constant at 5.24%. Hence, it was found that the DO increment for photocatalysis process in the presence of ZnO-PEG-St (0.015 g/L of PEG) is higher than ZnO-PEG-St (0.010 g/L of PEG) under fluorescent light condition.

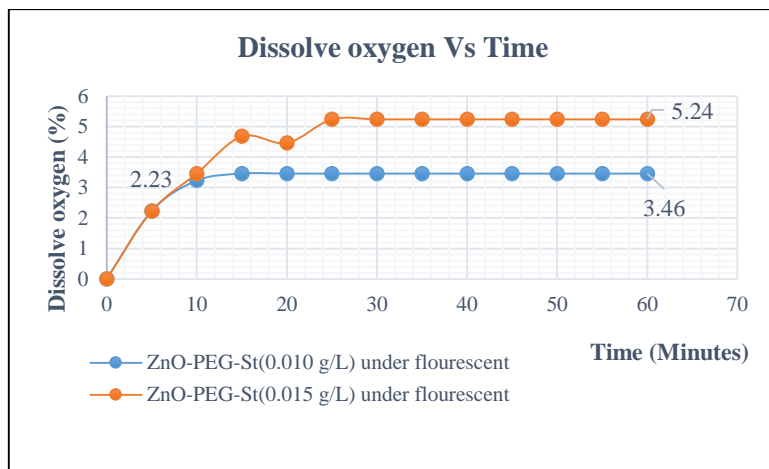


Figure 3.10 Percentage of dissolve oxygen increment versus time for photocatalysis process in the presence of ZnO-PEG-St (0.015 g/L and 0.010 g/L of PEG) under fluorescent

In the fluorescent condition, the percentage of dye removal for ZnO-PEG-St contain 0.010 g/L amount of PEG is 40.32% whilst ZnO-PEG-St contain 0.015 g/L of PEG reads 48.39% of dye removal. The result show that ZnO nanoparticles contain higher amount of PEG can produce better percentage of dye removal because it can increase the surface area of ZnO nanoparticle. Mondal & Sharma, (2014) state that there are more number of atoms resides on the surface, it enhances the adsorption capacity of the photocatalysts towards organic pollutants. The activity of photocatalysis is associated with the time exhausted by electrons and holes to get to the surface of the particles. The higher the surface to volume ratio, smaller the particle diameter and the smaller time may be used up by charge carriers diffusing to the surface from inside. This can provide lesser probability of electron and holes recombination. Therefore, the superior photocatalytic activity can be achieved. Furthermore, the amount of dissolve oxygen increases for both photocatalyst during the treatment. However, ZnO-PEG-St contain 0.015 g/L of PEG shows the higher increment of dissolve oxygen compare to the ZnO-PEG-St contain 0.010 g/L of PEG. This show the positive result of the experiment for the dye wastewater treatment.

3.1.8 Effect of ZnO-PEG-St on pH

The pH value of the aqueous solution is a key parameter for photocatalytic degradation of wastewater and dyes because it affects the adsorption of pollutants that happens at the surface of photocatalysts (Mondal & Sharma, 2014). The wastewater produces from textile generally have a wide range of pH values. Furthermore, the generation of hydroxyl radicals which is necessary for the photocatalytic reaction also depends on pH of the solution (Lawless, Serpone, & Meisel, 1991). Table 3.1 show the PH of ZnO-PEG-St (0.010 g/L and 0.015 g/L of PEG) under fluorescent and UV. At the initial experiment, the pH was maintained at pH 7. Then, the final pH was recorded at the end of experiment. Based on the table 3.1, the range of pH is in the range of 6 to 8.

Table 3.1: pH of ZnO-PEG-St (0.010 g/L and 0.015 g/L of PEG) under fluorescent and UV

Time (minutes)	PH of ZnO-PEG-St (0.010 g/L of PEG)		PH of ZnO-PEG-St (0.015 g/L of PEG)	
	Fluorescent	UV	Fluorescent	UV
0	6.80	6.80	6.80	6.80
5	6.91	6.92	6.91	7.44
10	6.92	6.93	6.91	7.55
15	6.91	6.91	6.92	7.55
20	6.91	6.90	6.92	7.55
25	6.91	6.90	6.91	7.55
30	6.91	6.90	6.91	7.55
35	6.91	6.90	6.91	7.55
40	6.91	6.90	6.91	7.55
45	6.91	6.90	6.91	7.55
50	6.91	6.90	6.91	7.55
55	6.91	6.90	6.91	7.55
60	6.91	6.90	6.91	7.55

Based on the experiment, the initial pH was adjusted to the pH 7. This due to the previous study by Hairom et al., (2014a). Based on the result, the pH was in the range of 6-9. This pH range was suitable to discharge to the environment and follow the standard (Tamime, 2009).

3.2 RECOMMENDATION AND CONCLUSION

3.2.1 Introduction

This chapter discusses the recommendation of the project to give the better impact in the future. Then, the conclusions are drawn based on the project findings and their implications.

3.2.2 Conclusion

Reviewing the recent representative publications, the function of various operating parameters on the photocatalytic decomposition of various organic dyes in wastewater explored in this review. ZnO have been recommended to be efficient photocatalysts for the degradation and mineralisation of various toxic organic pollutants such as azo dyes in wastewater water. In this experiment, ZnO nanoparticles of hexagonal wurtzite structure was completely synthesized by using simple precipitation method in the presence of different amount of PEG (ZnO-PEG-St). ZnO-PEG-St was characterized by using FTIR. The FTIR spectral analysis reveals the characteristics peaks for Zn-O stretching. The absorption of water molecules on the ZnO nanoparticles is confirmed by FTIR spectra. Furthermore, the performance of the different ZnO-PEG-St as photocatalyst for photocatalytic degradation of dyes was studied. The result show that ZnO-PEG-St contain 0.015 g/L of PEG under UV light is better compared to other photocatalyst. The research also discovered that the UV energy gives improved efficiency in degradation of dyes compared to the fluorescent light. This this because the light intensity of UV light much higher compared to the fluorescent light. Oxygen levels showed an increase during the experiment under fluorescent lamps and UV lamps and a higher rise is in a state of UV light.

REFERENCES

- [23] ASTM Akpan, U. G., & Hameed, B. H. (2009). Parameters affecting the photocatalytic degradation of dyes using TiO₂-based photocatalysts: A review. *Journal of Hazardous Materials*, 170(2-3), 520–529. <http://doi.org/10.1016/j.jhazmat.2009.05.039>
- [24] Babu, B. R., Parande, a K., Raghu, S., & Kumar, T. P. (2007). Cotton Textile Processing : Waste Generation and Effluent Treatment. *The Journal of Cotton Science*, 153(11:141), 141–153.
- [25] Banerjee, P., Chakrabarti, S., Maitra, S., & Dutta, B. K. (2012). Zinc oxide nano-particles - Sonochemical synthesis, characterization and application for photo-remediation of heavy metal. *Ultrasonics Sonochemistry*, 19(1), 85–93. <http://doi.org/10.1016/j.ultsonch.2011.05.007>
- [26] Carmen, Z., & Daniela, S. (2010). Textile Organic Dyes – Characteristics , Polluting Effects and Separation / Elimination Procedures from Industrial Effluents – A Critical Overview. *Organic Pollutants Ten Years after the Stockholm Convention - Environmental and Analytical Update*, 55–86. <http://doi.org/10.5772/32373>
- [27] Chen, T., Zheng, Y., Lin, J.-M., & Chen, G. (2008). Study on the photocatalytic degradation of methyl orange in water using Ag/ZnO as catalyst by liquid chromatography electrospray ionization ion-trap mass spectrometry. *Journal of the American Society for Mass Spectrometry*, 19(7), 997–1003. <http://doi.org/10.1016/j.jasms.2008.03.008>
- [28] Dong, Y., Su, Y., Chen, W., Peng, J., Zhang, Y., & Jiang, Z. (2011). Ultrafiltration enhanced with activated carbon adsorption for efficient dye removal from aqueous solution. *Chinese Journal of Chemical Engineering*, 19(5), 863–869. [http://doi.org/10.1016/S1004-9541\(11\)60066-9](http://doi.org/10.1016/S1004-9541(11)60066-9)
- [29] Hairom, N. H. H. (2009). *Facile Synthesis of a Nanosized Zinc Oxide For Photocatalytic Degradation of Methyl Orange*. Universiti Teknologi Malaysia.
- [30] Hairom, N. H. H., Mohammad, A. W., & Kadhum, A. A. H. (2015). Influence of zinc oxide nanoparticles in the nanofiltration of hazardous Congo red dyes. *Chemical Engineering Journal*, 260, 907–

915. <http://doi.org/10.1016/j.cej.2014.08.068>

[31] Hairom, N. H. H., Mohammad, A. W., Ng, L. Y., & Kadhum, A. A. H. (2014a). Effect of various zinc oxide nanoparticles in membrane photocatalytic reactor for Congo red dye treatment. *SEPARATION AND PURIFICATION TECHNOLOGY*, 137, 74–81. <http://doi.org/10.1016/j.seppur.2014.09.027>

[32] Hairom, N. H. H., Mohammad, A. W., Ng, L. Y., & Kadhum, A. A. H. (2014b). Utilization of self-synthesized ZnO nanoparticles in MPR for industrial dye wastewater treatment using NF and UF membrane. *Desalination and Water Treatment*, (May), 1–12. <http://doi.org/10.1080/19443994.2014.917988>

[33] He, Z., & Zhou, J. (2013). Synthesis , Characterization , and Activity of Tin Oxide Nanoparticles : Influence of Solvothermal Time on Photocatalytic Degradation of Rhodamine B, *2013*(September), 13–18.

[34] Jin, Y., Wang, J., Sun, B., Blakesley, J. C., & Greenham, N. C. (2008). Solution-processed ultraviolet photodetectors based on colloidal ZnO nanoparticles. *Nano Letters*, 8(6), 1649–1653. <http://doi.org/10.1021/nl0803702>

[35] Kanade, K. G., Kale, B. B., Aiyer, R. C., & Das, B. K. (2006). Effect of solvents on the synthesis of nano-size zinc oxide and its properties. *Materials Research Bulletin*, 41(3), 590–600. <http://doi.org/10.1016/j.materresbull.2005.09.002>

[36] Khan, R., Hassan, M. S., Cho, H. S., Polyakov, A. Y., Khil, M. S., & Lee, I. H. (2014). Facile low-temperature synthesis of ZnO nanopyramid and its application to photocatalytic degradation of methyl orange dye under UV irradiation. *Materials Letters*, 133, 224–227. <http://doi.org/10.1016/j.matlet.2014.07.006>

[37] Kołodziejczak-Radzimska, A., & Jesionowski, T. (2014). Zinc Oxide—From Synthesis to Application: A Review. *Materials*, 7(4), 2833–2881. <http://doi.org/10.3390/ma7042833>

[38] Konstantinou, I. K., & Albanis, T. a. (2004). TiO₂-assisted photocatalytic degradation of azo dyes in aqueous solution: Kinetic and mechanistic investigations: A review. *Applied Catalysis B: Environmental*, 49(1), 1–14.

[39] Lawless, D., Serpone, N., & Meisel, D. (1991). Role of

hydroxyl radicals and trapped holes in photocatalysis. A pulse radiolysis study. *The Journal of Physical Chemistry*, 95(13), 5166–5170. <http://doi.org/10.1021/j100166a047>

[40] Lu, F., Cai, W., & Zhang, Y. (2008). ZnO hierarchical micro/nanoarchitectures: solvothermal synthesis and structurally enhanced photocatalytic performance. *Advanced Functional Materials*, 18(7), 1047–1056.

[41] Meena, R. C.; Pachwarya, R. B.; Meena, V. K. . S. A. (2009). Degradation of textile dyes Ponceau-S and Sudan IV using recently developed photocatalyst, immobilized resin dowex-11. *American Journal of Environmental Sciences*, 5(3), 444–450.

[42] Mondal, K., & Sharma, A. (2014). Photocatalytic Oxidation of Pollutant Dyes in Wastewater by TiO₂ and ZnO nano-materials – A Mini-review, 36–72.

[43] Mustafa, N., & Nakib, H. A. L. (2013). Reverse Osmosis Polyamide Membrane for the Removal of Blue and Yellow Dye from Waste Water, 14(2), 49–55.

[44] Nomura, K., Shibata, N., & Maeda, M. (2002). Orientation control of zinc oxide films by pulsed current electrolysis. *Journal of Crystal Growth*, 235(1-4), 224–228. [http://doi.org/10.1016/S0022-0248\(01\)01773-0](http://doi.org/10.1016/S0022-0248(01)01773-0)

[45] Prasad M.P.D, Sridevi V, Aswini N, V. K. R. A. and S. P. . D. (2015). Treatment of f Sugar Industry Effluent using Microbial Fuel Cells, 7522(June), 247–251.

[46] Rashed, M. N. (2013). Adsorption Technique for the Removal of Organic Pollutants from Water and Wastewater. *Organic Pollutants - Monitoring, Risk and Treatment*, 167–194.

[47] Saravanan, L., Diwakar, S., & Mohankumar, R. (2011). Synthesis, Structural and Optical Properties of PVP Encapsulated CdS Nanoparticles. *Nanomaterials and*, 1(2), 42–48. Retrieved from <http://hrcak.srce.hr/file/114166>

[48] Sekiguchi, T., Miyashita, S., Obara, K., Shishido, T., & Sakagami, N. (2000). Hydrothermal growth of ZnO single crystals and their optical characterization. *Journal of Crystal Growth*, 214, 72–76. [http://doi.org/10.1016/S0022-0248\(00\)00065-8](http://doi.org/10.1016/S0022-0248(00)00065-8)

- [49] Tamime, A. Y. (2009). *Cleaning-in-Place: Dairy, Food and Beverage Operations*. Wiley. Retrieved from https://books.google.com.my/books?id=oLA_91Wn7R8C
- [50] Thiruvengkatachari, R., Vigneswaran, S., & Moon, I. (2008). A review on UV/TiO₂ photocatalytic oxidation process (Journal Review). *Korean Journal of Chemical Engineering*, 25(1), 64–72. <http://doi.org/10.1007/s11814-008-0011-8>
- [51] Tripathy, N., Ahmad, R., Eun Song, J., Ah Ko, H., Hahn, Y.-B., & Khang, G. (2014). Photocatalytic degradation of methyl orange dye by ZnO nanoneedle under UV irradiation. *Materials Letters*, 136, 171–174. <http://doi.org/10.1016/j.matlet.2014.08.064>
- [52] Vafaezadeh, M., & Hashemi, M. M. (2015). Polyethylene glycol (PEG) as a green solvent for carbon–carbon bond formation reactions. *Journal of Molecular Liquids*, 207, 73–79. <http://doi.org/10.1016/j.molliq.2015.03.003>

CHAPTER 4

MATERIALS PROCESSING AND CHARACTERIZATION IN BIODEGRADABLE IMPLANTS DEVELOPMENT

*Ahmad Kafrawi Nasution*¹, *Abdul Hakim Md Yusop*²,
Muhammad Hanif Ramlee^{2,3}

¹Department of Mechanical Engineering,
Faculty of Engineering,
Muhammadiyah University of Riau, Pekanbaru, Riau,
Indonesia.

²Medical Devices and Technology Center (MEDITEC),
Institute of Human Centered Engineering (iHumen),
Universiti Teknologi Malaysia,
81310 UTM Johor Bahru, Johor, Malaysia.

³Bioinspired Innovation Group (BIOINSPIRA),
School of Biomedical Engineering and Health Sciences,
Faculty of Engineering,
Universiti Teknologi Malaysia,
81310 UTM Johor Bahru, Johor, Malaysia.

4.1 INTRODUCTION

Current metal biomaterials for biomedical applications tend to use a lot of prosthetic devices (prosthetic devices) to help, repair and regeneration of damaged tissue. Metallic biomaterials can be used as a permanent function or temporary functions. However, metal biomaterials is still in need of repairs and improvements in biocompatibility and biofunctionality [1]. Several researches conducted to study the behavior of metallic implants in order to improve the biocompatibility in the last few years [2, 3]. Recent studies on the in vivo have shown that metal ions and particles are separated due to the friction of the implant that can cause damage to the soft tissue [4]. General agreement that the important factors affecting the longevity of orthopedic implants are the release of

metal ions from the implant [4-6], formation of debris associated with the problem of tissue inflammation, bone loss and loosened implant [7]. Therefore, efforts should be made is the improvement of the mechanical properties.

In titanium (Ti) and its alloys have been carried out efforts to improve the mechanical properties by controlling processing conditions [8]. The processing is done by the application of treatment and the addition of numbers of elements [1, 9-13]. Some of the treatment given to the Ti alloy can change its properties such as texture control, heat treatment (aging) as well as combination deformation-heat treatment [1, 11]. The deformation process often given in Ti alloys includes equal channel angular pressing (ECAP), accumulative roll bonding (ARB) and high pressure torsion (HPT) [1]. Table 4.1 showing the effect of elements on titanium (Ti) and its alloys which gives an effect on the cost production and ease of implant is removed.

Table 4.1: Selection of titanium (Ti) and its alloys based on the consumption of the elements against the cost (high and low) and removable implants [1]

Ti alloys with consumption of high cost elements	Ti alloys with consumption of low cost elements	Ti alloys for removable implants
Ti-13Nb-13Zr	Ti-10Cr-Al	Ti-Zr-Nb
Ti-12Mo-6Zr-2Fe (TMZF) (ASTM F1813)	Ti-Mn-Fe	Ti-Zr-Nb-Ta
Ti-15Mo (ASTM F2066)	Ti-Mn-Al	Ti-Zr-Al-V
Ti-16Nb-10Hf (Tiadyne 1610)	Ti-Cr-Al	Ti-30Zr-5Mo
Ti-15Mo-5Zr-3Al	Ti-Sn-Cr	Ti-30Zr-7Mo
Ti-35.5Nb-7.1Zr-5.1Ta (TNZT)	Ti-Cr-Sn-Zr	Ti-30Zr-5Cr
Ti-29Nb-13Ta-4.6Zr (TNTZ)	Ti-(Cr, Mn)-Sn	Ti-30Zr-3Cr-3Mo
Ti-Nb-In	Ti-12Cr	
Ti-24Nb-4Zr-7.9Sn (Ti2448)		
Ti-Cr-Sn-Zr		
Ti-Zr-Cr		
Ti-Zr-Mo		
Ti-Zr-Mo-Cr		

4.2 BIODEGRADABLE METALS

4.2.1 Definition and Concept of Biodegradable Metals

The term “biodegradable metal” (BM) has been used worldwide and there were many new findings reported over the last decade [14]. Hopefully, the advent of this new implant materials can support the healing process of diseased tissue or organ and subsequently degraded slowly [15]. Definition of biodegradable metals (BMs) according to Li, Zheng et al. 2014 is a metals that were expected to corrode in vivo, where the corrosion products of metals provide response corresponding to the "host" and dissolve completely upon fulfilling the mission to assist the tissue healing with no implant residues [16].

From the point of view of materials science, biodegradable metals can be classified as follows: [14]

- **“Pure metals” (BMs-PM)** is a metal with one metallic element with impurity levels lower than the commercial tolerance limits.
- **“Biodegradable alloys” (BMs-BA)** is a metal with various microstructures and one or more alloying elements.
- **“Biodegradable metal matrix composites” (BMs-MC)** is all the components forming biodegradable composites have a category of the materials are non-toxic to the body.

Li, Zheng et al. 2014 said the development of new materials along with the improvement of living standards and expectations of quality of life [16]. In other clinical applications only require temporary support to the healing process of tissue [16], therefore, required new materials. Such support is only derived from material made of degradable biomaterials [15, 17]. Biodegradable concept has long been known, for example in biodegradable polymer sutures [16]. There are two degradable biomaterial implants that have been proposed: biodegradable polymers and biodegradable metals [15]. However, biodegradable polymers have biomechanical limitation compared to biodegradable metals [18]. On the other hand, biodegradable metals have both the strength and the ability to degrade [19]. During the past several years, biodegradable metals were used as a temporary implant material for vascular intervention and osteosynthesis [20-26].

4.2.2 Magnesium-based biodegradable metals

When viewed from the alloying elements, there are three major groups of magnesium alloys including pure magnesium (pure Mg), magnesium alloys with the main alloying elements Al and alloys magnesium free of alloying elements Al [27-30].

4.2.3 Pure magnesium

Pure magnesium is magnesium with other elements (impurities) within tolerance limit. If impurities exceed the tolerance limit, the corrosion rate will increase [31, 32]. The corrosion resistance of pure magnesium is higher by improving the grain size through forging or rolling and heat treatment [32]. The heating temperature and the length of time of the heat treatment must be considered properly. Otherwise, it would get the opposite result [32].

Therefore pure magnesium demonstrated the ability to stimulate new bone formation, Huang, Ren et al and Gao, Qiao et al still worrying about its mechanical properties in orthopedic applications [33, 34]. Li and Zheng said that the pure magnesium is not the right material for biodegradable vascular stents [32].

4.2.4 Magnesium alloys with the main alloying elements Al

Types of magnesium alloys containing elements of Al are AZ91, AZ31, AE21, Calcium (Ca) modified AZ alloys and AE42 [35, 36]. LAE442 alloy is the development of magnesium alloys (AE42) with low density but it will increase the ductility and corrosion resistance [37].

Additional of Mn increase the ductility and corrosion control with bind Fe (adverse effect from Fe on the corrosion behavior) [30]. Addition of Zn can form a solid solution strengthening [35] to increase strength and castability [30]. However, when combined with Al larger ($> 2\text{wt.}\%$) it result in embrittlement [36]. Other alloying elements in magnesium alloys containing Al is Lithium. Lithium has unique properties which are able to change the lattice structure of the HCP into BCC in magnesium alloys [38].

4.2.5 Free-Al Magnesium alloy

Magnesium alloys with free-Al are WE, MZ, WZ and Mg–Ca alloys [30]. The addition of some elements such as Yttrium (Y), zirconium (Zr), Zinc (Zn) and RE almost certain to improve the properties (creep resistance, high temperature stability and forgingability) of the alloy in transportation industry applications [35, 36].

4.2.6 Iron-based biodegradable metals

Pure Fe and Fe based alloys have been developed as biodegradable metals other than Mg and Mg based alloys [1]. From the point of view of structure, Mg and Mg based alloys do not always meet the mechanical properties while pure Fe and Fe based alloys have higher strength [1, 39, 40]. Pure Fe and Fe based alloys are considered as candidate to be used as an alternative to biodegradable implant material [26, 41-44].

The results of pure Fe in vivo tests showed no toxicity [45]. But the results of in vitro showed the concentration of iron ions in the body should not be more than 50 µg/ml because it will cause toxicity and cell death [44, 46]. One thing to note is the excessive degradation after implantation of pure iron at the organism. This is because it is dangerous for the healing of wounds, especially in the early stages of operation [42, 47].

4.3 MATERIALS PROCESSING

Currently, processing material reliable cannot be separated from the increased mechanical properties, alloy design advances (the influence of alloying elements) and process optimization [8, 48]. Magnesium and its alloys still have some issues that should be considered as limited mechanical properties and the problems with low corrosion resistance [49]. Attempts have been made regarding the development of magnesium and its alloys by reducing and controlling the corrosion rate and maintaining biocompatibility [49]. Generally, there are two ways to improve the corrosion behavior of magnesium and its alloys: (a) adjusting the composition and microstructure, including grain size [29, 50] and texture [51] from base material (not only of alloys) [52], but through development of optimal methods of production and availability

of raw materials [53]; (b) conducting a surface treatment or coating [54] such as using ceramic, polymer or composite layer [49].

Arrangements the chemical composition of Mg and its alloys has been carried out since 1990 for transportation applications and recent years, particular researchers of biomaterials were interested in developing a variety of medical devices made from Magnesium alloys [20, 28, 55-66].

The corrosion resistance of pure magnesium is higher by improving the grain size through forging or rolling and heat treatment [32]. As for magnesium alloys with main alloying element Al commonly formed complex compounds to solid solution strengthening, precipitation strengthening and grain-boundaries strengthening [30]. The addition of the element Rare earths (RE) in the magnesium alloys with main alloying element Al and magnesium alloys with free-Al have several contributions such as strengthening, raising the creep resistance, increasing corrosion resistance [67], forgingability [35, 36] and all efforts made to improve services Mg alloys in the transportation industry [35, 36, 67]. Based on research, recommended types magnesium alloys used for biomedical use in human is magnesium alloys free-Al without harmful elements such as RE [68]. Therefore, good alloys element candidates to be used in biomedical magnesium alloys include Ca, Mn and Zn [63, 69, 70].

While efforts were made to pure Fe and Fe based alloys is to increase the degradation rate is still very low and considered to have the same reaction with a permanent implant [42, 71]. Development of research results of pure Fe and Fe based alloys is still of concern to such as the attainment of the level of degradation, mechanical performance and maintaining biocompatibility [71]. To get the appropriate design, there are several things that must be considered like manufacturing process, selection of elements alloys [39, 42, 45] and heat treatment to control the grain size [1, 39, 72].

For other biodegradable metals such as Zn a metallic element that is important and second most widely found in the human body [73]. Currently, Zinc is used as an alloying element, especially in biodegradable metal Mg-based [16]. Efforts made to alter the mechanical properties of pure Zn by adding alloying elements and adjustment microstructure through mechanical deformation [16]. The mechanical deformation effective to improve the mechanical properties and corrosion properties of biodegradable metal are rolling (hot/cold), extrusion, equal-channel angular pressing (ECAP), high pressure torsion (HPT), drawing and forging can be seen in Figure 4.1 [14, 57, 74].

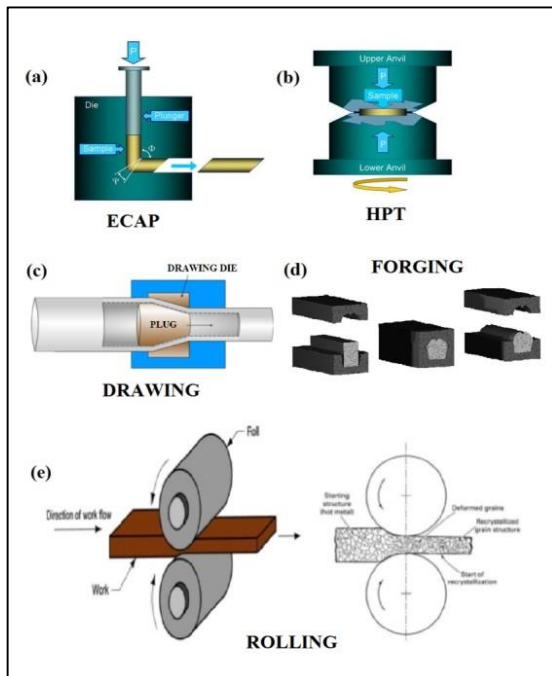


Figure 4.1: Schematic mechanical deformation for biodegradable metals

Materials processing can be selected based on specific application [75]. An example is the friction welding process. Nasution, Murni et al. 2014 has done a friction welding between pure Fe (biodegradable metal) and SS316L (inert metal) for treating temporary clinical problems such as bone fracture [76]. Friction welding has a number of advantages such as low heat input, narrow heat-affected zone (HAZ), and low residual stresses [76] and distortion [75-77]. The results of the connection of welding dissimilar materials can be seen in Figure 4.2.

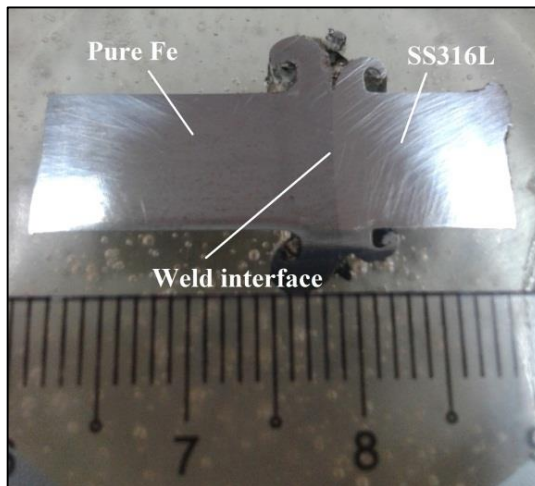


Figure 4.2: Dissimilar metals were joined through the friction welding

4.4 CHARACTERIZATION

4.4.1 Potentiodynamic polarization test (PDP)

The most commonly used technique to evaluate the degradation behaviour of the biodegradable metallic implants is potentiodynamic polarization test. The PDP plays a vital role in determining and quantifying the mechanistic corrosion of the biodegradable metals in simulated body fluid (SBF). An external voltage is applied by a potentiostat and the corresponding current density on the working

electrode (samples) is monitored. 3-electrodes set up are often used in the test comprising of a reference electrode (Ag/AgCl, saturated Calomel), an auxiliary electrode (Graphite, Platinum) and a working electrode (tested samples). The reference electrode is used to measure the working electrode potential. A reference electrode should have a constant electrochemical potential as long as no current flows through it. The auxiliary/counter electrode functions to provide a complete circuit allowing current to flow between the working electrode [78]. Figure 4.3 shows the 3-electrodes configuration for the PDP test in estimating the corrosion rate of the biodegradable metals.

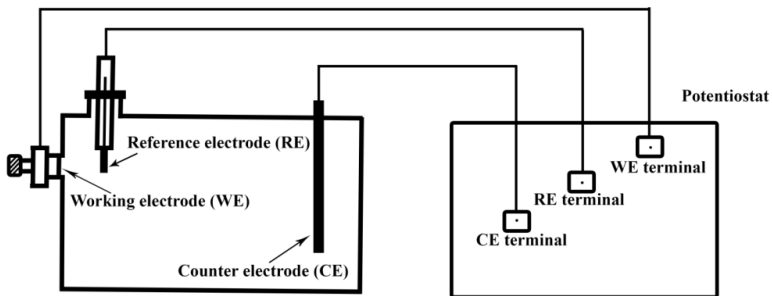


Figure 4.3: 3-electrodes set-up for the potentiodynamic polarization test

4.4.1.1 Interpretation of the PDP curves

The PDP curves could provide a quantitative interpretation on the corrosion rate of the different samples, as shown in Figure 4.4. Qualitatively, from the Figure 4, corrosion rate of sample A is higher than that of sample B and sample C in the order of sample A > sample B > sample C, as the curve of sample A resides at the rightmost indicating the highest current density, i_{corr} . Current density measures the electrical current flowing through the exposed area of the working electrode.

Tafel slopes are constructed on both the anodic and cathodic branches of the polarization curves and the slopes can be extrapolated back to the open-circuit corrosion potential to give a corrosion current density. Quantitatively, the current density of the sample A, sample B and sample C are about 6.9×10^{-6} , 2.3×10^{-6} , and 6×10^{-7} A/cm²,

respectively, determined by the Tafel extrapolation method. The corrosion rate is directly proportional to the current density.

Through the PDP curve as well, the corrosion potential E_{corr} can be quantified. It is a potential at which the rate of oxidation is exactly equal to the rate of reduction. At this potential, the anodic currents and cathodic currents are equal in magnitude and hence no net current could be measured. At this potential, all electrons generated by oxidation metal in dissolution reaction are consumed by oxidant reduction reaction on the same metal surface.

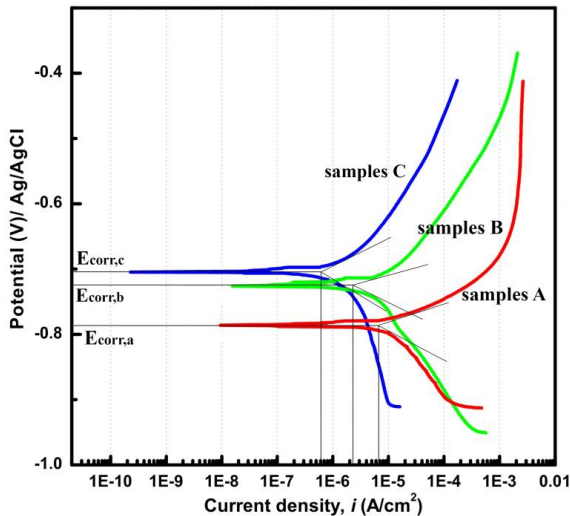


Figure 4.4 Determination of corrosion potential and corrosion current density through Tafel extrapolation technique.

The corrosion current density determined from the Tafel extrapolation method then will be used to calculate the corrosion rate of the corroding metals. Based on the ASTM G59–97 (2014), the corrosion rate can be estimated by the following expression

$$CR = 3.27 \times 10^3 \cdot \frac{i_{corr}}{\rho} EW$$

where i_{corr} = corrosion current density ($\mu\text{A}/\text{cm}^2$), EW = equivalent weight

and ρ = density.

ASTM G59 – 97 (2014) and ASTM G5 – 14 are utilized as the guidance to conduct the PDP test and to analyse the results obtained

The quantification of the corrosion rates of the biodegradable metals in the implant application researches is an indispensable aspect since the degradation rate should be monitored over the implantation period so as it tailors with the tissue healing time [79]. In many biodegradation studies, the corrosion rates of pure Fe, pure Mg, Fe-based alloys and Mg-based alloys have been determined by the PDP test through the Tafel extrapolation method [80-83]

4.4.2 Electrochemical impedance spectroscopy (EIS)

Electrochemical impedance spectroscopy is one of the vital techniques in characterizing the corrosion behaviour of the biodegradable metals, particularly for the coated metals. In EIS, the frequency is applied by the potentiostat and the corresponding impedances are obtained.

In recent years, EIS have been of great interests in the study of corrosion system whereby it has been used effectively to measure the polarization resistance for corrosion systems. It is very useful in order to characterize a coated metal substrate by analysing two occurrences: (1) the deterioration of the coating due to electrolyte exposure (2) the increase or change in corrosion rate of the underlying substrate due to the deterioration or delamination of the coating and subsequent attack by the electrolyte. In EIS, the electrochemical interaction at electrode - electrolyte interface can be characterized by an analogous electronic equivalent circuit consisting of a specific combination of resistors and capacitor. The equivalent circuits are constructed after getting the data of applied frequencies (f), imaginary impedances (Z_i), real impedances (Z_{real}), absolute impedances ($|Z|$) and phase angles (θ) with the aid of special software. Simply speaking, an equivalent circuit transforms the frequency response data to corrosion properties in terms of resistance and impedance.

Nyquist plot gives the plot of the real part of impedance against the imaginary part. This plot gives a quick overview of the data and provides some qualitative interpretations from the shape of the curves. Another plot, called Bode plot indicates the absolute impedances, $|Z|$ and the phase angles, θ of the impedances, each as a function of frequency. Figure 4.5 shows the typical equivalent circuit of an organic coating on a metal substrate.

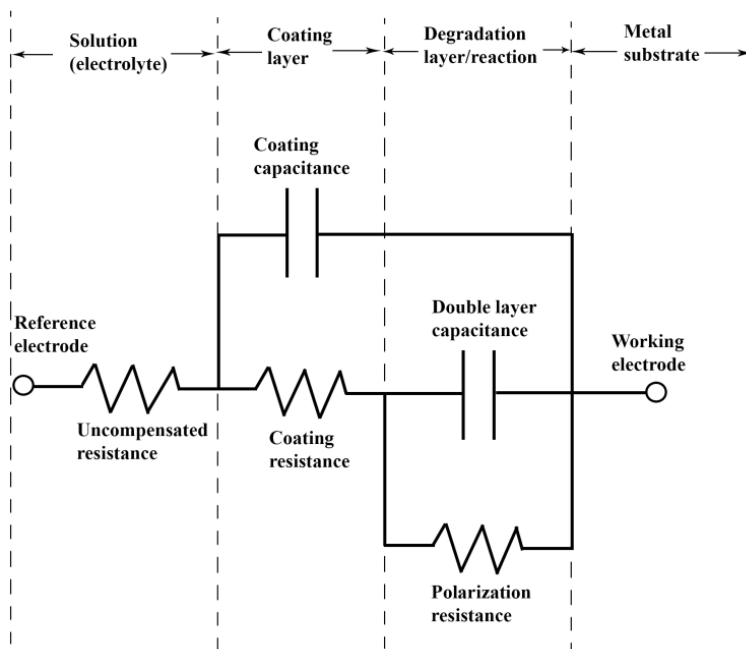


Figure 4.5 Typical equivalent circuit of a coated metal

It is noteworthy to define some important parameters in the EIS.

a) Ohmic resistance ($R\Omega$)

Ohmic resistance or so-called uncompensated resistance is the potential drop between the reference electrode and the working electrode. It depends on the conductivity of the electrolyte and the geometry of the electrode as well.

b) Pore resistance, R_{po}

R_{po} is a resistance developed by the organic coating. It may indicate the coating's porosity as the resistance will decrease once the coating experienced an increase of porosity.

c) Polarization resistance, R_p

The corrosion rate of the metal substrate beneath the coating can be interpreted by the R_p . High R_p of a metal implies high corrosion resistance. The value of R_p can be estimated through the equivalent circuit modelled.

d) Coating capacitance, C_c

The C_c is an important parameter in analysing the coating failure. For polymer-coated metal, the coating capacitance is given by:

$$C_c = \frac{\epsilon\epsilon_0}{d} A$$

Where, ϵ is the dielectric constant of the coating, ϵ_0 is the dielectric constant of vacuum, A is the area of the coating, d is the thickness of the coating. When water penetrates the coating, its dielectric constant increases, leading to an increase of coating capacitance. Hence, the coating capacitance can be utilized to measure the water uptake by the coating.

e) Double layer capacitance, Cdl

Cdl is the capacitance at which the corrosion reaction takes place. It may indicate the delamination or deterioration of the coating.

f) Constant Phase Element, CPE

In some cases, CPE is used in replacing the capacitance considering the deviation from ideal capacitor behaviour owing to the certain heterogeneity of the electrode surfaces.

$$CPE = \frac{1}{Y_0(j\omega)^n}$$

where, Y_0 is the admittance of an ideal capacitance and n is an empirical constant, ranging from 0 to 1. When $n=1$, the CPE behaves as a pure capacitor, while when $n=0$, the CPE behaves a pure resistor.

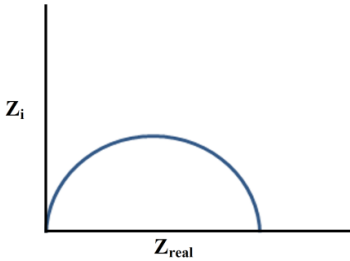
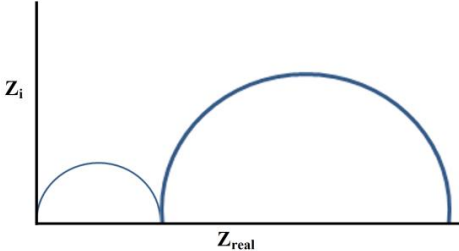
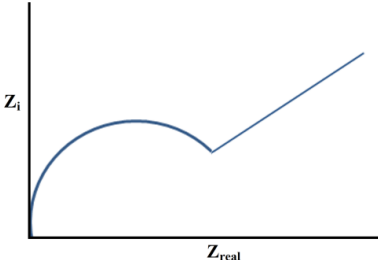
g) Warburg Impedance, W

The diffusion of ionic species at the metal-electrolyte interface is modelled by the Warburg impedance. Warburg impedance is characterized by having identical real and imaginary contributions, resulting in a phase angle of 45° in a Bode plot. The Warburg impedance is determined by the following expression;

$$W = \frac{1}{Y_0\sqrt{j\omega}}$$

where, Y_0 is the diffusion admittance.

Table 4.2: Shows typical Nyquist plots in the case of organic coated-metal being immersed in an electrolyte indicating the electrochemical interaction at metal-electrolyte interface.

Nyquist plots	Description
 <p>A Nyquist plot with the imaginary impedance Z_i on the vertical axis and the real impedance Z_{real} on the horizontal axis. The plot shows a single, symmetric semicircle in the lower half-plane, starting from the origin and ending on the positive real axis.</p>	<ul style="list-style-type: none"> • Development of a low pore resistance, R_{po} • Penetrating of the electrolyte via the pore channel to the surface of the underlying metal.
 <p>A Nyquist plot with the imaginary impedance Z_i on the vertical axis and the real impedance Z_{real} on the horizontal axis. The plot shows two overlapping semicircles in the lower half-plane. The first is a smaller semicircle on the left, and the second is a larger semicircle on the right, partially overlapping the first.</p>	<ul style="list-style-type: none"> • Two impedance loops • First smaller loop indicates coating capacitance C_c and second loop postulates double layer capacitance C_{dl}
 <p>A Nyquist plot with the imaginary impedance Z_i on the vertical axis and the real impedance Z_{real} on the horizontal axis. The plot shows a semicircle in the lower half-plane that transitions into a straight line with a 45-degree slope, extending into the fourth quadrant.</p>	<ul style="list-style-type: none"> • Warburg impedance indicated by the 45°- slope line. • Diffusion of the electrolyte ionic species on the metal surfaces.

There have been intense uses of the EIS in studying the corrosion behaviour of the biodegradable metals particularly of the coated metals. An EIS study has been conducted on PLA coated- AZ91 magnesium alloy samples. The degradation resistance created by the PLA coating were evaluated by examining the changes in the Nyquist plots at predetermined time intervals [84]. Another EIS study by Zomorodian et

al. employed a composite coating comprising of polyether imide PEI, diethylene triamine and hydroxyapatite applied on AZ31 magnesium alloys. The coating performance was evaluated using EIS technique for 88 days by analysing the changes in the absolute impedances, $|Z|$ and the phase angles, θ of the impedances through the Bode plots [85]. Very recently, both Nyquist plot and Bode plot have been analysed in an EIS study to investigate the degradation behaviour of Fe-Au and Fe-Ag composite biodegradable stents [83].

4.5 CONCLUSION

This chapter has presented a brief report on material processing and characterization in the development of current biodegradable implants. Although this chapter is intended as an a preliminary introduction to the processing of materials and the characterization of biodegradable implants includes the measurement and determination of the corrosion rate of biodegradable implants. Measurement and determination of corrosion rates using potentiodynamic polarization tests and electrochemical impedance spectroscopy are currently widely used by researchers in the field of biomaterials.

ACKNOWLEDGEMENT

This work was supported the Ministries of Research, Technology, And Higher Education Republic of Indonesia through Director of Research and Community Service with contract number: 009/L10/AK.04/KONTRAK-PENELITIAN/2019. Apart from that, This work was financially supported by the Universiti Teknologi Malaysia under the Research University Grant (20H20, 4J358, 15J84 and 20H26), Ministry of Energy, Science, Technology, Environment and Climate Change (EF0618I1166 and 4S144) Fundamental Research Grant Scheme (FRGS) Ministry of Education Malaysia (278784-294883).

REFERENCES

- [1] M. Niinomi, M. Nakai, and J. Hieda, "Development of new metallic alloys for biomedical applications," *Acta Biomaterialia*, vol. 8, pp. 3888-3903, 2012.
- [2] R. F. V. V. Jaimes, M. L. C. d. A. Afonso, S. O. Rogero, S. M. L. Agostinho, and C. A. Barbosa, "New material for orthopedic implants: Electrochemical study of nickel free P558 stainless steel in minimum essential medium," *Materials Letters*, vol. 64, pp. 1476-1479, 2010.
- [3] S. S. M. Tavares, F. B. Mainier, F. Zimmerman, R. Freitas, and C. M. I. Ajus, "Characterization of prematurely failed stainless steel orthopedic implants," *Engineering Failure Analysis*, vol. 17, pp. 1246-1253, 2010.
- [4] J. C. Walker, R. B. Cook, J. W. Murray, and A. T. Clare, "Pulsed electron beam surface melting of CoCrMo alloy for biomedical applications," *Wear*, vol. 301, pp. 250-256, 2013.
- [5] Y. Yan, A. Neville, and D. Dowson, "Tribo-corrosion properties of cobalt-based medical implant alloys in simulated biological environments," *Wear*, vol. 263, pp. 1105-1111, 2007.
- [6] Z. Doni, A. C. Alves, F. Toptan, J. R. Gomes, A. Ramalho, M. Buciumeanu, *et al.*, "Dry sliding and tribocorrosion behaviour of hot pressed CoCrMo biomedical alloy as compared with the cast CoCrMo and Ti6Al4V alloys," *Materials & Design*, vol. 52, pp. 47-57, 2013.
- [7] L. Casabán Julián and A. Igual Muñoz, "Influence of microstructure of HC CoCrMo biomedical alloys on the corrosion and wear behaviour in simulated body fluids," *Tribology International*, vol. 44, pp. 318-329, 2011.
- [8] B. Patel, G. Favaro, F. Inam, M. J. Reece, A. Angadji, W. Bonfield, *et al.*, "Cobalt-based orthopaedic alloys: Relationship between forming route, microstructure and tribological performance," *Materials Science and Engineering: C*, vol. 32, pp. 1222-1229, 2012.

- [9] N. Sumitomo, K. Noritake, T. Hattori, K. Morikawa, S. Niwa, K. Sato, *et al.*, "Experiment study on fracture fixation with low rigidity titanium alloy," *Journal of Materials Science: Materials in Medicine*, vol. 19, pp. 1581-1586, 2008/04/01 2008.
- [10] H. J. Rack and J. I. Qazi, "Titanium alloys for biomedical applications," *Materials Science and Engineering: C*, vol. 26, pp. 1269-1277, 2006.
- [11] M. Calin, A. Helth, J. J. Gutierrez Moreno, M. Bönisch, V. Brackmann, L. Giebeler, *et al.*, "Elastic softening of β -type Ti-Nb alloys by indium (In) additions," *Journal of the Mechanical Behavior of Biomedical Materials*, vol. 39, pp. 162-174, 2014.
- [12] J. A. Disegi, "Titanium alloys for fracture fixation implants," *Injury*, vol. 31, Supplement 4, pp. D14-D17, 2000.
- [13] M. Geetha, A. K. Singh, R. Asokamani, and A. K. Gogia, "Ti based biomaterials, the ultimate choice for orthopaedic implants – A review," *Progress in Materials Science*, vol. 54, pp. 397-425, 2009.
- [14] Y. F. Zheng, X. N. Gu, and F. Witte, "Biodegradable metals," *Materials Science and Engineering: R: Reports*, vol. 77, pp. 1-34, 3// 2014.
- [15] H. Hermawan, *Biodegradable Metals : From Concept to Applications*. Heidelberg, Germany: Springer, 2012.
- [16] H. Li, Y. Zheng, and L. Qin, "Progress of biodegradable metals," *Progress in Natural Science: Materials International*, 2014.
- [17] T. Barrows, "Degradable implant materials: A review of synthetic absorbable polymers and their applications," *Clinical Materials*, vol. 1, pp. 233-257, 1986.
- [18] R. Suuronen, T. Pohjonen, J. Vasenius, and S. Vainionpää, "Comparison of absorbable self-reinforced multilayer poly-L-lactide and metallic plates for the fixation of mandibular body osteotomies: An experimental study in sheep," *Journal of Oral and Maxillofacial Surgery*,

vol. 50, pp. 255-262, 1992.

[19] S. E. Henderson, K. Verdelis, S. Maiti, S. Pal, W. L. Chung, D.-T. Chou, *et al.*, "Magnesium alloys as a biomaterial for degradable craniofacial screws," *Acta Biomaterialia*, vol. 10, pp. 2323-2332, 2014.

[20] M. P. Staiger, A. M. Pietak, J. Huadmai, and G. Dias, "Magnesium and its alloys as orthopedic biomaterials: A review," *Biomaterials*, vol. 27, pp. 1728-1734, 2006.

[21] G. Mani, M. D. Feldman, D. Patel, and C. M. Agrawal, "Coronary stents: A materials perspective," *Biomaterials*, vol. 28, pp. 1689-1710, 2007.

[22] B. O'Brien and W. Carroll, "The evolution of cardiovascular stent materials and surfaces in response to clinical drivers: A review," *Acta Biomaterialia*, vol. 5, pp. 945-958, 2009.

[23] A. C. Hänzi, P. Gunde, M. Schinhammer, and P. J. Uggowitzer, "On the biodegradation performance of an Mg-Y-RE alloy with various surface conditions in simulated body fluid," *Acta Biomaterialia*, vol. 5, pp. 162-171, 2009.

[24] H. Hermawan, M. Moravej, D. Dubé, M. Fiset, and D. Mantovani, "Degradation behaviour of metallic biomaterials for degradable stents," in *Advanced Materials Research* vol. 15-17, ed, 2007, pp. 113-118.

[25] H. Hermawan, D. Dubé, and D. Mantovani, "Development of Degradable Fe-35Mn Alloy for Biomedical Application," *Advanced Materials Research*, vol. 15-17, pp. 107-112, 2007.

[26] H. Hermawan, H. Alamdari, D. Mantovani, and D. Dubé, "Iron-manganese: New class of metallic degradable biomaterials prepared by powder metallurgy," *Powder Metallurgy*, vol. 51, pp. 38-45, 2008.

[27] Y. Ren, J. Huang, K. Yang, B. Zhang, Z. Yao, and H. Wang, "Study of bio-corrosion of pure magnesium," *Jinshu Xuebao/Acta Metallurgica Sinica*, vol. 41, pp. 1228-1232, 2005.

- [28] G. Song and S. Song, "A possible biodegradable magnesium implant material," *Advanced Engineering Materials*, vol. 9, pp. 298-302, 2007.
- [29] H. Wang, Y. Estrin, and Z. Zúberová, "Bio-corrosion of a magnesium alloy with different processing histories," *Materials Letters*, vol. 62, pp. 2476-2479, 2008.
- [30] F. Witte, N. Hort, C. Vogt, S. Cohen, K. U. Kainer, R. Willumeit, *et al.*, "Degradable biomaterials based on magnesium corrosion," *Current Opinion in Solid State and Materials Science*, vol. 12, pp. 63-72, 2008.
- [31] J.-Y. Lee, G. Han, Y.-C. Kim, J.-Y. Byun, J.-i. Jang, H.-K. Seok, *et al.*, "Effects of impurities on the biodegradation behavior of pure magnesium," *Metals and Materials International*, vol. 15, pp. 955-961, 2009/12/01 2009.
- [32] N. Li and Y. Zheng, "Novel Magnesium Alloys Developed for Biomedical Application: A Review," *Journal of Materials Science & Technology*, vol. 29, pp. 489-502, 2013.
- [33] J. Gao, L. Qiao, Y. Wang, and R. Xin, "Research on bone inducement of magnesium in vivo," *Xiyou Jinshu Cailiao Yu Gongcheng/Rare Metal Materials and Engineering*, vol. 39, pp. 296-299, 2010.
- [34] J. Huang, Y. Ren, B. Zhang, and K. Yang, "Study on biocompatibility of magnesium and its alloys," *Xiyou Jinshu Cailiao Yu Gongcheng/Rare Metal Materials and Engineering*, vol. 36, pp. 1102-1105, 2007.
- [35] B. Mordike and P. Lukáč, "Physical Metallurgy," in *Magnesium Technology*, ed: Springer Berlin Heidelberg, 2006, pp. 63-107.
- [36] S. Housh and B. Mikucki, "Selection and Application of Magnesium and Magnesium Alloys," in *Properties and Selection: Nonferrous Alloys and Special-Purpose Materials*. vol. 2, ed: ASM

International, 1990, pp. 455 - 479.

[37] F. W. Bach, M. Schaper, and C. Jaschik, "Influence of lithium on hcp magnesium alloys," in *Materials Science Forum* vol. 419-422, ed, 2003, pp. 1037-1042.

[38] A. D. P. A.A. Nayeb-Hashemi, and J.B. Clark, "Mg (Magnesium) Binary Alloy Phase Diagrams," in *Alloy Phase Diagrams*. vol. 3, ed: ASM International, 1988.

[39] H. Hermawan, D. Dubé, and D. Mantovani, "Degradable metallic biomaterials: Design and development of Fe–Mn alloys for stents," *Journal of Biomedical Materials Research Part A*, vol. 93A, pp. 1-11, 2010.

[40] M. Schinhammer, A. C. Hänzi, J. F. Löffler, and P. J. Uggowitzer, "Design strategy for biodegradable Fe-based alloys for medical applications," *Acta Biomaterialia*, vol. 6, pp. 1705-1713, 2010.

[41] H. Hermawan, D. Dubé, and D. Mantovani, "Development of degradable Fe-35Mn alloy for biomedical application," in *Advanced Materials Research* vol. 15-17, ed, 2007, pp. 107-112.

[42] M. Peuster, C. Hesse, T. Schloo, C. Fink, P. Beerbaum, and C. von Schnakenburg, "Long-term biocompatibility of a corrodible peripheral iron stent in the porcine descending aorta," *Biomaterials*, vol. 27, pp. 4955-4962, 2006.

[43] P. P. Mueller, T. May, A. Perz, H. Hauser, and M. Peuster, "Control of smooth muscle cell proliferation by ferrous iron," *Biomaterials*, vol. 27, pp. 2193–2200, 2006.

[44] S. Zhu, N. Huang, L. Xu, Y. Zhang, H. Liu, H. Sun, *et al.*, "Biocompatibility of pure iron: In vitro assessment of degradation kinetics and cytotoxicity on endothelial cells," *Materials Science and Engineering: C*, vol. 29, pp. 1589-1592, 2009.

[45] M. Peuster, P. Wohlsein, M. Brüggmann, M. Ehlerding, K. Seidler, C. Fink, *et al.*, "A novel approach to temporary stenting:

degradable cardiovascular stents produced from corrodible metal—results 6–18 months after implantation into New Zealand white rabbits," *Heart*, vol. 86, pp. 563-569, November 1, 2001 2001.

[46] C. W. Siah, D. Trinder, and J. K. Olynyk, "Iron overload," *Clinica Chimica Acta*, vol. 358, pp. 24-36, 2005.

[47] R. O. N. Waksman, R. Pakala, R. Baffour, R. Seabron, D. Hellinga, and F. O. Tio, "Short-Term Effects of Biocorrosible Iron Stents in Porcine Coronary Arteries," *Journal of Interventional Cardiology*, vol. 21, pp. 15-20, 2008.

[48] T. Mitsunobu, Y. Koizumi, B.-S. Lee, K. Yamanaka, H. Matsumoto, Y. Li, *et al.*, "Role of strain-induced martensitic transformation on extrusion and intrusion formation during fatigue deformation of biomedical Co–Cr–Mo–N alloys," *Acta Materialia*, vol. 81, pp. 377-385, 2014.

[49] H. Hornberger, S. Virtanen, and A. R. Boccaccini, "Biomedical coatings on magnesium alloys – A review," *Acta Biomaterialia*, vol. 8, pp. 2442-2455, 2012.

[50] C. O. Hoog, N. Birbilis, M. X. Zhang, and Y. Estrin, "Surface Grain Size Effects on the Corrosion of Magnesium," *Key Engineering Materials*, vol. 384, pp. 229-240, 2008.

[51] R. Xin, M. Wang, J. Gao, P. Liu, and Q. Liu, "Effect of microstructure and texture on corrosion resistance of magnesium alloy," in *Materials Science Forum* vol. 610-613, ed, 2009, pp. 1160-1163.

[52] V. Kaesel, P. T. Tai, F. W. Bach, H. Haferkamp, F. Witte, and H. Windhagen, "Approach to Control the Corrosion of Magnesium by Alloying," in *Magnesium*, ed: Wiley-VCH Verlag GmbH & Co. KGaA, 2005, pp. 534-539.

[53] N. Hort, Y. Huang, D. Fechner, M. Störmer, C. Blawert, F. Witte, *et al.*, "Magnesium alloys as implant materials-Principles of property design for Mg-RE alloys," *Acta Biomaterialia*, vol. 6, pp. 1714-1725, 2010.

- [54] J. E. Gray and B. Luan, "Protective coatings on magnesium and its alloys - A critical review," *Journal of Alloys and Compounds*, vol. 336, pp. 88-113, 2002.
- [55] F. Witte, V. Kaese, H. Haferkamp, E. Switzer, A. Meyer-Lindenberg, C. J. Wirth, *et al.*, "In vivo corrosion of four magnesium alloys and the associated bone response," *Biomaterials*, vol. 26, pp. 3557-3563, 2005.
- [56] F. Witte, J. Fischer, J. Nellesen, H.-A. Crostack, V. Kaese, A. Pisch, *et al.*, "In vitro and in vivo corrosion measurements of magnesium alloys," *Biomaterials*, vol. 27, pp. 1013-1018, 2006.
- [57] Z. Li, X. Gu, S. Lou, and Y. Zheng, "The development of binary Mg-Ca alloys for use as biodegradable materials within bone," *Biomaterials*, vol. 29, pp. 1329-1344, 2008.
- [58] W. C. Kim, J. G. Kim, J. Y. Lee, and H. K. Seok, "Influence of Ca on the corrosion properties of magnesium for biomaterials," *Materials Letters*, vol. 62, pp. 4146-4148, 2008.
- [59] F. Witte, H. Ulrich, M. Rudert, and E. Willbold, "Biodegradable magnesium scaffolds: Part I: Appropriate inflammatory response," *Journal of Biomedical Materials Research - Part A*, vol. 81, pp. 748-756, 2007.
- [60] F. Witte, H. Ulrich, C. Palm, and E. Willbold, "Biodegradable magnesium scaffolds: Part II: Peri-implant bone remodeling," *Journal of Biomedical Materials Research - Part A*, vol. 81, pp. 757-765, 2007.
- [61] F. Witte, F. Feyerabend, P. Maier, J. Fischer, M. Störmer, C. Blawert, *et al.*, "Biodegradable magnesium-hydroxyapatite metal matrix composites," *Biomaterials*, vol. 28, pp. 2163-2174, 2007.
- [62] E. Zhang, W. He, H. Du, and K. Yang, "Microstructure, mechanical properties and corrosion properties of Mg-Zn-Y alloys with low Zn content," *Materials Science and Engineering A*, vol. 488, pp. 102-111, 2008.

- [63] G. Song, "Control of biodegradation of biocompatible magnesium alloys," *Corrosion Science*, vol. 49, pp. 1696-1701, 2007.
- [64] J. Lévesque, H. Hermawan, D. Dubé, and D. Mantovani, "Design of a pseudo-physiological test bench specific to the development of biodegradable metallic biomaterials," *Acta Biomaterialia*, vol. 4, pp. 284-295, 2008.
- [65] L. Xu, G. Yu, E. Zhang, F. Pan, and K. Yang, "In vivo corrosion behavior of Mg-Mn-Zn alloy for bone implant application," *Journal of Biomedical Materials Research - Part A*, vol. 83, pp. 703-711, 2007.
- [66] Y. Wan, G. Xiong, H. Luo, F. He, Y. Huang, and X. Zhou, "Preparation and characterization of a new biomedical magnesium-calcium alloy," *Materials and Design*, vol. 29, pp. 2034-2037, 2008.
- [67] L. L. Rokhlin, *Magnesium Alloys Containing Rare Earth Metals: Structure and Properties*. Taylor & Francis, London: CRC Press, 2003.
- [68] X. Zhang, G. Yuan, L. Mao, J. Niu, and W. Ding, "Biocorrosion properties of as-extruded Mg-Nd-Zn-Zr alloy compared with commercial AZ31 and WE43 alloys," *Materials Letters*, vol. 66, pp. 209-211, 2012.
- [69] Z. Li, X. Gu, S. Lou, and Y. Zheng, "The development of binary Mg-Ca alloys for use as biodegradable materials within bone," *Biomaterials*, vol. 29, pp. 1329-1344, 2008.
- [70] L. Xu, G. Yu, E. Zhang, F. Pan, and K. Yang, "In vivo corrosion behavior of Mg-Mn-Zn alloy for bone implant application," *Journal of Biomedical Materials Research Part A*, vol. 83A, pp. 703-711, 2007.
- [71] T. Kraus, F. Moszner, S. Fischerauer, M. Fiedler, E. Martinelli, J. Eichler, *et al.*, "Biodegradable Fe-based alloys for use in osteosynthesis: Outcome of an in vivo study after 52 weeks," *Acta Biomaterialia*, vol. 10, pp. 3346-3353, 2014.

- [72] M. Moravej, A. Purnama, M. Fiset, J. Couet, and D. Mantovani, "Electroformed pure iron as a new biomaterial for degradable stents: In vitro degradation and preliminary cell viability studies," *Acta Biomaterialia*, vol. 6, pp. 1843-1851, 2010.
- [73] B. L. Vallee, "Zinc: Biochemistry, physiology, toxicology and clinical pathology," *BioFactors*, vol. 1, pp. 31-36, 1988.
- [74] H. J. Zhang, D. F. Zhang, C. H. Ma, and S. F. Guo, "Improving mechanical properties and corrosion resistance of Mg₆₀Zn₄₀ magnesium alloy by rapid solidification," *Materials Letters*, vol. 92, pp. 45-48, 2013.
- [75] I. Bhamji, M. Preuss, P. L. Threadgill, R. J. Moat, A. C. Addison, and M. J. Peel, "Linear friction welding of AISI 316L stainless steel," *Materials Science and Engineering: A*, vol. 528, pp. 680-690, 2010.
- [76] A. K. Nasution, N. S. Murni, N. B. Sing, M. H. Idris, and H. Hermawan, "Partially degradable friction-welded pure iron–stainless steel 316L bone pin," *Journal of Biomedical Materials Research Part B: Applied Biomaterials*, pp. n/a-n/a, 2014.
- [77] H. K. Rafi, G. D. J. Ram, G. Phanikumar, and K. P. Rao, "Microstructure and tensile properties of friction welded aluminum alloy AA7075-T6," *Materials & Design*, vol. 31, pp. 2375-2380, 2010.
- [78] R. K. Franklin, "Dissertation: In vivo Electrochemical Sensors," Electrical Engineering, The University of Michigan., Michigan, US, 2010.
- [79] T. Kraus, F. Moszner, S. Fischerauer, M. Fiedler, E. Martinelli, J. Eichler, *et al.*, "Biodegradable Fe-based alloys for use in osteosynthesis: Outcome of an in vivo study after 52 weeks," *Acta Biomaterialia*, vol. 10, pp. 3346-3353, 2014.
- [80] D.-T. Chou, D. Hong, P. Saha, J. Ferrero, B. Lee, Z. Tan, *et al.*, "In vitro and in vivo corrosion, cytocompatibility and mechanical properties of biodegradable Mg–Y–Ca–Zr alloys as implant materials,"

Acta Biomaterialia, vol. 9, pp. 8518-8533, 11// 2013.

[81] J. W. Seong and W. J. Kim, "Development of biodegradable Mg–Ca alloy sheets with enhanced strength and corrosion properties through the refinement and uniform dispersion of the Mg₂Ca phase by high-ratio differential speed rolling," *Acta Biomaterialia*, vol. 11, pp. 531-542, 1/1/ 2015.

[82] X. B. Chen, D. R. Nisbet, R. W. Li, P. N. Smith, T. B. Abbott, M. A. Easton, *et al.*, "Controlling initial biodegradation of magnesium by a biocompatible strontium phosphate conversion coating," *Acta Biomaterialia*, vol. 10, pp. 1463-1474, 3// 2014.

[83] T. Huang, J. Cheng, D. Bian, and Y. Zheng, "Fe–Au and Fe–Ag composites as candidates for biodegradable stent materials," *Journal of Biomedical Materials Research Part B: Applied Biomaterials*, pp. n/a-n/a, 2015.

[84] A. Alabbasi, S. Liyanaarachchi, and M. B. Kannan, "Polylactic acid coating on a biodegradable magnesium alloy: An in vitro degradation study by electrochemical impedance spectroscopy," *Thin Solid Films*, vol. 520, pp. 6841-6844, 9/30/ 2012.

[85] A. Zomorodian, M. P. Garcia, T. Moura e Silva, J. C. S. Fernandes, M. H. Fernandes, and M. F. Montemor, "Corrosion resistance of a composite polymeric coating applied on biodegradable AZ31 magnesium alloy," *Acta Biomaterialia*, vol. 9, pp. 8660-8670, 11// 2013.

CHAPTER 5

CHARACTERIZATION OF NITROGEN AND MAGNESIUM-DOPED WITH TITANIUM DIOXIDE AT DIFFERENT CALCINATION TEMPERATURE USING X-RAY DIFFRACTION (XRD)

Nur' Aliaa Razali and Siti Amira Othman

Department of Physics and Chemistry,
Faculty of Applied Sciences and Technology,
Universiti Tun Hussein Onn Malaysia, Pagoh Campus, KM 1, Jalan
Panchor, 84600 Panchor, Johor.

5.0 INTRODUCTION

In photocatalysis, titanium dioxide is often used as the catalyst due to the cheap raw materials, easy to obtain and also environmental friendly. There is no side product that will harm the environment discharged from the process as semiconductor catalysts such as TiO_2 and ZnO have been widely used to mineralize harmful organic pollutants in wastewater into harmless inorganic nontoxic compounds such as CO_2 , HCl and water, thus it is very recommended to be applied in the wastewater treatment process [1]. Titanium dioxide is made up of TiO_6 octahedral. This arrangement of octahedral make the structure consists of three different of polymorphs which are anatase, rutile and brookite [2]. Basically, the rutile part is thermodynamically stable, while anatase and brookite categorized as metastable.

Despite of all the advantages of this photocatalyst, titanium dioxide is capable to act as sensitizer for light which will reduce the redox process due to their electronic structure. The best part is that the titanium dioxide can be chemically activated by light, thus in the industry, water treatment, air-cleaning or self-cleaning for the building often used titanium dioxide which helps the cleaning process become easier.

However, titanium dioxide only can be applied when the Ultra Violet (UV) light is presence in order to activate the electrons because of the high band gap energy (3.2 eV), which will cause the process become very costly [3]. In that case, the band gap energy need to be narrowed in order to enable the process operate under the visible light ($400 < \lambda < 500$) by modifying the photocatalyst. One of the easiest ways to reduce the band gap energy is by using dopants with suitable elements. There are others ways including sputtering, ion implantation, pulser laser deposition, hydrothermal and solvothermal synthesis but sol-gel method will be chosen as the method is easy to apply than the others as the process only need to operate at low temperature normally less than 700°C and low cost involved [3].

A non-metal dopant, as an example, nitrogen is considered as the most effective dopant to be incorporated with TiO_2 as the size is smaller and the source is cheaper. Besides, many research showed a great result when nitrogen doped TiO_2 is used on methylene blue and methyl orange. Thus, in this study, nitrogen doped TiO_2 will be applied on Reactive Black 5 dye and the result will be analyzed [4]. Some researchers believed that the nitrogen atoms substitute the oxygen atom in the lattice of TiO_2 molecule [2]. Magnesium is one of the abundant alkaline earth metal and less hazardous to be used in the water treatment process which will cause a more environmental friendly process. Magnesium is a type of metal dopant and a study of doping with magnesium ion that have nearly equivalent atomic radius to titanium, may give a better insight into doping process in detail and the effect of dopant size on the photocatalytic activity [5]. Besides, by inserting metal ions into TiO_2 structure can decrease the band gap and from the research, it is found that metals are able to lower the electron-hole recombination rate and trap the electrons [6].

5.1 METHODOLOGY

5.1.1 Chemicals

In this research, several chemicals were used and bought from Sigma-Aldrich. Titanium (IV) isopropoxide (TTIP) 97% bought from Sigma-Aldrich was used as the precursor in the process of photocatalyst preparation. Magnesium chloride 6 hydrate from Bendosen and ammonium nitrate 99 % from Emory. Ethanol, 95 %, a laboratory grade from HmbG chemical was used as solvent. Acetic acid glacial, 100 %, AR from Emory was used. Reactive Black 5 with dye content ≥ 50 % was bought from Sigma-Aldrich for the photodegradation application.

5.1.2 Preparation of Photocatalyst

Initially 45 ml of deionized water and 5 ml of acetic acid were mixed together and labelled as solution A. Solution B was prepared in another beaker by diluting 15 ml of TTIP with 5 ml of ethanol. Solution B was added dropwise into solution A for 30 minutes, and then the solution was stirred vigorously within 3 hours in the room temperature. Different amount of magnesium chloride and nitrogen nitrate was added into solution B in order to vary the weight percentage of magnesium and nitrogen as the dopants. Next, the solution was centrifuged for 15 minutes at 9000 rpm and the liquid layer was removed and sol gel was obtained.

The sol gel was left in room temperature for 12 hours as pre-aging process before aging in the oven at temperature of 110°C for 17 hours to remove excess solvents. The powder obtained was grounded finely using mortar pestle, and calcinated in a box furnace at 300°C, 500°C and 700°C for 1 hour for heating treatment in order to complete the preparation of photocatalyst. Then all the samples were analyzed using XRD, FESEM and undergo photocatalytic degradation. Dye samples were taken at every 15 minutes interval time. All the dye samples that undergo photodegradation were analyzed by using UV-Vis spectrophotometer. All the samples are labelled as 0.5 wt. % Mg-TiO₂, 0.7 wt.% Mg-TiO₂, 0.9 wt. % Mg-TiO₂, 0.5 wt. % N-TiO₂, 0.70 wt. % N-TiO₂ and 0.9 wt.% N-TiO₂.

5.1.3 Sample Characterization

All the samples were characterized and analyzed in order to identify the phase structure using X-ray Diffraction (XRD). All the results and data were recorded and tabulated.

5.2 RESULT AND DISCUSSION

The phase composite and estimation of crystallite size for all samples were analyzed and evaluated by using X-ray diffraction analysis.

After the XRD analysis done, the results will be analyzed and the estimated crystallite size of all samples (0.5wt.% N-TiO₂, 0.7wt.% N-TiO₂, 0.9wt.% N-TiO₂, 0.5wt.% Mg-TiO₂, 0.7wt.% Mg-TiO₂ and 0.9wt.% Mg-TiO₂) at different calcination temperature of 300°C, 500°C and 700°C calculated by using the Scherer's equation as follows:

$$D = K\lambda/\beta\cos\theta \quad (5.1)$$

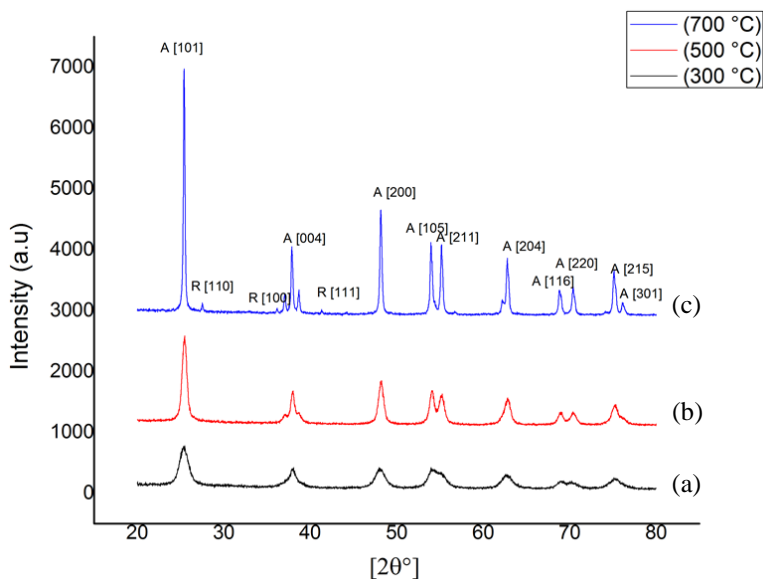
Where, $K=0.9$ is the Scherer constant, $\lambda=0.15406$ nm is the X-ray wavelength, β is the peak width of half maximum in radian, and θ is the Bragg diffraction angle. The rutile and anatase phase content (%) can be calculated by using the equation;

$$\% \text{ Rutile phase} = \frac{1}{[(I_A/I_R)^{0.884+1}] \quad (5.2)$$

$$\% \text{ Anatase phase} = \frac{1}{[(I_R/I_A)^{1.26+1}] \quad (5.3)$$

Table 5.1: The particle size of samples at different calcination temperature

Sample name	(wt.%)	Calcination Temperature (°C)	Anatase phase content (%)	Rutile phase content (%)	Estimated Anatase crystallite size (nm)	Estimated Rutile crystallite size (nm)
N-TiO ₂	0.5	300	100	-	7.57	-
		500	100	-	12.80	-
		700	75	25	55.56	118.57
Mg-TiO ₂	0.5	300	100	-	7.56	-
		500	100	-	13.94	-
		700	96	4	41.67	89.01

**Figure 5.1:** Comparison XRD analysis of sample 0.5wt. % Mg-TiO₂, prepared at (a) 300 °C (b) 500 °C and (c) 700°C.

Calcination temperature can affect the physical properties of the gels by polymerization, coarsening and phase transformation [7]. Figure 5.1 showed the XRD analysis of sample 0.5wt. % Mg-TiO₂, prepared at varying temperatures from 300°C to 700°C. From the analysis, it can be seen that at temperature 300 °C and 500 °C, only single anatase phase occurred and at 700 °C, the peaks of rutile can be observed. A study conducted by Kumar et al, (2016), found that at lower temperature (300 °C -500 °C) only anatase phase was observed and at 600 °C the rutile peaks started to appear. Peaks at calcination temperature of 300°C showed wider than the peaks at temperature of 500°C and 700 °C. The anatase phase can be observed at peaks of $2\theta = 24.40^\circ, 38.00^\circ, 48.00^\circ, 54.00^\circ, 62.90^\circ, 69.00^\circ, \text{ and } 75.14^\circ$. As the calcination temperature was increased up to 500°C, the peaks of anatase phase become defined and can be observed clearly especially at $2\theta = 54^\circ$ and 55.12° , also at $2\theta = 68.9^\circ$ and 70.4° . The peaks of rutile phase can be observed at $2\theta = 27.45^\circ, 36.09^\circ, 41.23^\circ, 54.32^\circ, 56.64^\circ, 62.74^\circ, 64.04^\circ, 69.01^\circ$ and 69.79° . From the analysis, it also can be seen that the peaks at 700°C become narrower compare to peaks at 300°C and 500 °C. This is because of the improvement of TiO₂ crystallinity associated with the anatase crystals growth [9]. According to Mozia, (2008), during the heat treatment of TiO₂, the dehydration takes place and as a result the crystals grow to a size larger than those of the original particles. Besides, the increase of the heat treatment temperature up to 700°C led to the phase transformation from thermodynamically metastable anatase to the most stable form of TiO₂, rutile. The estimated crystallites sizes can be calculated by using the Scherer's equation (Eq. 5.1) and the percentage of anatase and rutile phase can be found by applying Equation 5.2 and 5.3. From table 1, the estimated crystallites size for sample 0.5 wt.% Mg-TiO₂ at 300 °C have smallest size compared to 500 °C and 700 °C which are 7.56 nm, 13. 94 nm, 41.67 nm (anatase) and 89.01 nm (rutile) respectively. The size of crystallites increases as the calcination increases which is coincide with statement made by Mozia, (2008) and Aphairaj *et al*, (2011). At heat treatment of 700 °C, the samples contain 96 % of anatase and 4 % of rutile.

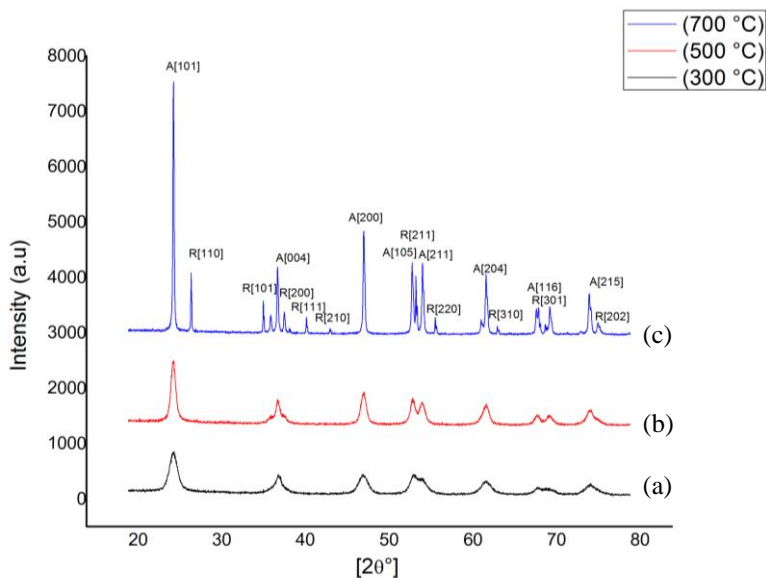


Figure 5.2: Comparison XRD analysis of sample 0.5wt. % N-TiO₂, prepared at varying temperatures of (a) 300°C (b) 500°C and (c) 700°C

Based on Figure 5.2, different phase of photocatalyst can be seen on the XRD data of photocatalyst sample with 0.5wt. % N-TiO₂ where each of them were calcined at temperature of 300°C, 500°C and 700°C respectively. From the graph, it can be seen at calcination temperature of 300°C and 500°C, anatase phase were observed and at 700°C rutile phase can be observed from the graph. At 300°C, the anatase phase can be seen and at 500°C, defined peaks of anatase can be clearly observed at $2\theta = 25.40, 38.00, 48.00, 54.00, 55.20, 62.72, 68.80, 70.26$ and 75.14° . As the higher of calcination temperature were applied, the rutile peaks already formed at 700°C, where the peaks can be observed at $2\theta = 27.58, 36.22, 41.38, 54.46, 64.16,$ and 69.92° . Thus, it can be said the formation of rutile may start at 600 °C. From the XRD graph, at lower temperature, broad peaks can be seen at $2\theta = 48.00, 54.00, 55.20, 62.72, 68.8, 70.26$ and 75.14° which indicating small crystallite sizes. As the

calcination temperature getting higher, the peaks become narrowed and stronger intensities could be observed, which means that the crystallite sizes have grown due to the heat treatment applied and the crystallinity have been improved as the calcination temperature increased. The estimated crystallite sizes were calculated and tabulated as in table 5.1. At 300 °C, the estimated crystallite size is 7.57 nm, at 500 °C, 12.8 nm and at 700 °C, the estimated crystallite sizes are 55.56 nm (anatase) and 118.57 nm (rutile). The anatase-rutile phase content for this sample were calculated and it was found that 75 % of anatase and 25 % rutile present in the sample.

5.3 CONCLUSION

XRD analysis has confirmed the photocatalyst that undergo calcination temperature of 300°C and 500 °C to be anatase structure. Rutile phase has been observed from the XRD analysis for the photocatalyst that calcinated at 700°C. The rutile peaks were predicted started to form at temperature of 600 °C. Photocatalyst that undergo calcination temperature at 500°C showed anatase structure, but the catalyst particle produced were found larger in size compared to catalyst prepared at 300 °C, which will resulted in smaller surface area.

REFERENCES

- [1] Mondal, K. & Sharma, A. (2005). *Photocatalytic Oxidation of Pollutant Dyes in Wastewater by TiO₂ and ZnO nano-materials- A Mini Review*.
- [2] Nolan, N. T., Synnott, D. W., Seery, M. K., Hinder, S. J., Wasenhoven, A. V. & Pillai, S. C. (2011). *Effect of N-doping on the photocatalytic activity of sol-gel TiO₂*. *Journal of Hazardous Materials*, 88-94.
- [3] Sikirman, A., Krishnan, J. m Jai, J. & Senusi, F. (2014). *Preparation, Characterization and Effectivity of N, Fe-TiO₂ as a Visible Light Active Photocatalyst*. *Advanced Materials*
- [4] Segne, T. A., Tirukkavalluri, S. V. & Challapalli, S. (2011). *Studies on Characterization and Photocatalytic Activities of Visible*

Light Sensitive TiO₂ Nano Catalysts Co-doped with Magnesium and Copper. International Research Journal of Pure & Applied Chemistry 1(3), 84-103.

[5] Avasalara, B. K., Tirukkovallun, R. & Bojja, S. (2016). *Magnesium Doped Titania for Photocatalytic Degradation of Dyes in Visible Light.* Journal of Environmental & Analytical Toxicology.

[6] Behnajady, M. A. & Tohidi, Y. (2013). *The effect of operational parameters in the photocatalytic activity of synthesized Mg/ZnO–SnO₂ nanoparticles.* Desalination and Water Treatment, 1-7.

[7] Hsiang, H. I. & Lin, S. C. (2007). *Effects of aging on nanocrystalline anatase-to- rutile phase transformation kinetics.* Ceramics International 34, 557– 561.

[8] Kumar, M., Gupta, A. K., & Kumar, D. (2016). *Annealing temperature Effects on Structural and Hydrophilic Properties of Magnesium-Doped TiO₂ Thin Films.* Journal of ceramic science and technology, 463-468.

[9] Mozia, S. (2008). *Effect of calcination temperature on photocatalytic activity of TiO₂ Photodecomposition of mono- and polyazo dyes in water.* Polish journal of chemical technology, 42 — 49.

[10] Aphairaj, D., Wirunmongkol, T., Chaloeay-arb, P., Pavasupree, S. & Limsuwan, P. (2011). *Effect of calcination temperatures on structures of TiO₂ powders prepared by hydrothermal method using Thai leucoxene mineral.* 9th Eco-Energy and Materials Science and Engineering Symposium, 1-4.

CHAPTER 6

ON THE MECHANICAL BEHAVIOUR OF HYPERELASTIC FUNCTIONALLY GRADED POLYMER

Ahmad Wisnu Sulaiman¹, Mohd Ayub Sulong^{1,2}

¹Department of Applied Mechanics and Design, Faculty of Mechanical Engineering, Universiti Teknologi Malaysia, 81310 Johor, Malaysia

²Medical Devices and Technology Centre (MEDITEC), Faculty of Biosciences and Medical Engineering, Universiti Teknologi Malaysia, 81310 UTM Johor Bahru, Johor, Malaysia

6.0 INTRODUCTION

A linear elastic material is a material that linearly deforms as stress increases. It will return to its original shape when stress is removed as long as it does not reach yield point. The application of linear elastic material is often used to bear a load where it requires to hold it without permanent deformation. In some application of material the condition requires a material that can withstand large deformation while still in elastic mode deformation. The material that can undergo large deformation under low stress is hyperelastic.

6.1 HYPERELASTIC MATERIAL MODEL

Hyperelastic has different responses on different types of loading. The response of uniaxial tensile, biaxial, and planar shear are not similar. Several models have been developed to mimic the actual data. Elastomeric material models are characterized by different forms of their strain energy density functions. Such material is also called hyperelastic. Implicit in the use of these functions (usually denoted by W) is the assumption that the material is isotropic and elastic[1].

The principal of Neohookean model is derived from thermodynamic and statistical mechanics. It is also called first order approximation. The equation for Neohookean model is shown in equation 2.1.

$$W = \frac{1}{2}G(\lambda_1^2 + \lambda_2^2 + \lambda_3^2 - 3)$$

W = Strain energy density
 G = Bulk modulus
 l = Stretch ratio

The strain energy density function is introduced by Treolar in 1944 to confirm experiments on rubberlike material. The model is famous until now because of its similarity with Hooke's law which stress is proportional with strain

6.1.1 MOONEY

The basic assumption on Mooney equation is the material is incompressible where one of the stress invariants is equals to 1 so that the strain energy function will become the function of two invariants

$$W = C_1(I_1 - 3) + C_2(I_2 - 3)$$

$$I_1 = \lambda_1^2 + \lambda_2^2 + \lambda_3^2$$

$$I_1 = \lambda_1^2\lambda_2^2 + \lambda_1^2\lambda_3^2 + \lambda_2^2\lambda_3^2$$

$$I_3 = \lambda_1^2\lambda_2^2\lambda_3^2 = 1$$

W = Strain energy density
 C = Mooney constant
 I = Stress Invariants

There are some other model that was proposed based on Mooney model. Which are Signiorni and Yeoh[2]. The equation is shown in equation 2.6 and 2.7 respectively.

$$W = C_{10}(I_1 - 3) + C_{01}(I_2 - 3) + C_{20}(I_1 - 3)^2$$

$$W = C_{10}(I_1 - 3) + C_{20}(I_1 - 3) + C_{30}(I_1 - 3)^2$$

The differentiation between Signiorni and Yeoh lies on the stretch invariants. Signiorni use two stretch invariants (I_1 and I_2), while Yeoh use one stretch invariant (I_1). The rest of the equation is similar. However, these models are not used in this study.

6.1.2 OGDEN

Ogden model is capable to tolerance compressibility in the material. Ogden model is based on Treolar's experiment data and formulated back in 1972[3]. The model is valid for both incompressible and compressible material. Its equation is based on series. The equation for the model is shown in equation below.

$$W = \sum_{n=1}^N \frac{\mu_n}{\alpha_n} \left[J^{\frac{-\alpha_n}{3}} (\lambda_1^{\alpha_n} + \lambda_2^{\alpha_n} + \lambda_3^{\alpha_n}) \right] + 4.5K \left(J^{\frac{1}{3}} - 1 \right)^2$$

W	= Strain energy density
K	= Initial bulk modulus
l	= Stretch ratio
μ_n	= material constant
α_n	= material constant
J	= Volumetric Ratio

Kut et. al in 2017 develop a simulation test on each available elastomer model to confirm which model is best to fit the cyclic uniaxial tension test. The simulation was done using MSc Marc software. The loading configuration was set using 3 point bending test and uniaxial tensile test with cylinder model tested. The result shown the Yeoh model is the best elastomer model in the study with 62 % deformation[4].

Moerman et.al in 2015 tested Ogden model tension compression asymmetry properties. The tension-compression asymmetry is a condition where a material response between tension and compression response are not symmetrical. For human body soft tissue symmetric tension-compression is recommended. In the case of anisotropic material controlling the degree of asymmetry is recommended [5].

Kaden in 2007 investigates reinforced hyperelastic materials with ABAQUS software. The material used is rubber and fiber glass. The investigation was tested on cylindrical fiber at the center to verify the effect of configuration and fiber size ratio to the strength of material on regular arrays and random arrays.

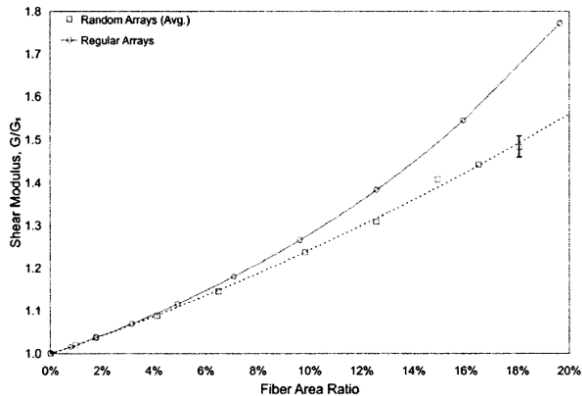


Figure 6.1 : Shear modulus on regular and random arrays [6]

Figure 6.1 shows the effect of fiber area ratio with shear modulus. Squared line represents random arrays, while the other one is random arrays. The increase of fiber ratio will improve the shear modulus regardless configuration of arrays. The random arrays shows linear relation between fiber ratio and shear modulus, as fiber ratio increases the shear modulus increased. The regular array is more superior then random arrays in terms of shear modulus improvement. The relation between fiber ratio and shear modulus in regular arrays is exponential.

Kuksenko et.al in 2018 investigates the large deformation response of composites reinforced by continuous wavy fibers using three-dimensional FEA. The focus is placed on in-phase fibers with circular cross-sections following sinusoidal paths. The result show the fibers' relative radius has no effect on the overall mechanical response of the considered composite. At higher values of the contrast, a minor difference between the responses of composites reinforced by fibers of different relative radii is observed under longitudinal elongation and shear in the x_1-x_2 plane[7]

Mihai et.al in 2015 developed FEA model to investigate soft tissue of human brain. In the study it found that the fung and gent model that are commonly used to model soft tissue is insufficient same condition found in the Neohookean and Mooney model. The study found Ogden elastomer model is the sufficient one for soft tissue[8].

Brevlasky et.al in 2016 investigates static and dynamic behavior of hyperelastic material with tube cylindrical geometry. The cylinder is described by hyperelastic material with classic Neohookean and Mooney model applied. The analysis is targeting the response of model to mimic blood vessel. The pressure load applied are the dead load with radial distributed load and actual pressure as a follower load that depends on the area and always normal to the deformed surface. The static responses of the shell under these two loads differ essentially at moderate strains, while the behavior is similar for small loads. The principal difference is that the axial displacements are much larger for the shell under distributed radial forces, while for actual pressure the shell is stretched both in circum-ferential and axial directions [9].

Kokinis et.al in 2017 investigates the effect of gradient in FGM. The simulation was done in COMSOL FEA software and confirmed by experimental mechanical test. There are three different configurations tested in the study, which are ascending gradient (high tensile strength from middle and getting lower tensile strength towards edges), descending, and softlayer. The coupon is tested with uniaxial stretch in x axis direction. The strain energy contour from FEA simulation result for each configuration are shown in Figure 6.2.

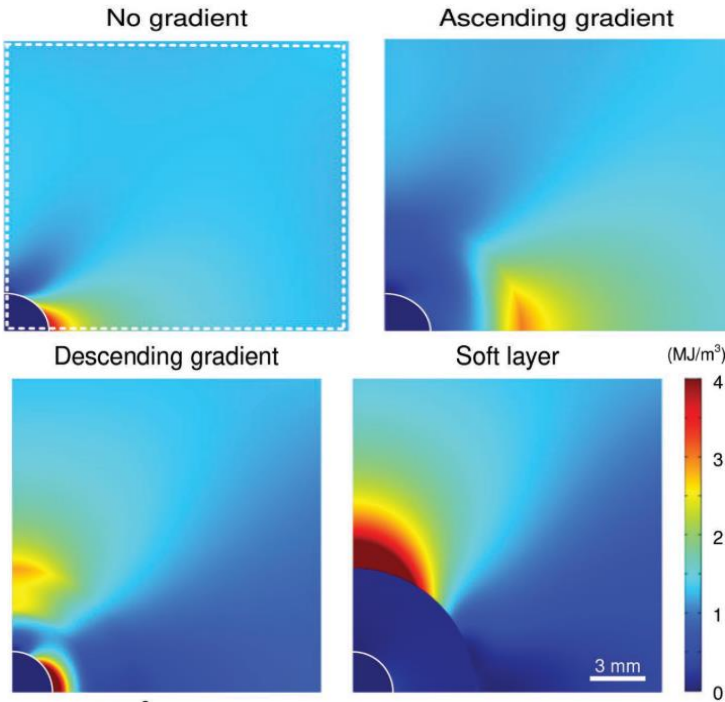


Figure 6.2: Strain Energy Density [10]

Figure 6.2 shows SED contour for all configuration. The contour with soft layer has concentration at the top of the material join without strain energy concentration along the direction of stretch. Descending gradient has two area of concentration which are along the stretch direction and also at the top. Both ascending and no gradient have

concentration area only along the stretch direction.

6.2 METHODOLOGY

The base geometry used are rectangular solid with 20 mm width, 70 mm height, and 5mm thickness for all models.

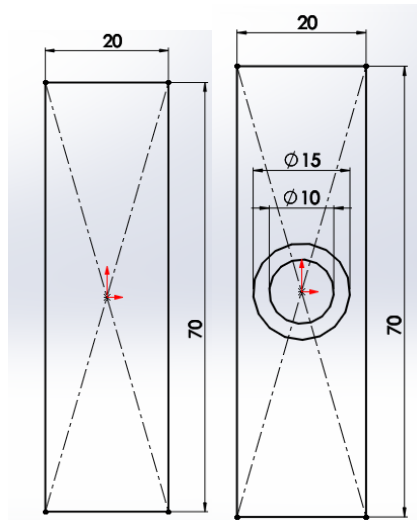


Figure 6.2: Geometry Used (a. horizontal and vertical, b. cylindrical)

Figure 6.3 shows geometries used in simulation which are cylindrical center, horizontal rectangular, and vertical. The models are modeled in FEMAP. The solid needs to be subdivided into several solid to improve the meshing quality by reducing the mesh distortion and aspect ratio, especially for the cylindrical center geometry since the junction of cylinder at the center with rectangular at the outer bond will make hexagonal element will become distorted. This step is expected to improve calculation time and accuracy.

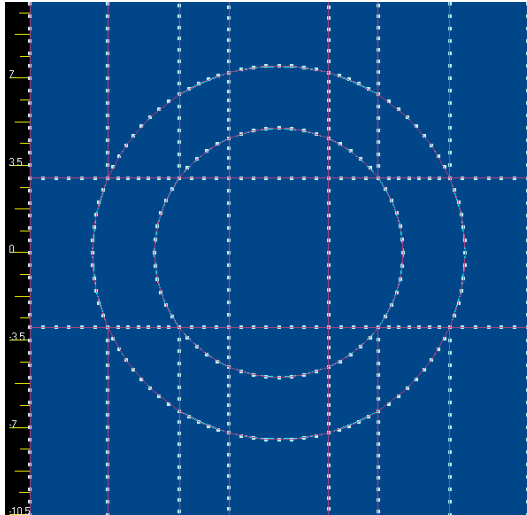


Figure 6.3: Solid Subdivision

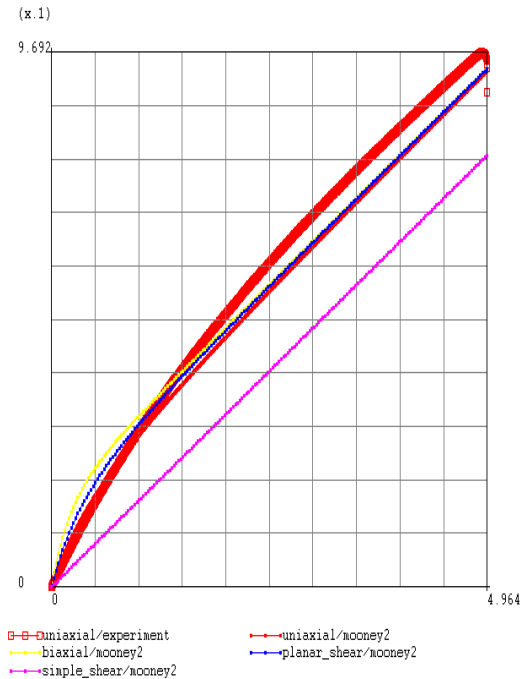
Figure 6.4 shows the solid subdivision in FEMAP for a coupon that has a cylindrical geometry introduced at the center of the solid. Subdivision of the solid is indicated by dotted lines. The geometry then mesh using hexmesh option in FEMAP and after it finish the model is exported into MSc Marc. The material data used is shown in Table 6.1.

Table 6.1: Uniaxial Tensile Data

Material	Tensile Stregth (MPa)	Fracture Strain
Lowest TS	0.969246746	4.964425155
Medium TS	1.091886708	4.219960316
Highest TS	1.681066783	9.689547491

Table 6.1 shows the data of material used in this study. The fracture strain for each individual data shows different value, highest TS material data are having the longest final elongation at fracture with 9.69 strain and TS of 1.67 MPa. Medium TS and Lowest TS are having 4.22 and 4.96 fracture strain, with 1.09, and 0.97 MPa TS respectively.

The experimental data needs to be fitted with elastomer model. The fitting is done in Msc Marc software. The method used is to fit the experimental data using the available model in elastomer of Msc Marc. The lowest number of order from the model with the best fit is selected and applied to the specific material. The elastomer model used for each material is shown in figure 6.5.



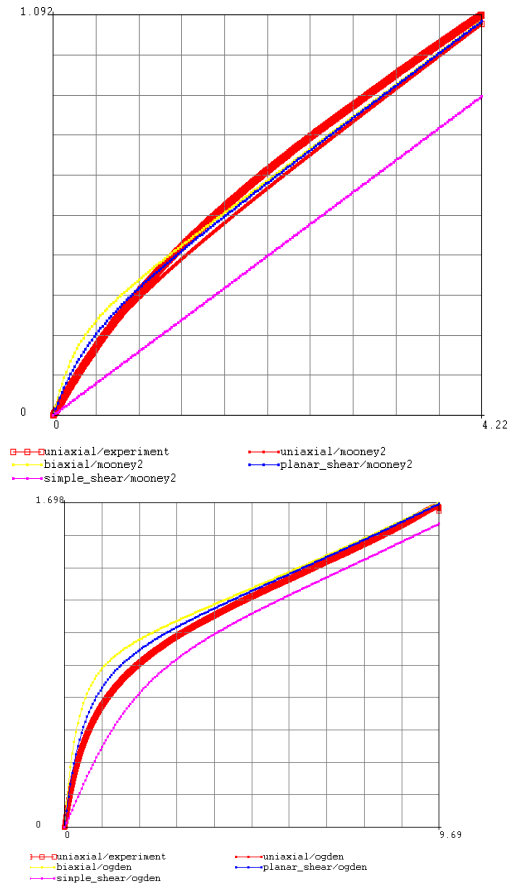


Figure 6.5: Materials Stress Strain Used (a. Lowest TS, b. Medium TS, c. Highest TS)

Figure 6.5 shows the experimental and calculated stress strain curve of lowest TS, medium TS, and highest TS. The lowest TS material with 9.962 MPa and 4.96 strain is modeled with Mooney 2 terms with positive coefficient, the medium TS with 1.092 MPa and 4.22 strain is also modeled with Mooney 2 terms, while the highest TS with 1.698 MPa and strain 9.69 is modeled with Ogden 2 terms. The calculated coefficient

and bulk modulus for Mooney model is shown in Table 6.2.

Table 6.2: Lowest TS and Medium TS Mooney Coefficient and Bulk Modulus

Material	Model	C1	C 2	Bulk Modulus
Lowest TS	Mooney	0.779	0	2521.11
Medium TS		0.103	0	974.296

Table 6.2 shows the coefficient and bulk modulus used for lowest TS and medium TS material. Lowest TS Mooney coefficient is 0.779 with bulk modulus of 2521.11. While medium TS Mooney coefficient is 0.103 with bulk modulus of 974.296. For both material positive coefficient is applied. Thus, the coefficient 2 is 0. Ogden coefficient and modulus of highest TS material is shown in Table 6.3. The solver used for simulation is *paradiso direct sparse*.

Table 6.3: Highest TS Ogden Coefficient and Bulk Modulus

Highest TS	No. of Terms	Moduli	Exp	Bulk Modulus
Ogden	1	0.0102	2.634	2361.76
	2	0.782	1.171	

6.3 RESULT AND DISCUSSION

Before the simulation started, the mesh quality should be confirmed using convergence study. The convergence study is carried out using simple block geometry. The purpose is to ensure the mesh quality is sufficient to be used in simulation. The size of mesh element simulated is start with 0.7 mm, 0.5 mm, and the last is 0.4 mm. The result to be analyzed is stress strain curve of each element size result.

The result of stress strain curves for each element size is then compared with experimental data. The convergence study graph is shown in Figure 6.6.

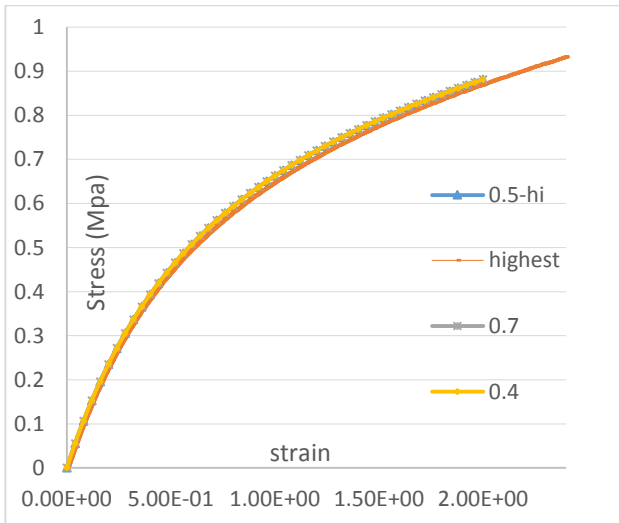


Figure 4.6: Convergence Study

Figure 6.6 shows stress strain curves of all element and experimental data. Blue line represents 0.5 mm element size, red line represents experimental data, grey line represents 0.7 mm element size, and orange line represents 0.4 element size. All of the simulated data shows a good agreement with experimental data. There is only small difference between the simulated and experimental data, stated from 0.4 strain. However, the gap is small and it still follows the experimental data curvature. There is no significant difference between 0.4 mm, 0.5 mm,

and 0.7 mm element size curves, by considering the time effectiveness for simulation the option is now between 0.5mm and 0.7 mm because the simulation time for 0.4 mm will take almost two days to finish. The simulation displacement is two times its original shape. The final mesh deformation is expected to be highly deformed, by considering this factor to safely and efficiently run the simulation 0.5 mm element size is chosen.

6.3.1 FORCE-DISPLACEMENT CURVE

The Force displacement curve from each configuration is shown in Figure 6.7.

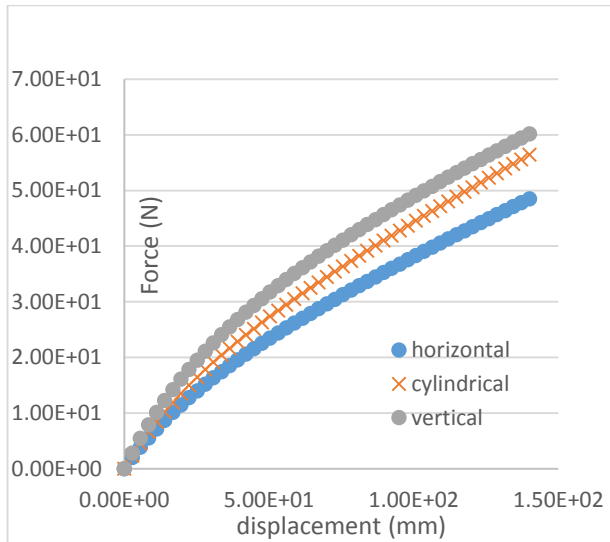


Figure 6.7: Force Displacement Curve

Figure 6.7 shows force displacement of all configuration. Blue dots represent horizontal, x marks represent cylindrical, and grey dots represent vertical configuration data. The data from all configuration shows different behavior. It has its own modulus in all displacement value. Horizontal configuration has the lowest force at final displacement. It has 48.5 N at its final displacement which is 140 mm. The cylindrical configuration has the medium force at final displacement compare to all configuration. It has 36.4 N at the final displacement. The

vertical configuration has the highest force at the final displacement. It has 60.2 N at the final displacement.

The behavior of all configuration is nonlinear. The horizontal configuration starts to have lower force displacement ratio at early stage. It began to lose the ratio at 11.5 mm displacement. After that point the ratio is nearly unchanged. The cylindrical configuration has different behavior at 20.4 mm displacement. However, there is no significant changes. The vertical configuration has smooth curve almost without transition. It could indicate that the force is spread along the similar area for whole time of the test.

6.3.2 STRESS-STRAIN CURVE

Stress strain curve of the simulation is calculated based on the force displacement. The stress strain curve is shown in Figure 6.8.

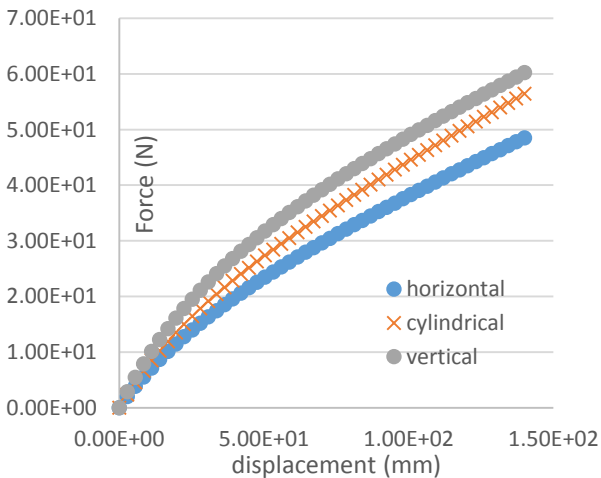


Figure 6.8: Force Displacement Curve

Figure 6.8 shows force displacement of all configuration. Blue dots represent horizontal, x marks represent cylindrical, and grey dots represent vertical configuration data. The data from all configuration shows different behavior. It has its own modulus in all displacement value. Horizontal configuration has the lowest force at final displacement. It has 48.5 N at its final displacement which is 140 mm. The cylindrical configuration has the medium force at final displacement compare to all configuration. It has 36.4 N at the final displacement. The vertical configuration has the highest force at the final displacement. It has 60.2 N at the final displacement.

The behavior of all configuration is nonlinear. The horizontal configuration starts to have lower force displacement ratio at early stage. It began to lose the ratio at 11.5 mm displacement. After that point the ratio is nearly unchanged. The cylindrical configuration has different behavior at 20.4 mm displacement. However, there is no significant changes.

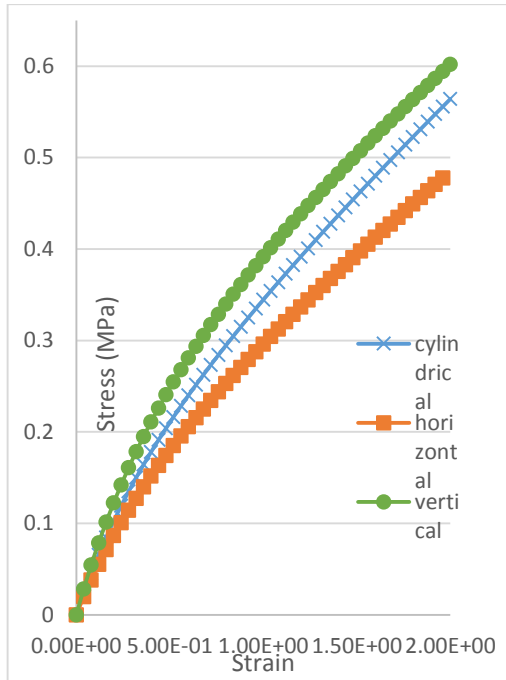


Figure 6.9: Simulation Stress Strain Curve

Figure 6.9 shows simulation stress strain data. The squared orange line represents horizontal configuration data, the crossed blue line represents cylindrical configuration data, and the green dotted line represents vertical configuration data. The strongest configuration is vertical configuration followed by cylindrical configuration and horizontal configuration. The comparison between simulation and experimental stress strain behavior is shown in Figure 6.10.

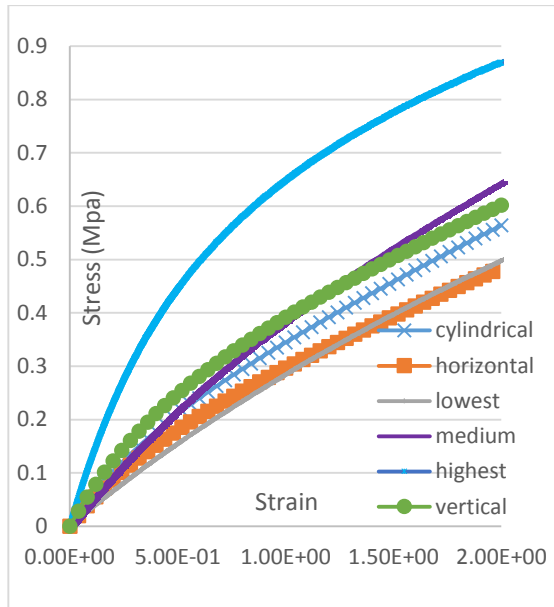


Figure 6.10: Stress-Strain Curve Experimental and Simulation Comparison

As shown in Figure 6.10 the stress strain responses of all the configuration does not reach the strength of the highest TS material. All of the simulated stress is in between the lowest TS and medium TS material. However, the behavior from each configuration does not match with neither lowest TS nor Medium TS. The slope of all configuration are a mixture of all the three materials.

The stress comparison between experimental and simulation data are shown in Figure 6.11

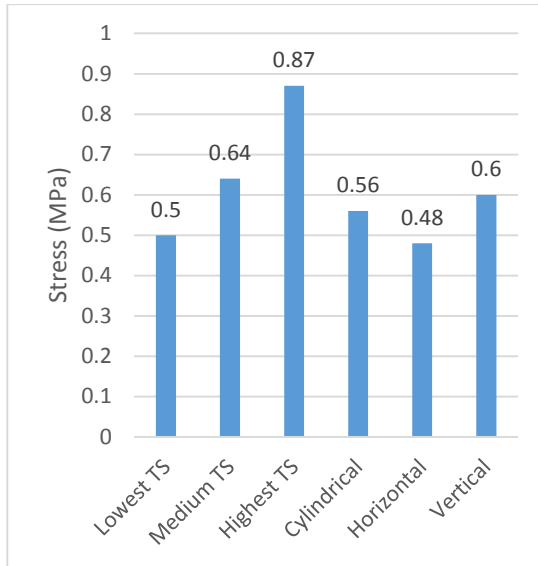


Figure 5: Stress at Strain 2 Simulation and Experimental

Figure 6.11 shows a bar chart of stress at strain equals 2 for simulation and experimental. The stresses shown are the comparison for simulation and experiment when the specimen has elongate 2 times its original shape. All simulation data does not reach the medium TS stress level which is at 0.64 MPa. The lowest stress happen with horizontal configuration with 0.48 MPa, and the medium one is cylindrical configuration with 0.56 MPa, and the highest stress is vertical configuration. although the horizontal configuration stress is lower than the lowest TS the slope of horizontal configuration is higher when the specimen elongation is in between 0 until 1.5.

6.3.3 STRAIN ENERGY DENSITY

The strain energy density for all configuration are shown in Figure 6.12

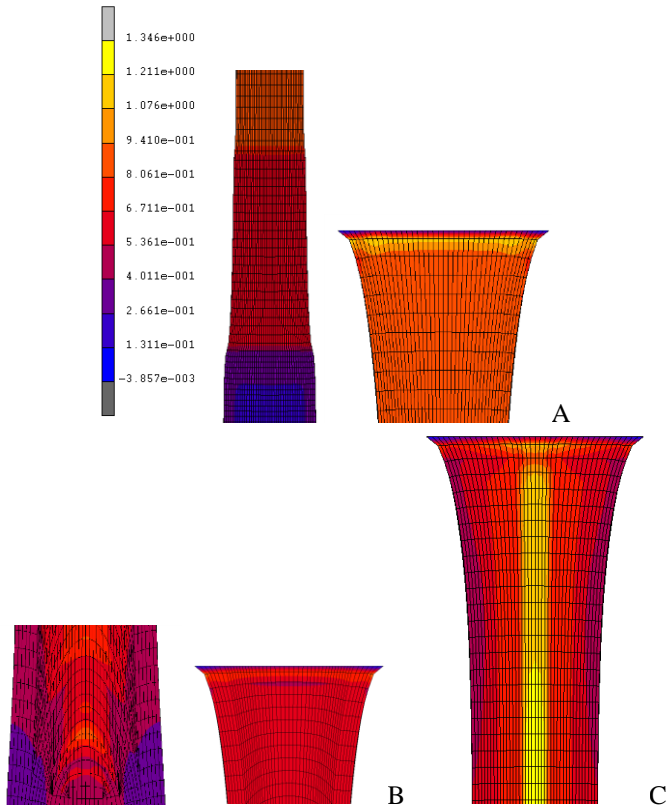


Figure 6.12 : Strain Energy Density Contour (A. horizontal, B. cylindrical, C. vertical)

Figure 6.12 shows SED contour for all configuration. The results shown are SED contour at final increment of test. The figure is focus on the SED critical area only. The SED from each configuration has unique behavior. Figure 4.12 A shows horizontal configuration SED. It shows that the critical area is located near the edges of coupon, it is indicated by bright yellow color. Figure 4.12 B shows cylindrical configuration SED. It shows that the overall SED is lower than the horizontal configuration level, the SED is concentrated at the junction of each material junction either along the stretch direction or lateral from the stretch direction. Figure 4.12 C shows a SED of vertical configuration. It shows that SED

is spread along the highest TS material at the center, with small concentration at the edge of coupon compare to horizontal configuration.

The behavior on horizontal configuration is the most critical condition compare to the other case since the concentration is only concentrated at the 4 edges of coupon. This concentration might happen because as the increase of strain the necking starts occur on all edges all the work energy will be concentrated at the radius of the necking.

Cylindrical configuration behavior is similar with the previous researcher result in which the SED concentration is exist along the material junction. Overall the mesh distortion level on the junction is tolerable since the highest distortion does not occur badly and it is not on the most critical zone. The highest SED concentration is located at the junction of different material along the stretch direction. Vertical configuration behavior is the best in terms of SED concentration locality since the area is spread out along the highest TS.

6.4 CONCLUSIONS

The conclusions for this study are:

1. The model successfully replicate experimental data, with stress strain curves from the simulation showed the strongest case is vertical arrangement with TS at strain equals to 2 % 0.6MPa, follows by cylindrical and horizontal of 0.56MPa and 0.48 Mpa.
2. The strain energy density from each case has some specific area with the bigger scalar. For horizontal case is the area near the top and bottom edge, while for cylinder case is in between the material contact at the top and bottom, for vertical case is distributed along the highest material TS.

REFERENCES

- [1] MSC. Software, “*Nonlinear Finite Element Analysis of Elastomers.*”
- [2] O. H. Yeoh, *Some Forms of the Strain Energy Function for Rubber*, vol. 66. 1993.
- [3] R. W. Ogden, “*Large Deformation Isotropic Elasticity: On the Correlation of Theory and Experiment for Compressible Rubberlike Solids,*” *Proc. R. Soc. A Math. Phys. Eng. Sci.*, vol. 328, no. 1575, pp. 567–583, 1972.
- [4] S. Kut, G. Rzyzińska, And Niedziałek, “*The Influence Of Material Model Of The Polyurethane Elastomer On The Fem Calculations Quality For The Various Modes Of Loading The,*” vol. 62, pp. 523–530, 2017.
- [5] K. M. Moerman, C. K. Simms, and T. Nagel, “*Control of tension – compression asymmetry in Ogden hyperelasticity with application to soft tissue modelling,*” *J. Mech. Behav. Biomed. Mater.*, vol. 56, pp. 218–228, 2016.
- [6] J. Kaden, “*Computational Simulations Of Fiber Reinforced Hyperelastic Materials,*” McGill University, 2007.
- [7] D. Kuksenko, H. J. Böhm, and B. Drach, “*Advances in Engineering Software Effect of micromechanical parameters of composites with wavy fibers on their effective response under large deformations,*” *Adv. Eng. Softw.*, vol. 121, no. May, pp. 206–222, 2018.
- [8] L. A. Mihai, L. K. Chin, P. A. Janmey, and A. Goriely, “A

comparison of hyperelastic constitutive models applicable to brain and fat tissues,” J. R. Soc. Interface, vol. 12, no. 110, 2015.

[9] I. D. Breslavsky, M. Amabili, and M. Legrand, “*Static and Dynamic Behavior of Circular Cylindrical Shell Made of Hyperelastic Arterial Material,*” vol. 83, no. May 2016, pp. 1–9, 2019.

[10] D. Kokkinis, F. Bouville, and A. R. Studart, “*3D Printing of Materials with Tunable Failure via Bioinspired Mechanical Gradients,*” *Adv. Mater.*, vol. 30, no. 19, pp. 1–9, 2018

CHAPTER 7

A COMPREHENSIVE REVIEW OF COLLAGEN SCAFFOLD IN MUSCULOSKETEL TISSUE ENGINEERING

Mohd Syahir Anwar Hamzah¹, Syuhaimi Yusof¹, Syahirah Mohd Noor¹, Saiful Izwan Abd Razak² and Nadirul Hasraf Mat Nayan^{1,2*}

¹Faculty of Engineering Technology, Universiti Tun Hussein Onn Malaysia, Pagoh Higher Education Hub, KM 1 Jalan Panchor, 84600 Pagoh, Johor.

²Center of Advanced Composite Material, Faculty of Engineering, Universiti Teknologi Malaysia, 86000 Skudai, Johor.

³Microelectronic and Nanotechnology-Shamsuddin Research Centre (MiNT-SRC), Integrated Engineering Institute, Universiti Tun Hussein Onn Malaysia, 86400 Parit Raja, Johor.

*Corresponding author: nadirul@uthm.edu.my

Abstract

Musculosketel tissue healing process limitation is unable to restore significant tissue loss due to congenital defects, tumor denervation or trauma. Tissue engineering is a novel approach that attempts to overcome these problems by investigating potential alternative treatment using temporary matrix scaffold formed by biocompatible materials. Collagen is natural based biomaterials which mostly derived from animal have been studies for a long time in tissue engineering domains especially in musculosketel tissue replacement applications such as bone and cartilage. The wide ranges of collagen sources with unique properties such as porous structure, good permeability, low immunogenicity and biocompatible make collagen are versatile scaffold materials in tissue engineered research. Here, we discuss comprehensively different sources of collagen with main properties; modifications had been done in biomedical engineering and highlight the application of collagen and its contribution in musculosketel tissue engineering fields.

Keyword: Tissue engineering, musculoskeletal tissue, collagen, bone tissue, tendon tissue, cartilage tissue.

7.1 INTRODUCTION

Human organs possess the ability to maintain their homeostasis, circulate blood and adjust accordingly as a response to several changes from their surrounding environment. However, loss of functionality, either due to aging or to disease/injury, is in fact inevitable [1]. The musculoskeletal system, which provides mechanical support and permits movement, is composed of skeletal muscle, tendons, bones, joints and ligaments. Skeletal muscles act as contractile levers, and are connected to bone by tendons [2-3]. Bones act as rigid levers, articulating with other bones through joints, which are kept in relationship by ligaments. A special characteristic of muscle, tendons and joints is the possession of a rich sensory nerve supply, which detects the position of the body and the velocity of movement. The integration of this sensory information by the central nervous system is vital for the musculoskeletal system to function normally [4]. Bone come second most transplanted tissue globally after blood with over two million bone grafting surgeries per annum [5]. Bone regeneration is the complex phenomenon in which active signaling from different biomolecules is required at various stages of bone development. Small size bone fracture whether it might be pathological or accidental can be repaired by bone's own regeneration capability [6]. Nevertheless, damaged tissues and even whole organs have the opportunity of regeneration, assisted by traditional medical treatment, transplantation and finally, alternative novel strategies that have emerged from the promising field of regenerative sciences [7-8]. Tissue engineering is a broad area that produces tools of solution for the problems in medical areas such as scaffold fabrication.

Tissue engineering defined as the combination of biological, chemical, and engineering principles for developing biological substitutes that repair, replace, maintain, or improve tissue function or a whole organ using cells, biomaterials, and growth factors alone or in combination [9]. Therefore, tissue engineering seems to be as a key technology to close gaps in the management of major tissue defects in

reconstructive surgery and could obviate many of the risks and problems associated with donor organs, and at lower cost [10]. In recent years, the importance of convergent research integrating tissue engineering, advanced materials, and stem cells with the seemingly disparate disciplines of physical sciences and developmental biology has been recognized, and a new research direction has been proposed and termed as “regenerative engineering” [11].

Substances frequently used for scaffolds include natural polymeric materials, synthetic polymers or ceramics, biodegradable polymers, or polymers with adsorbed proteins or immobilized functional groups. Naturally occurring matrices or their components have advantages because of their outstanding biocompatibility properties [12-13]. Popular ECM molecules of connective tissues are collagen, hyaluronan, and glycosaminoglycans. Collagens have been used in native form or as denatured gelatin which found most abundant protein in the animal. In plant and unicellular organisms, the collagen is not existed because their polysaccharides and cellulose takes its role [14]. The collagen consists 25-30% of protein in mammals where found in the corneas, bones, blood vessels, cartilage, teeth and many more [15]. The elongated fibrils are found in the area of fibrous tissues such as tendons, ligaments and skin. The muscle tissue form of 1-2% where the most is endomysium component. Therefore, the fibroblast of connective tissues and other epithelial cells are the most constitutes the collagen [16-17].

This review will discuss a summary approach of collagen applications for engineering cartilage and bone. The basic structure, properties and modification techniques were discussed comprehensively to give overview on collagen before it can be claimed as superior biomaterial in musculosketel tissue engineering applications. Thus, its use in tissue engineering could be significant in enhancing and mimicking the natural musculosketel environment.

7.2 BASIC STRUCTURE OF COLLAGEN

The structure of collagen is classified into three polypeptide chain where it is sort of triple helix with the two identical chains (α_1) and the third is different in their extent of chemical composition (α_2) (as illustrate in Figure 1). Therefore, it can be categorized as hetero-polymer which each chains contains 1050 amino acids while another in typical-handed helical structure has 300nm long and its diameter around 1.5nm with molecular weight is about 2900000 [18-19]. The structure of collagen has repeating of Gly-X-Y, where X and Y refer to any amino acid but mostly of it is hydroxyproline and proline. The glycine is located in each of third amino acid which allowed the firm packaging 3 α chains in tropocollagen molecule [20]. The packing of collagen is come in hexagonal and a quasi hexagonal shape which is forms a type of fibrillar collagen where the packing structure is likely microfibrillar and sheet-like. Hence, the collagen can be representing as elongated fibrils [21].

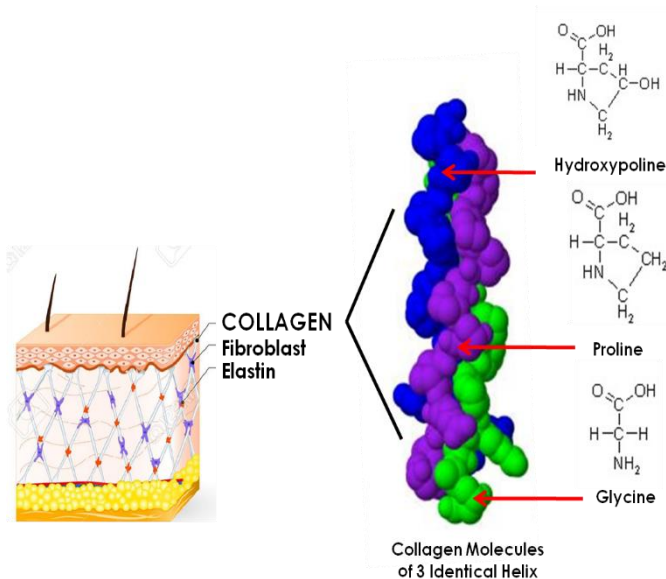


Figure 7.1: Basic structure of collagen fibers.

Previous studies showed that the collagen has led to discover approximately 33 different types of collagenous polypeptides which occupy with at least 33 different gene sequences. There are 19 different collagen types of polypeptides from types I to types XIX that occurred in extracellular matrix [22]. The basic collagen types are consisting of types I, II, III, V and XI where called as fibril-forming. Among the collagen types, it can be known based on their ability of assemble into highly orientated supramolecular aggregates that has characteristic of supra-structure and typical quarter-staggered fibril array between diameter 25 to 400 nm. The fibrils have characteristic banding pattern with periodicity about 70nm by using electron microscope. It can be determined from staggered arrangement individual collagen [23].

Type I collagen is by far the most important. More than 90% of collagen forming in bone, tendons, skin, ligaments, cornea and interstitial connective tissue except a few tissues such as vitreous body, brain and hyaline cartilage. Type I can be incorporated into composite whether with type III collagen (in reticular fibres and skin) or type V collagen (in bone, cornea, tendon) which it called as triple helical fibres, in vivo [24-26]. It has been found that type I collagen shows tensile stiffness in tendons and fascia, while in bone, tensile strength, torsional stiffness and load bearing was provided after calcification [26-27].

The fibril-forming type II collagen is the characteristic and predominant component of hyaline cartilage. It is, however, not specifically restricted to cartilage where it accounts for about 80% of the total collagen content since it is also found in the vitreous body, the corneal epithelium, the notochord, the nucleus pulposus of intervertebral discs, and embryonic epithelial mesenchymal transitions [28]. Compared to type I collagen, type II collagen chains show a higher content of hydroxyl-lysine as well as glucosyl and galactosyl residues which mediate the interaction with proteoglycans, another typical component of the highly hydrated matrix of hyaline cartilage [29]. Type III collagen is a homotrimer of three $\alpha 1(\text{III})$ chains and is widely distributed in collagen I containing tissues with the exception of bone. It is an important component of reticular fibres in the interstitial tissue of the lungs, liver, dermis, spleen, and vessels. This homotrimeric molecule also often contributes to mixed fibrils with type I collagen and is also abundant in

elastic tissues [27,30].

Types V and XI collagens are formed as heterotrimers of three different α -chains ($\alpha 1$, $\alpha 2$, $\alpha 3$). It is remarkable that the $\alpha 3$ -chain of type XI collagen is encoded by the same gene as the $\alpha 1$ -chain of type II collagen and only the extent of glycosylation and hydroxylation differs from $\alpha 1(\text{II})$ [31]. Although it is finally not sorted out, a combination between different types V and XI chains appears to exist in various tissues. Thus, types V and XI collagens form a subfamily within fibril-forming collagens, though they share similar biochemical properties and functions with other members of this family. As mentioned before, type V collagen typically forms heterofibrils with types I and III collagens and contributes to the organic bone matrix, corneal stroma and the interstitial matrix of muscles, liver, lungs, and placenta [32]. Type XI collagen distributes largely in articular cartilage with type II collagen. The large amino-terminal non-collagenous domains of types V and XI collagens are processed only partially after secretion and their incorporation into the heterofibrils is thought to control their assembly, growth, and diameter [33].

Literally, more research about collagen, more discoveries of new types of collagen has been found until type XXVIII in zebrafish nervous system, liver, thymus muscle, intestine and skin [28]. Thus from that, the group or classes of types collagen has been made due to smaller the scope. Current classifications are based largely on primary structure, and collagenous molecules can be grouped into three categories on the basis of the respective sizes of their collagenous triple helices (Kielty, 2002). Collagens in Group 1 consists of types I, II, III, V, and XI. Group 2 comprises collagen types IV and VII, whose component polypeptides are distinguished by their primary structures characterized by imperfections in the Gly– X Y triplet sequence. Group 3 comprises short-chain collagens. This grouping has been subdivided into Group 3A, 3B and 3C which is from types VI to XIX.

7.3 PROPERTIES OF COLLAGEN

Collagen supports most of the tissues in the form of extracellular matrix and gives structure to the cells. It has great tensile strength exhibited by its presence in tendons, bones, cartilage, fascia, etc. It provides elasticity and strength to the skin and helps in tissue and organ development. Collagen provides protection to skin by inhibiting the absorption of toxins and pathogens [34]. It has a role in biological functions of a cell (cell survival, proliferation and differentiation), helps in healing of damaged bones or blood vessels and maintains structural integrity [35].

Collagen (Figure 7.2) products are used in drugs and medicine for several functions, including wound dressings and as matrices for tissue growth. As the chief structural protein of the body, the properties of collagen that make it appropriate for use in medicine are unit dependent upon characteristics of amino acid composition and sequence. There are several physical, chemical, and biological properties of collagen that favor the use of collagen as a biomaterial of the nineties; they are high tensile strength, orientation of fibers, semipermeability of membranes, low-antigenicity, its positive effect on wound healing rates and hemostatic properties [36]. Hydrolyzed collagen is outlined as a collagen product peptide derived by reaction having a molecular weight of 1,000 to 10,000. Hydrolyzed collagen is offered as a viscous, amber aqueous solution or most typically, as off-white to white hygroscopic powder. It will absorb up to thirty times its own weight in water. Any one of three methods commercially prepares it: base-forming reaction, enzymatic reaction or acid hydrolysis; and it is commercially derived from either bovine or porcine sources.

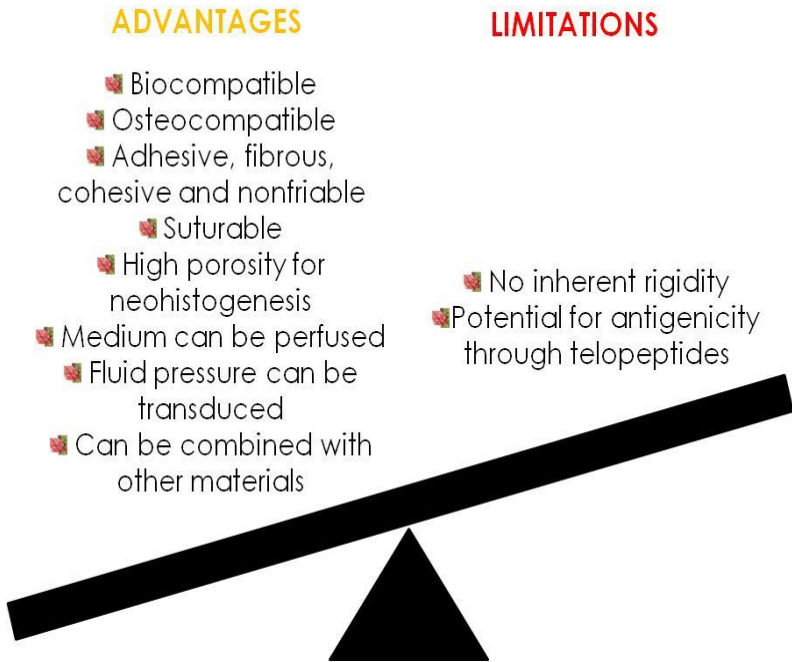


Figure 7.2: Properties of Collagen as Scaffold

Collagen has several distinctive biological characteristics for that no artificial substitute exists. Type I collagen is used in several applications due to its borderline antigenicity, its styptic capability, its chemotactic properties, and it is without delay offered from several natural sources. Collagen, the principal structural protein, is the main component of animal tissue, while sort I collagen is the dominant constituent occupying over 90% of the tissue [37-38]. The use of Type I collagen as a wound dressing dates back nearly 85 years (REF). Collagen has been ready in varied forms such as films, powders, sponges and gels. The commercialization method of collagen to date has been terribly slow primarily because of the high value of preparation, difficulties of handling and storage, and its cost-effectiveness during application [39-41]. In a number of reports collagen has been shown to be useful by

dominant the evaporation of fluid, keeping the wound pliable and flexible, promoting the development of connective tissue, diminishing pain, providing mechanical protection against physical and bacterial insult [42].

The use of collagen within the management of tissue regeneration is a survival as an aid to increased healing. The animal tissue is created from soft animal tissue (the gingival corium) and the connective tissues of the periodontal ligament and the superjacent epithelial tissue [43]. The gingival extends from its limiting margin in the cervical region of a tooth to the alveolar mucosa covering the bony alveolar processes of the jaws. The gingival dermis attaches to each the alveolar bone and the cervical bone and the cervical region of the tooth protects and maintains the integrity of the periodontal ligament [44-45]. Organic chemistry studies show that the main components of animal tissue connective tissue area unit sort I and sort III collagen, Type I collagen being the principal constituent. The main fibrillar part of the gum is sort I collagen; a heavier concentration of Type I collagen is conjointly found within the deeper layers of the animal tissue dermis. Inflammation of the gingiva or periodontal disease is one of the foremost common dental diseases for humans. If not controlled or treated, it will result in disease with a slow progressive destruction of the ligament and alveolar bone [43,46]. A mucosa membrane whose structure resembles that of the skin lines the mouth or oral mucosa. It is composed of two layers, the overlying epithelial tissue and an underlying connective tissue. The structure of this membrane varies with the functional necessities of the very different regions of the oral cavity; for example, areas involved in the change of state of food like the gingivae and tongue have a way very different structure than that of the floor of the mouth [47]. The oral mucous membrane is created from primarily sort I collagen, representing approximately 80-90% of the total collagen content [48].

7.4 SOURCES OF COLLAGEN

7.4.1 Bovine

It makes use of the skin and bone of cow. It is one of the major industrial sources of collagen. Due to the outbreak of diseases such as BSE, TSE, FMD especially mad cow disease, which pose a threat to the humans, researchers are in search for an alternative safer source of collagen. One of the major disadvantages of bovine collagen is that nearly 3% of the population is allergic to it causing a hindrance in its usage. Bovine Achilles tendon is used industrially to obtain type I collagen. Type IV is obtained from the placental villi and type II from nasal or articular cartilage [49]. Bovine is made use of in different development stages such as *fet al* bovine dermis used for tendon reinforcement, skin and wound healing (in the form of collagen matrix); neonatal bovine dermis is used for hernia repair, plastic and reconstructive surgery; adult bovine pericardium for hernia repair and muscle flap reinforcement [50].

7.4.2 Porcine

The skin and bones of pigs are utilized. This source is widely used for obtaining collagen for industrial purpose. Since porcine collagen is almost similar to human collagen it does not cause much allergic response when used but just like the bovine source the setback of zoonosis poses a risk of contamination and pigs are forbidden due to religious constrains. Adult porcine dermis and small intestinal mucosa is used for tendon reinforcement, hernia repair, skin and wound healing, plastic and reconstructive surgery [51].

7.4.3 Marine

Marine source is found to be the safest source for obtaining collagen presently. Another reason for approving this source is due to the belief that “life originated from marine”. Collagen extraction from animal source is complex, time consuming and expensive. The yield obtained is also lower when compared to other sources

(approximately 12 g of collagen per 1 kg of the raw material used). Due to the concern over adverse inflammatory and immunologic response and prevalence of various diseases among land animals which causes health complications, marine sources have started to be researched [52-53]. Marine source has got ample advantages over the land animal sources such as free of zoonosis such as BSE, TSE and FMD, High content of collagen, Environment friendly has lower body temperature than animals thereby aid in greater absorption, Greater absorption due to low molecular weight, Less significant religious and ethical constrains, Minor regulatory and quality control problems, Presence of biological contaminants and toxins almost negligible, Low inflammatory response, Less immunogenic and Metabolically compatible. This source includes the use of marine invertebrates and vertebrates such as fishes, star fish, jellyfish, sponges, sea urchin, octopus, squid, cuttlefish, sea anemone and prawn [54-56].

7.4.4 Fishes

The bones, skin, fins, scales of fresh or salt water fishes are mainly used for this purpose. This in turn helps to reduce environmental pollution as these are the considered a waste during fish processing. Study of collagen from marine origin comprises of marine vertebrates and invertebrates. Vertebrates include mainly the fishes [57]. Collagen mainly type I was obtained from the skin of *Gadusmorhua*. Silver carp *Hypophthalmichthysmolitrix*. Japanese sea-bass, chub mackerel bullhead shark and sole fish. Then, the bone (sole fish) of collagen I is acquired from *Thunnusobesus*, skipjack tuna, Japanese sea-bass, yu, yellow sea bream, fin of horse mackerel, scales of Japanese sea-bass, *Pagrus major*, *Oreochromisniloticas*, Carp [58].

7.4.5 Other Animal Sources

It includes chicken, kangaroo tail, rat tail tendon, duck feet, equine tendon (horse), alligators bone and skin, bird feet, sheep skin (ovine source), frog skin and sometimes even from humans [59]. Recombinant human collagen is used which lower immunogenicity

has compared to other sources. Adult equine pericardium is used for tendon reinforcement, skin and wound healing and hernia repair. Type I and II collagen is isolated from equine skin, articular cartilage and flexor tendon [51]. Collagen type I, II, III and V were obtained from chicken neck among which type I was predominant. Chicken feet are an abundant source of collagen. Type IX is also found in the chicken embryo sternal cartilage and type I and III from its skin, type IV from its muscular tissues [60-61]. Type I collagen was also obtained from the fallopian tube of bull frog. From invertebrate tissue of *Archaeogastropod*, *Neritacrepidularia*, *gastropod* collagen was characterized [62].

7.5 MODIFICATION OF COLLAGEN FOR BIOMEDICAL APPLICATION

7.5.1 Physical Modification

Physical modification is widely considered simple, cheap and safe since it requires no chemical reagents [63-64]. During physical modification process, dehydrathermal treatment, ultraviolet irradiation and gamma-ray radiation are extensively investigated [65]. Note that, recently, new physical modification method plasma has attracted scientists' attention in impacting collagen with novel physicochemical properties. However, physical modification has a drawback of lower crosslinking efficacy than chemical modification.

7.5.1.1 Dehydrathermal (DHT) Treatment

Crosslinking collagen with the method of dehydrathermal (DHT) treatment is a common approach of physical modification. During DHT treatment, amide bonds form between the free carboxyl and amine group within collagen triple helixes, thus enhancing the physicochemical properties of collagen and collagenous scaffolds to some extent, for instance, the tensile strength, elongation at break, elasticity modulus, resistance to enzymatic degradation and thermal stability are increased compared to non crosslinked collagen and collagenous materials [66-67]. Usually, during DHT treatment, collagen or collagenous materials are firstly placed in a vacuum

furnace with 0.05mbar vacuum degree at about 40°C for 2-4h to remove free-water from collagen or collagenous materials which protects them from thermal denaturation. Subsequently, DHT treatment was performed on collagen specimens with different temperatures (100°C, 150°C or 200°C) for 24-48h approximately. After that, the temperature of vacuum furnace should be cooled down to room temperature to obtain cross-linked collagen specimens [66,68]. Note that, crosslinking and denaturation of collagen occurs simultaneously during the DHT treatment. Cross linking treatment plays a vital role in DHT treatment when the temperature is low, whereas denaturation is usually maximum when the temperature is higher than 150°C [69]. Haugh et al. reported that crosslink density was found to increase with DHT temperature, but not exposure period, and denaturation degree increased sharply when DHT temperature was higher than 150°C. Thus, DHT treatment at 110°C for 24h may be optimum for collagen crosslinking [70].

7.5.1.2 Ultraviolet (UV) Irradiation Modification

Exposure of collagen to non-ionizing irradiation by ultraviolet(UV) light can enhance collagen properties. The double bonds and aromatic rings within collagen molecule can absorb UV irradiation to induce free radical formation in amino acids (tyrosine or phenylalanine), which can further cause the formation of inter-molecular covalent bonds [71-72]. Usually, UV at 184.9 and 253.7nm wavelengths are used to excite molecular oxygen to form ozone and to photosensitize polymer surface, then oxygen-containing functional groups (carboxyl and hydroxyl groups) could be incorporated into collagen or collagenous materials [73]. Liu et al. applied the UV irradiation technique on a three dimensional collagen scaffold for surface modification. The surface modification of crosslinking-treated collagen scaffolds by exposure to UV led to a further increase in surface oxygen concentration and promoted the surface wettability of the collagen scaffolds [74]. Crosslinking with UV light for more than 30min and less than 180 min seems to be more beneficial to cell proliferation than chemical crosslinking by using glutaraldehyde. A combination technique of DHT treatment and 45 min of UV exposure produced the optimal collagen matrix in

terms of contraction rate, mechanical property and cell growth [75]. UV modification can also be used in the field of corneal collagen crosslinking. Usually, a combined technique of photo-chemical reaction between ultraviolet light-A and riboflavin is used for corneal collagen crosslinking [76].

7.5.1.3 Gamma-ray Radiation Modification

Gamma-ray radiation is commonly used to cross-link collagen and collagenous material just as in polymerization of other synthetic polymers, for instance, polyvinyl alcohol (PVA), and polyvinyl pyrrolidone (PVP) [77]. Exposure to ray irradiation is a frequent, clean, and superior method used to prevent bacterial contamination of sterilized induced by gamma ray irradiation of collagen is of concern due to the decay of bioactivity, which correlates with considerable structural alterations [78]. Note that, both crosslinking and scission occur when collagen and collagenous materials are exposed to gamma radiation. Generally, crosslinking plays a primary role when the sample is in a wet condition, in contrast, scission i.e. disruption or denaturation is the predominant behaviour in a dry protein sample [79]. Tyan et al. suggest that gamma radiation exposure of about 10 KGy is the critical dose to moderate the bioactivities of collagen and causes amide degradation to collagen [80]. In the case of gamma-crosslinking, a hydroxyl radical ($\bullet\text{OH}$) is firstly formed by splitting a water molecule under gamma irradiation, and subsequently can attack the polymer molecule as a primary intermediate molecular species to form a polymer radical. Then, the polymer radical can form intermolecular crosslinking or degradation by inter- or intramolecular reaction, respectively [36].

7.5.2 Chemical Modification

Chemical modification involves the introduction of functional groups into collagen molecules, resulting in markedly altered physicochemical properties than physical modification. Such modification of native collagen molecules profoundly changes the thermal stability, gelatinization, degradation and conformation

characteristics. Usually, chemical modification is intended to facilitate intra- and inter- molecular bonds within collagen structure for stabilization [81]. Usually, during the chemical modification, some chemical reagents are strongly recommended, for instance, glutaraldehyde, carbodiimide, genipin, plant tannins, polyepoxy compound, acyl azide, and dialdehyde compound derived from natural biomass [82]. Although collagen or collagenous materials are always endowed with higher stability by chemical modification, the biocompatibility of modified collagen should not be ignored when chemical modification is applied.

7.5.2.1 Glutaraldehyde Modification

Traditionally, aldehyde, especially glutaraldehyde, has been firstly applied in the leather industry to improve the stability of hide or skin. After that, glutaraldehyde is being used to modify collagen to protect it from being degraded by collagenases [83]. Fathima et al. researched the stabilization of collagen by aldehydes by choosing four aldehydes, both mono- and dialdehydes, formaldehyde, crotonaldehyde, glyoxal and glutaraldehyde. Compared with native collagen, glutaraldehyde did promote the shrinkage temperature from $62\pm 1^\circ\text{C}$ to $82\pm 1^\circ\text{C}$, much more than that of crotonaldehyde ($77\pm 1^\circ\text{C}$) [72]. Other researchers claim that Schiff bases are not so stable and they can react with a glutaraldehyde-related enol, which results in the formation of a secondary amine, thereby forming a six membered dihydropyridine. Usually, glutaraldehyde vapour is more effective to cross-link collagen and collagenous scaffolds in the field of tissue engineering as compared to glutaraldehyde solution. Although after cross-linked by glutaraldehyde, the collagenous scaffolds reveal a significant resistance to enzymatic degradation and their solubility and antigenicity are effectively reduced, and adverse biological reactions to glutaraldehyde have been limited to infrequent contact dermatitis [84].

7.6 APPLICATIONS OF COLLAGEN SCAFFOLD IN MUSCULOSKELTEL TISSUE ENGINEERING

Bone and cartilage reconstruction are necessary topics of trendy musculoskeltel medication either for purposeful or esthetic surgery. Collagen-based biomaterial implantation is necessary once osteochondral defects reach a crucial volume or when transplant need to be avoided for sensible or pathological reasons [85]. Scaffolds for bone tissue engineering rely on hardening of a collagen biomaterial by mineralization with calcium phosphate and/or on crosslinking with other substances like hydroxyapatite or brushite. Collagen has been used as implantable carriers for bone inducing proteins, such as bone morphogenetic protein 2 (rhBMP-2) [86-89]. Recently, collagen itself was used as bone substitutes due to its osteo-inductive activity. The uses of collagen film as gene delivery carriers for osteo-induction and collagen sponge for bone related protein carriers [87-88]. Type I collagen crosslinked *N*-telopeptide was used as a marker of bone resorption and clinically used as a marker of bone metastasis of prostate cancer and breast cancer [90-92].

Regenerating articular cartilage and fibrocartilaginous tissue such as the meniscus is still a challenge in orthopedic medicine. While a range of different scaffolds have been developed for joint repair, none have facilitated the development of a tissue that mimics the complexity of soft tissues such as articular cartilage. Furthermore, many of these scaffolds are not designed to function in mechanically challenging joint environments [93]. Collagen-based biomaterials used for cartilage regeneration tend to be additional versatile and are ideally engineered with type II collagen in distinction to most of the different collagen-based biomaterials, which are created victimization type I collagen. Nonetheless, some studies demonstrate that small amounts of autologous chondrocytes will grow in dynamic culture on type I or II collagen structures with none notable distinction [94]. Further developments aimed at differentiating mesenchymal stem cells directly in collagen-based biomaterial, to permanently solve osteochondral defects on a semipermanent basis, are presently underneath investigation [95]. Optimization of pore size and distribution is additionally a priority considering the impact of those parameters on cell adhesion,

proliferation and migration [96]. Decellularization of complex structures like meniscus has additionally shown promising results in order to provide an optimal replacement scaffold for specific osteochondral defects [97]. Table 7.1 summarizes the current application and fabrication techniques of collagen scaffold for bone and cartilage tissue replacement.

Table 7.1: Processing material and method of collagen scaffold with summary of outcome research.

Processing Materials	Processing Method	Main Outcome	Refs
Bone Tissue Engineered Scaffold			
Collagen / beta-tricalcium phosphate (β -TCP) and strontium oxide	Freeze drying	Microporous scaffold excellent mechanical integrity (213.44 \pm 0.47 kPa) structure with high porosity (~95-99%) and pore size (100-200 μ m) give better proliferation and alkaline phosphate (ALP) activity for rat bone marrow mesenchymal stem cells.	[98]
Collagen / beta tricalcium phosphate (β -TCP)	Freeze drying	This porous scaffold has excellent mechanical (970 \pm 1.2 kPa) and porous structure with ~98% porosity and 120-200 μ m pore size. In vitro biocompatibility studied of rat bone marrow mesenchymal stem cells show scaffold promoted vascularization with good integration which	[99]

		effectively activates the differentiation of stem cells into osteoblasts.	
Collagen / carbon nanotube / chitosan / hydroxyapatite	Freezing and lyophilization	Artificial bone scaffold with increased mechanical strength (524 to 1112 kPa) exhibits good in-vitro bioactivity due to nucleation of osteoinductive HA with interconnecting porous structure (95.7±0.1% porosity with 20-350 µm pore size)	[100]
Collagen / polyurethane / bioactive glass / ceramics	Polymer blend and coating	The collagen/polyurethane blend coated with glass-ceramic by surface-silanisation produced well developed substrate for bone cell adhesion and growth by mimicking the composite nature of the bone ECM.	[101]
Collagen / recombinant bone morphogenetic protein-2 (rhBMP-2) / vascular endothelial growth factor (VEGF) / O-carboxymethyl chitosan	Calcination	The double factors composite sustained release system showed that rhBMP-2/VEGF in composite scaffolds successfully achieved the sequential release of double factors that significantly promote osteogenesis effect.	[102]

microspheres (O-CMCS)			
Collagen / fibrin	Polymerization	The hydrogel has excellent stem cell function (including cell viability, morphology, proliferation and gene expression of human mesenchymal stem cell / human umbilical vein endothelial cell (MSC/HUVEC) spheroids) and able to generate pre-vascularized network which provided suitable 3D microenvironment for bone tissue formation	[103]
Collagen / hydroxyapatite	Sponge template and coating	The microporous composite demonstrated that the porosity of scaffold was reducing due to lower compressive pressure (50% compressive ratio) and high sintering temperature (1000-1200°C).	[104]
Collagen / hyaluronic acid / poly (L-lactide-co-ε-caprolactone)	Electrospinning	The microfibrillar scaffold has high water uptake capacity (103%) and better supported adipose-derived mesenchymal stem cell adhesion. Besides, this scaffold would eliminate the immune	[105]

		response triggered by xenogeneic collagen and transmission of animal-borne disease while promoting a better vascular network formation.	
Collagen / phosphorylated chitosan	Biomimetic mineralization	The process of mineralization collagen fibrils encapsulated by nanoapatite mineral nanocrystals can be shortened within 96 hours by using phosphorylated chitosan which created new nucleation sites on the fibers that allow amorphous calcium phosphate attachment for bone tissue regeneration.	[106]
Cartilage Tissue Engineered Scaffold			
Collagen / gold nanoparticle	Coating	Biocompatibility study using keratinocytes cell showed that higher cell viability on functionalized gold nanoparticle mediated collagen materials which highly suitable for skeletal tissue application.	[107]
Collagen alginate	3D printing	The 3D scaffold able to facilitate cell adhesion, accelerated <u>cell proliferation</u> and enhanced the expression	[108]

		of cartilage specific genes such as <i>Acan</i> , <i>Col2a1</i> and <i>Sox 9</i> . Besides, the result showed the scaffold effectively suppressed dedifferentiation of chondrocytes and preserved phenotype.	
Collagen type I and II	Polymer blend	Cryo-scanning electron microscopy images confirmed lower void space percentages can be achieved at 36.4% with superior mechanical properties ($G^* = 5 \text{ Pa}$) which can implemented for articular tissue substitute.	[109]
Collagen alginate /	Crosslink and freezing	The aligned pore structure improved the mechanical properties and promoted higher levels of sulfated glycosaminoglycans (sGAG) and collagen deposition compared to an isotropic (nonaligned) pore geometry when seeded with adult human stem cells. This led to greater cell proliferation, higher sGAG and collagen accumulation, and the development of a stiffer tissue scaffold.	[110]
Collagen riboflavin /	Photo-crosslinking	The photo-crosslinking scaffold improved the	[93]

		mechanical properties, delayed enzyme-triggered degradation of collagen scaffolds and enhanced gene expression level for collagen type II and aggrecan.	
Collagen / silk / poly lactic-co-glycolic acid (PLGA)	Lyophilisation	The in vitro fluorescence staining of bone marrow stromal cells revealed that the composite scaffold enhanced cell proliferation without eliciting side effects. The prepared composite scaffold was implanted in fully thick articular cartilage defects in rabbits showed the enhancement of articular cartilage regeneration and integration between the repaired cartilage and the surrounding cartilage.	[111]

7.7 CONCLUSION

Collagens are the most abundant group of organic macromolecules in an organism. First, collagens serve important mechanical functions within the body, particularly in connective tissues. Thus, in bone, tendon, fascia, articular cartilage, and many more, fibrillar collagens are providing most of the biomechanical properties essential for the functioning of these organ systems. Second, collagens also exert important functions in the cellular microenvironment and are involved in the storage and release of cellular mediators, such as growth factors. All aspects mentioned above define collagens as interesting targets as well as tools of pharmacological intervention. A proper collagen matrix in

terms of its composition and supramolecular organization is the target of any repair process of connective tissue whether occurring naturally, like during fracture healing or following treatment of bone non-unions after trauma, tumor-surgery or of cartilage defects has been discuss. Finally, it should be considered that some additional features of collagens, such as biodegradability, low immunogenicity and the possibilities for large-scale isolation make them interesting compounds for a widespread industrial use in medicine, cosmetics or food industry.

ACKNOWLEDGEMENT

The authors would like to express the deepest appreciation to the Ministry of Education Malaysia (KPM) through Malaysian Technical University Network (MTUN) Grant (MTUN-Vote number 124) and Universiti Tun Hussein Onn Malaysia (UTHM) through the Geran Penyelidikan Pascasiswazah (GPPS-Vote number H458) and Industrial Grant (Vote number M009) for funding this research.

REFERENCES

- [1] Whaley, M. M., & Barber, D. L. (2017). The Aging Process. *Occupational Therapy with Elders-eBook: Strategies for the COTA*, 30.
- [2] Neumann, D. A. (2013). *Kinesiology of the musculoskeletal system-e-book: foundations for rehabilitation*. Elsevier Health Sciences.
- [3] Whiting, W. C., & Zernicke, R. F. (2008). *Biomechanics of musculoskeletal injury*. Human Kinetics.
- [4] Senior, K. R. (Ed.). (2010). *Bone and Muscle: Structure, Force, and Motion*. The Rosen Publishing Group, Inc.
- [5] Campana, V., Milano, G., Pagano, E., Barba, M., Cicione, C., Salonna, G., Lattanzi, W. & Logroscino, G. (2014). Bone substitutes in orthopaedic surgery: from basic science to clinical practice. *Journal of Materials Science: Materials in Medicine*, 25(10), 2445-2461.
- [6] Kumar Meena, L., Rather, H., Kedaria, D., & Vasita, R. (2019). Polymeric microgels for bone tissue engineering applications—a review. *International Journal of Polymeric Materials and Polymeric Biomaterials*, 1-17.

- [7] Engel, E., Michiardi, A., Navarro, M., Lacroix, D., & Planell, J. A. (2008). Nanotechnology in regenerative medicine: the materials side. *Trends in Biotechnology*.
- [8] Fontana, F., Ferreira, M. P. A., Correia, A., Hirvonen, J., & Santos, H. A. (2016). Microfluidics as a cutting-edge technique for drug delivery applications. *Journal of Drug Delivery Science and Technology*, 34, 76–87
- [9] Ma, L., Gao, C., Mao, Z., Zhou, J., Shen, J., Hu, X., & Han, C. (2003). Collagen/chitosan porous scaffolds with improved biostability for skin tissue engineering. *Biomaterials*, 24(26), 4833–4841.
- [10] Griffith, L. G., & Naughton, G. (2002). Tissue engineering--current challenges and expanding opportunities. *science*, 295(5557), 1009–1014.
- [11] Spector, M. (2006). Biomaterials-based tissue engineering and regenerative medicine solutions to musculoskeletal problems. *Swiss Medical Weekly*, 136(19–20), 293–301.
- [12] Porter, J. R., Ruckh, T. T., & Papat, K. C. (2009). Bone tissue engineering: a review in bone biomimetics and drug delivery strategies. *Biotechnology progress*, 25(6), 1539-1560.
- [13] Gohil, S. V., Suhail, S., Rose, J., Vella, T., & Nair, L. S. (2017). Polymers and composites for orthopedic applications. In *Materials for Bone Disorders* (pp. 349-403). Academic Press.
- [14] Cromar, L. G. (2014). *The Structure, Function and Evolution of the Extracellular Matrix: A Systems-Level Analysis* (Doctoral dissertation).
- [15] Silvipriya, K. S., Kumar, K. K., Bhat, A. R., Kumar, B. D., John, A., & Lakshmanan, P. (2015). Collagen: Animal sources and biomedical application. *J Appl Pharm Sci*, 5(3), 123-127.
- [16] Di Lullo, G. A., Sweeney, S. M., Körkkö, J., Ala-Kokko, L., & San Antonio, J. D. (2002). Mapping the ligand-binding sites and disease-associated mutations on the most abundant protein in the human, type I collagen. *Journal of Biological Chemistry*, 277(6), 4223-4231.

- [17] Neel, E. A. A., Bozec, L., Knowles, J. C., Syed, O., Mudera, V., Day, R., & Hyun, J. K. (2013). Collagen—emerging collagen based therapies hit the patient. *Advanced drug delivery reviews*, 65(4), 429-456.
- [18] Mienaltowski, M. J., & Birk, D. E. (2014). Structure, physiology, and biochemistry of collagens. In *Progress in heritable soft connective tissue diseases* (pp. 5-29). Springer, Dordrecht.
- [19] Theocharis, A. D., Skandalis, S. S., Gialeli, C., & Karamanos, N. K. (2016). Extracellular matrix structure. *Advanced drug delivery reviews*, 97, 4-27.
- [20] Castillo, N. C. (2014). Bioactive Sutures to Prevent Fibrosis in Injured Skeletal Muscle Tissue.
- [21] Abustam, E., Tawali, A. B., & Said, M. I. (2018). Chemical Composition, Amino Acid and Collagen Content of Snakehead (*Channa striata*) Fish Skin and Bone.
- [22] Kielty, C. M., & Grant, M. E. (2002). The collagen family: structure, assembly, and organization in the extracellular matrix. *Connective tissue and its heritable disorders: molecular, genetic, and medical aspects*, 159-221.
- [23] Holmes, D. F., Gilpin, C. J., Baldock, C., Ziese, U., Koster, A. J., & Kadler, K. E. (2001). Corneal collagen fibril structure in three dimensions: structural insights into fibril assembly, mechanical properties, and tissue organization. *Proceedings of the National Academy of Sciences*, 98(13), 7307-7312.
- [24] Balasubramanian, P., Prabhakaran, M. P., Sireesha, M., & Ramakrishna, S. (2012). Collagen in human tissues: structure, function, and biomedical implications from a tissue engineering perspective. In *Polymer Composites–Polyolefin Fractionation–Polymeric Peptidomimetics–Collagens* (pp. 173-206). Springer, Berlin, Heidelberg.
- [25] Von Der Mark, K., & Park, J. (2013). Engineering biocompatible implant surfaces. Part II: cellular recognition of biomaterial surfaces: lessons from cell–matrix interactions. *Prog Mater Sci*, 58(3), 327-81.
- [26] Ehrlich, H. (2010). Marine Collagens. *Biological Materials of Marine Origin*, 427-441.

- [27] Gelse, K., Pöschl, E., & Aigner, T. (2003). Collagens—structure, function, and biosynthesis. *Advanced drug delivery reviews*, 55(12), 1531-1546.
- [28] Dong, C., & Lv, Y. (2016). Application of collagen scaffold in tissue engineering: recent advances and new perspectives. *Polymers*, 8(2), 42.
- [29] Gelse, K., Pöschl, E., & Aigner, T. (2003). Collagens—structure, function, and biosynthesis. *Advanced drug delivery reviews*, 55(12), 1531-1546.
- [30] Nielsen, M. J., & Karsdal, M. A. (2016). Chapter 3-Type III Collagen. *Biochemistry of Collagens, Laminins and Elastin*.
- [31] Perdivara, I., Yamauchi, M., & Tomer, K. B. (2013). Molecular characterization of collagen hydroxylysine O-glycosylation by mass spectrometry: current status. *Australian journal of chemistry*, 66(7), 760-769.
- [32] Shiba, M., Shimizu, I., Yasuda, M., Ii, K., & Ito, S. (1998). Expression of type I and type III collagens during the course of dimethylnitrosamine- induced hepatic fibrosis in rats. *Liver*, 18(3), 196-204.
- [33] Frisenda, S., Perricone, C., & Valesini, G. (2013). Cartilage as a target of autoimmunity: a thin layer. *Autoimmunity reviews*, 12(5), 591-598.
- [34] Silvipriya, K. S., Kumar, K. K., Bhat, A. R., Kumar, B. D., John, A., & Lakshmanan, P. (2015). Collagen: Animal sources and biomedical application. *J Appl Pharm Sci*, 5(3), 123-127.
- [35] Barrientos, S., Stojadinovic, O., Golinko, M. S., Brem, H., & Tomic- Canic, M. (2008). Growth factors and cytokines in wound healing. *Wound repair and regeneration*, 16(5), 585-601.
- [36] Madanagopal, T. T., Agarwalla, S. V., & Rosa, V. (2019). Carbon nanocomposites for implant dentistry and bone tissue engineering. In *Applications of Nanocomposite Materials in Dentistry* (pp. 47-63). Woodhead Publishing.
- [37] Pal, G. K., & Suresh, P. V. (2016). Sustainable valorisation of seafood by-products: recovery of collagen and development of collagen-based novel functional food ingredients. *Innovative food science & emerging technologies*, 37, 201-215.
- [38] Morgan, P. E., Pattison, D. I., & Davies, M. J. (2012). Quantification of hydroxyl radical-derived oxidation products in peptides

- containing glycine, alanine, valine, and proline. *Free Radical Biology and Medicine*, 52(2), 328-339.
- [39] Wang, Y., Azaïs, T., Robin, M., Vallée, A., Catania, C., Legriél, P., Pehau-Arnaudet, G., Babonneau, F., Giraud-Guille, M.M. & Nassif, N. (2012). The predominant role of collagen in the nucleation, growth, structure and orientation of bone apatite. *Nature materials*, 11(8), 724.
- [40] Gautieri, A., Vesentini, S., Redaelli, A., & Buehler, M. J. (2011). Hierarchical structure and nanomechanics of collagen microfibrils from the atomistic scale up. *Nano letters*, 11(2), 757-766.
- [41] Sivan, S. S., Hayes, A. J., Wachtel, E., Caterson, B., Merkher, Y., Maroudas, A., & Roberts, S. (2014). Biochemical composition and turnover of the extracellular matrix of the normal and degenerate intervertebral disc. *European Spine Journal*, 23(3), 344-353.
- [42] Han, S. K. (2015). *Innovations and advances in wound healing*. Springer.
- [43] Guo, S. A., & DiPietro, L. A. (2010). Factors affecting wound healing. *Journal of dental research*, 89(3), 219-229.
- [44] Reddy, S. (2017). *Essentials of Clinical Periodontology & Periodontics*. JP Medical Ltd.
- [45] Wang, H. L., & Neiva, R. F. (2008). Socket augmentation: rationale and technique. *Fundamentals of Esthetic Implant Dentistry*, 209.
- [46] Lucas, P. W. (2004). *Dental functional morphology: how teeth work*. Cambridge University Press.
- [47] Short, L. M. (2012). Future Of The Profession–The Times They Are Changing.
- [48] Almela, T., Al-Sahaf, S., Brook, I. M., Khoshroo, K., Rasoulianboroujeni, M., Fahimipour, F., Tahriri, M., Dashtimoghadam, E., Bolt, R., Tayebi, L., & Moharamzadeh, K. (2018). 3D printed tissue engineered model for bone invasion of oral cancer. *Tissue and Cell*, 52, 71-77.
- [49] Ahuja, T., Dhakray, V., Mittal, M., Khanna, P., Yadav, B., & Jain, M. (2012). Role of collagen in the periodontal ligament-A Review. *The Internet Journal of Microbiology*, 10(1).
- [50] Parenteau-Bareil, R., Gauvin, R., & Berthod, F. (2010). Collagen-based biomaterials for tissue engineering applications. *Materials*, 3(3), 1863-1887.

- [51] Cortial, D., Gouttenoire, J., Rousseau, C. F., Ronzière, M. C., Piccardi, N., Msika, P., Herbage, D., Mallein-Gerin, F., & Freyria, A. M. (2006). Activation by IL-1 of bovine articular chondrocytes in culture within a 3D collagen-based scaffold. An in vitro model to address the effect of compounds with therapeutic potential in osteoarthritis. *Osteoarthritis and cartilage*, 14(7), 631-640.
- [52] Addad, S., Exposito, J. Y., Faye, C., Ricard-Blum, S., & Lethias, C. (2011). Isolation, characterization and biological evaluation of jellyfish collagen for use in biomedical applications. *Marine drugs*, 9(6), 967-983.
- [53] Exposito, J. Y., Cluzel, C., Garrone, R., & Lethias, C. (2002). Evolution of collagens. *The anatomical record*, 268(3), 302-316.
- [54] KRISHNAN, S., & PERUMAL, P. (2013). Preparation and biomedical characterization of jellyfish (*Chrysaora quinquecirrha*) collagen from southeast coast of India. *structure*, 8, 11.
- [55] Sugiura, H., Yunoki, S., Kondo, E., Ikoma, T., Tanaka, J., & Yasuda, K. (2009). In vivo biological responses and bioresorption of tilapia scale collagen as a potential biomaterial. *Journal of Biomaterials Science, Polymer Edition*, 20(10), 1353-1368.
- [56] Song, E., Kim, S. Y., Chun, T., Byun, H. J., & Lee, Y. M. (2006). Collagen scaffolds derived from a marine source and their biocompatibility. *Biomaterials*, 27(15), 2951-2961.
- [57] Liang, J., Pei, X. R., Wang, N., Zhang, Z. F., Wang, J. B., & Li, Y. (2010). Marine collagen peptides prepared from chum salmon (*Oncorhynchus keta*) skin extend the life span and inhibit spontaneous tumor incidence in sprague-dawley rats. *Journal of medicinal food*, 13(4), 757-770.
- [58] Hashim, P., Ridzwan, M. M., Bakar, J., & Hashim, M. D. (2015). Collagen in food and beverage industries. *International Food Research Journal*, 22(1), 1.
- [59] Wood, A., Ogawa, M., Portier, R. J., Schexnayder, M., Shirley, M., & Losso, J. N. (2008). Biochemical properties of alligator (*Alligator mississippiensis*) bone collagen. *Comparative Biochemistry and Physiology Part B: Biochemistry and Molecular Biology*, 151(3), 246-249.
- [60] Hutmacher, D. W. (2000). Scaffolds in tissue engineering bone and cartilage. In *The Biomaterials: Silver Jubilee Compendium* (pp. 175-189). Elsevier Science.

- [61] Quereshi, S., Mhaske, A., Raut, D., Singh, R., Mani, A., & Patel, J. (2010). Extraction and partial characterization of collagen from different animal skins. *Recent Research in Science and Technology*, 2(9).
- [62] Palpandi, C., Ramasamy, P., Rajinikanth, T., Vairamani, S., & Shanmugam, A. (2010). Extraction of collagen from mangrove archaeogastropod *Nerita* (*Dostia*) *crepidularia* Lamarck, 1822. *American-Eurasian Journal of Scientific Research*, 5(1), 23-30.
- [63] Ding, C., Zhang, M., Wu, K., & Li, G. (2014). The response of collagen molecules in acid solution to temperature. *Polymer*, 55(22), 5751-5759.
- [64] Zork, N. M., Myers, K. M., Yoshida, K., Cremers, S., Jiang, H., Ananth, C. V., & Vink, J. (2015). A systematic evaluation of collagen cross-links in the human cervix. *American journal of obstetrics and gynecology*, 212(3), 321-e1.
- [65] Zhu, B., Li, W., Lewis, R. V., Segre, C. U., & Wang, R. (2014). E-spun composite fibers of collagen and dragline silk protein: fiber mechanics, biocompatibility, and application in stem cell differentiation. *Biomacromolecules*, 16(1), 202-213.
- [66] Yu, X., Tang, C., Xiong, S., Yuan, Q., Gu, Z., Li, Z., & Hu, Y. (2016). Modification of collagen for biomedical applications: a review of physical and chemical methods. *Current Organic Chemistry*, 20(17), 1797-1812.
- [67] Hortensius, R. A. (2016). *Bioinspired alterations of collagen-glycosaminoglycan scaffolds for tissue regeneration applications* (Doctoral dissertation, University of Illinois at Urbana-Champaign).
- [68] Lee, K. W. (2010). *Interactions Between IGFBP-3 and Nuclear Receptors in Prostate Cancer Apoptosis*. CALIFORNIA UNIV LOS ANGELES.
- [69] Haugh, M. G., Jaasma, M. J., & O'Brien, F. J. (2009). The effect of dehydrothermal treatment on the mechanical and structural properties of collagen- GAG scaffolds. *Journal of Biomedical Materials Research Part A: An Official Journal of The Society for Biomaterials, The Japanese Society for Biomaterials, and The Australian Society for Biomaterials and the Korean Society for Biomaterials*, 89(2), 363-369..

- [70] Haugh, M. G., Murphy, C. M., McKiernan, R. C., Altenbuchner, C., & O'Brien, F. J. (2011). Crosslinking and mechanical properties significantly influence cell attachment, proliferation, and migration within collagen glycosaminoglycan scaffolds. *Tissue Engineering Part A*, 17(9-10), 1201-1208.
- [71] Wihodo, M., & Moraru, C. I. (2013). Physical and chemical methods used to enhance the structure and mechanical properties of protein films: A review. *Journal of food engineering*, 114(3), 292-302.
- [71] Wihodo, M., & Moraru, C. I. (2013). Physical and chemical methods used to enhance the structure and mechanical properties of protein films: A review. *Journal of food engineering*, 114(3), 292-302.
- [72] Fathima, N. N., Madhan, B., Rao, J. R., Nair, B. U., & Ramasami, T. (2004). Interaction of aldehydes with collagen: effect on thermal, enzymatic and conformational stability. *International Journal of Biological Macromolecules*, 34(4), 241-247.
- [73] Sionkowska, A., Kozłowska, J., & Lazare, S. (2014). Modification by UV radiation of the surface of thin films based on collagen extracted from fish scales. *Biointerphases*, 9(2), 029003.
- [74] Liu, C., McKenna, F. M., Liang, H., Johnstone, A., & Abel, E. W. (2010). Enhanced cell colonization of collagen scaffold by ultraviolet/ozone surface processing. *Tissue Engineering Part C: Methods*, 16(6), 1305-1314.
- [75] Lew, D. H., Liu, P. H. T., & Orgill, D. P. (2007). Optimization of UV cross- linking density for durable and nontoxic collagen GAG dermal substitute. *Journal of Biomedical Materials Research Part B: Applied Biomaterials*, 82(1), 51-56.
- [76] Dias, J. M., & Ziebarth, N. M. (2013). Anterior and posterior corneal stroma elasticity assessed using nanoindentation. *Experimental eye research*, 115, 41-46.
- [77] HARA, M. (2006). Various cross-linking methods for collagens: merit and demerit of methods by radiation. *Journal of Oral Tissue Engineering*, 3(3), 118-124.
- [78] Gruskin, E., Doll, B. A., Futrell, F. W., Schmitz, J. P., & Hollinger, J. O. (2012). Demineralized bone matrix in bone repair: history and use. *Advanced drug delivery reviews*, 64(12), 1063-1077.
- [79] Davidenko, N., Bax, D. V., Schuster, C. F., Farndale, R. W., Hamaia, S. W., Best, S. M., & Cameron, R. E. (2016). Optimisation of UV irradiation as a binding site conserving method for crosslinking

- collagen-based scaffolds. *Journal of Materials Science: Materials in Medicine*, 27(1), 14.
- [80] Tyan, Y. C., Liao, J. D., Lin, S. P., & Chen, C. C. (2003). The study of the sterilization effect of gamma ray irradiation of immobilized collagen polypropylene nonwoven fabric surfaces. *Journal of Biomedical Materials Research Part A: An Official Journal of The Society for Biomaterials, The Japanese Society for Biomaterials, and The Australian Society for Biomaterials and the Korean Society for Biomaterials*, 67(3), 1033-1043.
- [81] Taraballi, F., Zanini, S., Lupo, C., Panseri, S., Cunha, C., Riccardi, C., & Cipolla, L. (2013). Amino and carboxyl plasma functionalization of collagen films for tissue engineering applications. *Journal of colloid and interface science*, 394, 590-597.
- [82] Huang, G. P., Shanmugasundaram, S., Masih, P., Pandya, D., Amara, S., Collins, G., & Arinzeh, T. L. (2015). An investigation of common crosslinking agents on the stability of electrospun collagen scaffolds. *Journal of Biomedical Materials Research Part A*, 103(2), 762-771.
- [83] Liu, Y., Ma, L., & Gao, C. (2012). Facile fabrication of the glutaraldehyde cross-linked collagen/chitosan porous scaffold for skin tissue engineering. *Materials science and engineering: c*, 32(8), 2361-2366.
- [84] Kikuchi, M., Matsumoto, H. N., Yamada, T., Koyama, Y., Takakuda, K., & Tanaka, J. (2004). Glutaraldehyde cross-linked hydroxyapatite/collagen self-organized nanocomposites. *Biomaterials*, 25(1), 63-69.
- [85] Correlo, V. M., Oliveira, J. M., Mano, J. F., Neves, N. M., & Reis, R. L. (2011). Natural origin materials for bone tissue engineering e properties, processing, and performance. *Principles of regenerative medicine*, 2, 557-586.
- [86] Li, R. H., & Wozney, J. M. (2001). Delivering on the promise of bone morphogenetic proteins. *Trends in biotechnology*, 19(7), 255-265.
- [87] Pina, S., Oliveira, J. M., & Reis, R. L. (2015). Natural- based nanocomposites for bone tissue engineering and regenerative medicine: A review. *Advanced Materials*, 27(7), 1143-1169.
- [88] Trombetta, R., Inzana, J. A., Schwarz, E. M., Kates, S. L., & Awad, H. A. (2017). 3D printing of calcium phosphate ceramics for bone

- tissue engineering and drug delivery. *Annals of biomedical engineering*, 45(1), 23-44.
- [89] Shinohara, Y., Nakamura, T., Shirakata, Y., & Noguchi, K. (2016). Bone healing capabilities of recombinant human bone morphogenetic protein-9 (rhBMP-9) with a chitosan or collagen carrier in rat calvarial defects. *Dental materials journal*, 35(3), 454-460.
- [90] Gibbs, D. M. R., Black, C. R. M., Hulsart-Billstrom, G., Shi, P., Scarpa, E., Oreffo, R. O. C., & Dawson, J. I. (2016). Bone induction at physiological doses of BMP through localization by clay nanoparticle gels. *Biomaterials*, 99, 16-23.
- [91] Huang, Q., & Ouyang, X. (2012). Biochemical-markers for the diagnosis of bone metastasis: a clinical review. *Cancer Epidemiology*, 36(1), 94-98.
- [92] Schiano, C., Soricelli, A., De Nigris, F., & Napoli, C. (2019). New challenges in integrated diagnosis by imaging and osteoimmunology in bone lesions. *Expert review of clinical immunology*, 15(3), 289-301.
- [93] Heo, J., Koh, R. H., Shim, W., Kim, H. D., Yim, H. G., & Hwang, N. S. (2016). Riboflavin-induced photo-crosslinking of collagen hydrogel and its application in meniscus tissue engineering. *Drug delivery and translational research*, 6(2), 148-158.
- [94] Otto, I., Levato, R., Webb, W., Khan, I., Breugem, C., & Malda, J. (2018). Progenitor cells in auricular cartilage demonstrate cartilage-forming capacity in 3D hydrogel culture. *European cells & materials*, 35, 132-150.
- [95] Paxton, N. C., Powell, S. K., & Woodruff, M. A. (2016). Biofabrication: The future of regenerative medicine. *Techniques in Orthopaedics*, 31(3), 190-203.
- [96] Huang, Z. (2017). *In vitro differentiation of chondrogenic cells in three-dimensional scaffold-assisted culture for cartilage repair and characterization of cartilage sources* (Doctoral dissertation).
- [97] Nürnberger, S., Schneider, C., van Osch, G. V. M., Keibl, C., Rieder, B., Monforte, X., & Gahleitner, C. (2019). Repopulation of an auricular cartilage scaffold, AuriScaff, perforated with an enzyme combination. *Acta biomaterialia*, 86, 207-222.
- [98] Goodarzi, H., Hashemi-Najafabadi, S., Baheiraei, N., & Bagheri, F. (2019). Preparation and Characterization of Nanocomposite

- Scaffolds (Collagen/ β -TCP/SrO) for Bone Tissue Engineering. *Tissue Engineering and Regenerative Medicine*, 1-15.
- [99] Baheiraei, N., Nourani, M. R., Mortazavi, S. M. J., Movahedin, M., Eyni, H., Bagheri, F., & Norahan, M. H. (2018). Development of a bioactive porous collagen/ β - tricalcium phosphate bone graft assisting rapid vascularization for bone tissue engineering applications. *Journal of Biomedical Materials Research Part A*, 106(1), 73-85.
- [100] Türk, S., Altinsoy, I., Efe, G. Ç., Ipek, M., Özacar, M., & Bindal, C. (2018). 3D porous collagen/functionalized multiwalled carbon nanotube/chitosan/hydroxyapatite composite scaffolds for bone tissue engineering. *Materials Science and Engineering: C*, 92, 757-768.
- [101] Caddeo, S., Mattioli-Belmonte, M., Cassino, C., Barbani, N., Dicarolo, M., Gentile, P., & Ciardelli, G. (2019). Newly-designed collagen/polyurethane bioartificial blend as coating on bioactive glass-ceramics for bone tissue engineering applications. *Materials Science and Engineering: C*, 96, 218-233.
- [102] Dou, D. D., Zhou, G., Liu, H. W., Zhang, J., Liu, M. L., Xiao, X. F., Fei, J. J., Guan, X. L., & Fan, Y. B. (2019). Sequential releasing of VEGF and BMP-2 in hydroxyapatite collagen scaffolds for bone tissue engineering: Design and characterization. *International journal of biological macromolecules*, 123, 622-628.
- [103] Heo, D. N., Hospodiuk, M., & Ozbolat, I. T. (2019). Synergistic interplay between human MSCs and HUVECs in 3D spheroids laden in collagen/fibrin hydrogels for bone tissue engineering. *Acta biomaterialia*.
- [104] Islam, M. S., Rahman, A. Z., Sharif, M. H., Khan, A., Abdulla-Al-Mamun, M., & Todo, M. (2019). Effects of compressive ratio and sintering temperature on mechanical properties of biocompatible collagen/hydroxyapatite composite scaffolds fabricated for bone tissue engineering. *Journal of Asian Ceramic Societies*.
- [105] Kenar, H., Ozdogan, C. Y., Dumlu, C., Doger, E., Kose, G. T., & Hasirci, V. (2019). Microfibrous scaffolds from poly (l-lactide-co- ϵ -caprolactone) blended with xeno-free collagen/hyaluronic acid for improvement of vascularization in tissue engineering applications. *Materials Science and Engineering: C*, 97, 31-44.

- [106] Zheng, B., Mao, C., Gu, T., Pan, H., Shao, C., Sun, J., Chen, C., Tang, R., & Gu, X. (2019). Phosphorylated chitosan to promote biomimetic mineralization of type I collagen as a strategy for dentin repair and bone tissue engineering. *New Journal of Chemistry*, 43(4), 2002-2010.
- [107] Vedhanayagam, M., Nair, B. U., & Sreeram, K. J. (2019). Effect of functionalized gold nanoparticle on collagen stabilization for tissue engineering application. *International journal of biological macromolecules*, 123, 1211-1220.
- [108] Yang, X., Lu, Z., Wu, H., Li, W., Zheng, L., & Zhao, J. (2018). Collagen-alginate as bioink for three-dimensional (3D) cell printing based cartilage tissue engineering. *Materials Science and Engineering: C*, 83, 195-201.
- [109] Vázquez-Portalatín, N., Kilmer, C. E., Panitch, A., & Liu, J. C. (2016). Characterization of collagen type I and II blended hydrogels for articular cartilage tissue engineering. *Biomacromolecules*, 17(10), 3145-3152.
- [110] Almeida, H. V., Sathy, B. N., Dudurych, I., Buckley, C. T., O'Brien, F. J., & Kelly, D. J. (2017). Anisotropic shape-memory alginate scaffolds functionalized with either type I or type II collagen for cartilage tissue engineering. *Tissue Engineering Part A*, 23(1-2), 55-68.
- [111] Wang, J., Yang, Q., Cheng, N., Tao, X., Zhang, Z., Sun, X., & Zhang, Q. (2016). Collagen/silk fibroin composite scaffold incorporated with PLGA microsphere for cartilage repair. *Materials Science and Engineering: C*, 61, 705-711.

CHAPTER 8

HYDROXYAPATITE IN BONE TISSUE APPLICATIONS

Norhana Jusoh^{1,2}

¹School of Biomedical Engineering and Health Sciences,
Faculty of Engineering,
Universiti Teknologi Malaysia, Johor Bahru,
81310 Johor, Malaysia.

²Medical Devices and Technology Centre (MEDITEC),
Institute of Human Centered Engineering,
Universiti Teknologi Malaysia, Johor Bahru,
81310 Johor, Malaysia.

8.0 INTRODUCTION

Autogenous bone grafting has been the gold standard in bone implantation due to its advantages in osteogenic capacity, osteoconduction, mechanical properties, and the lack of adverse immunological response [1]. However, these bone grafting techniques have some limitations in term of the requirement of additional surgery for harvesting, the availability of graft with sufficient size and shape, and the risk of donor site morbidity [1]. Therefore, many kinds of biomaterials have been developed as bone substitutes for bone tissue engineering [1-5]. Bone substitutes can be classified in two main categories either bone substitutes derived from biological products or synthetic bone substitutes such as ceramics, polymers, metals, and organic or non-organic bone substitutes [1,2]. Besides, the ideal bone substitutes should meet precise specifications, such as biocompatible, bioresorbable, osteoconductive, osteoinductive, structurally similar to bone, porous, mechanically resistant, easy to use, safe, and cost-effective [1,2]. Among them, hydroxyapatite (HA) have been used extensively as a substitute in bone grafts, HA have properties similarity with the bone's calcium phosphate such as the osteoconductivity and negligible

immunoreactivity. [1-5].

8.1 HYDROXYAPATITE PROPERTIES

Bone is a composite of biominerals, organic materials (which is primarily in the form of collagen) and water, as show in Figure 8.1 [4]. Besides, for elastic resistance, the collagen acts as a matrix for the deposition and growth of minerals. The biominerals comprises 65–70% of bone, which is one or more types of calcium phosphates [4]. Among the calcium phosphates, hydroxyapatite is the thermodynamically most stable crystalline phase of calcium phosphates in body fluid, possesses the most similarity to the mineral part of bone [4,5].

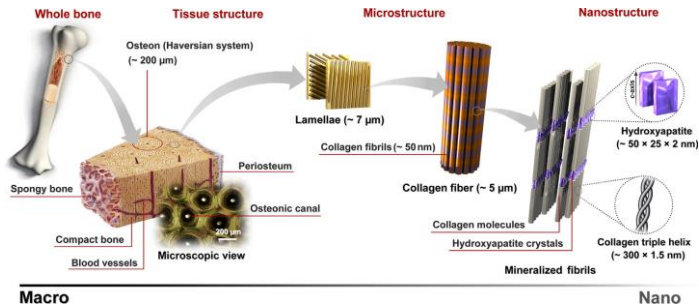


Figure 8.1: Structure of typical bone at various length scales [4].

Hydroxyapatite (HA) is part of the apatites family, which are crystalline compounds with crystalline hexagonal lattice. HA has the specific formula $(Ca_{10}(PO_4)_6(OH)_2)$ and is the primary mineral component of teeth and bones [1,2,4,5]. Thus, HA is extremely biocompatible and does not promote an inflammatory response. Natural HA is porous with a various porosity depending on the bone site that is extracted, which allows osteoconductive properties. HA can be utilized in small bone defects with low loading condition due to its very good mechanical properties with a compression resistance up to 160 MPa [4]. Synthetic HA can be made by the precipitation of calcium nitrate and ammonium dihydrogen phosphate [4]. Thus, HA resents all the

advantages of its two components such as osteoconductivity, biocompatibility, safe and nonallergen use, and promotion of bone formation [1-5].

8.2 SYNTHESIS OF HA COMPOSITES

Various approaches have been done to synthesize HA by varying nanoscale characteristics via solution-based precipitation reactions, hydrothermal synthesis, electrodeposition, or sintering [6,7]. For example, HA nanoparticles can be synthesized through a two-step process to obtain highly crystalline, as shown in Figure 8.2. Firstly, a typical precipitation reaction of a calcium salt with a phosphate salt was conducted. Then, the next step was hydrothermal aging of the precipitate in order to get particles with a narrow size distribution [7].

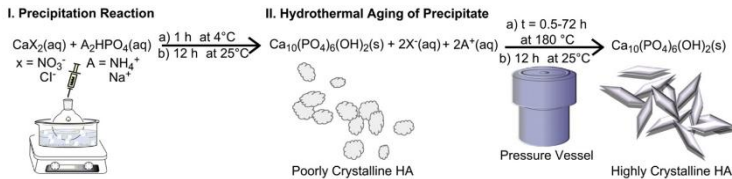


Figure 8.2: Two-step precipitation reaction to acquire crystalline HA nanoparticles [7].

The size and crystallinity of the particles can be manipulated by increasing the aging time and by varying the precursor salts [7]. From the initial precipitation reaction, the formed HA were small and poorly crystalline. Nevertheless, hydrothermally aging resulted in the formation of uniform, larger, faceted, and elongated particles with a narrow size distribution these same particles. Furthermore, the length of the rod-like particles increased with aging time, in contrast with the commercial particles that were spherical and exhibited a wide range of sizes [7].

Nevertheless, the use of HA alone may be giving disadvantages. Thus, various HA composite have been developed [8]. Figure 8.3 shows the characterization of porous non-mineralized or mineralized polymeric scaffolds fabricated by a gas foaming-particulate leaching technique [8].

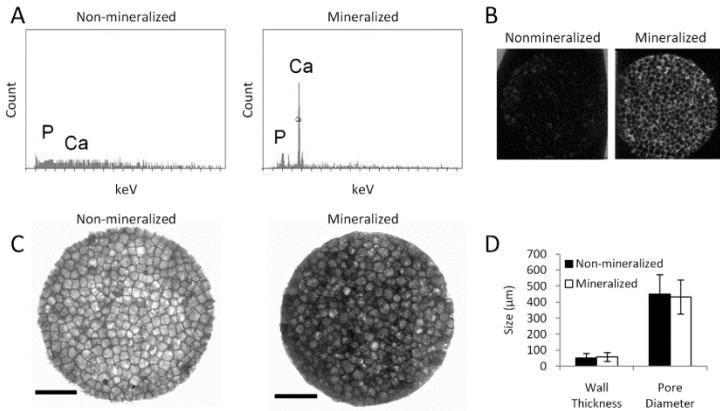


Figure 8.3: Non-mineralized and mineralized (hydroxyapatite) polymeric scaffolds fabricated by a gas foaming-particulate leaching technique [8].

A 8.5 mm diameter by 1 mm thickness porous mineralized scaffolds of poly(lactide-coglycolide) (PLG) and hydroxyapatite was prepared from a total of 8 mg of polymer, 8 mg of HA nanoparticles, and 152 mg of NaCl [8]. The scaffolds were leached in de-ionized water for 24 hours to remove NaCl porogen particles after high-pressure immersion in carbon dioxide gas and polymer foaming in a non-stirred pressure vessel. Characterization analysis indicated calcium or phosphate was available for cellular interactions at the porous surface of the mineralized scaffolds, while calcium or phosphate was undetectable for non-mineralized control scaffolds contained. Moreover, uniform distribution of HA throughout the mineralized scaffolds were observed and mineralized scaffolds exhibited compressive moduli that were 2-fold higher than for nonmineralized control scaffolds [8].

Besides, HA-collagen composites have some mechanical advantages over HA used alone. For example, this composite materials HA-collagen can enhance osteoblasts differentiation and accelerates osteogenesis. Recently, collagen–hydroxyapatite (Col–Ap) with a unique multi-level lamellar structure consisting of co-aligned micro and macro pores have been developed for bone tissue engineering [9]. This novel lamellar scaffold supports the attachment and spreading of osteoblasts. This novel scaffold has great potential to be used in bone tissue engineering applications due to its biomimetic composition, tunable structure, improved mechanical strength and good biocompatibility. Figure 8.4 shows the technique used for the preparation of the lamellar Col–Ap scaffold [9].

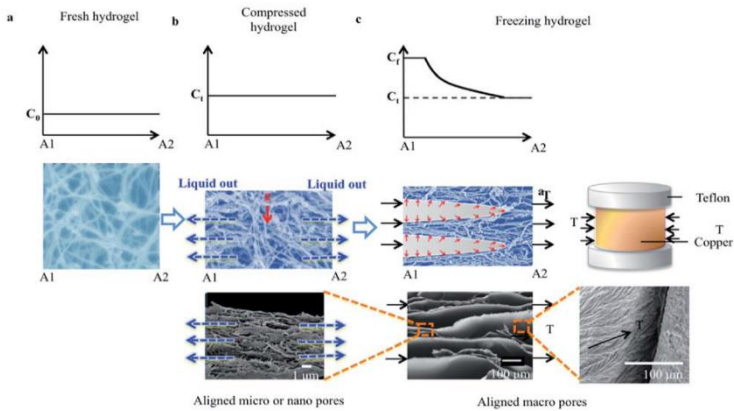


Figure 8.4: Technique used for the preparation of the lamellar Col–Ap scaffold [9].

The method based on biomimetic self-assembly process in a collagen-containing modified simulated body fluid preserved the structural integrity and great tensile strength of collagen by reinforcing the collagen hydrogel with apatite nano-particles. Besides, by controlling the freezing rate and direction, a unidirectional aligned macro-pore can be created. Depending on the self-compression time, the thickness of Col–Ap lamellae can be adjusted. Furthermore, the multilevel lamellar structure has led to a twelve-fold increase in Young's modulus and a two-

fold increase in the compression modulus along the aligned direction compared to a isotropic equiaxed pore structure scaffold [9].

In addition, compared to mechanically blended HA-polymer composites or HA-coating polymers, HA crystals deposited in situ on polymer molecule templates exhibited better bionic effects in term of crystallinity, mineralization and composites architecture [10]. Figure 8.5 shows an example of a porous scaffolds that were successfully fabricated based on 3D-printed of silk fibroin-biom mineralized hydroxyapatite (SF-HA) particles [10].

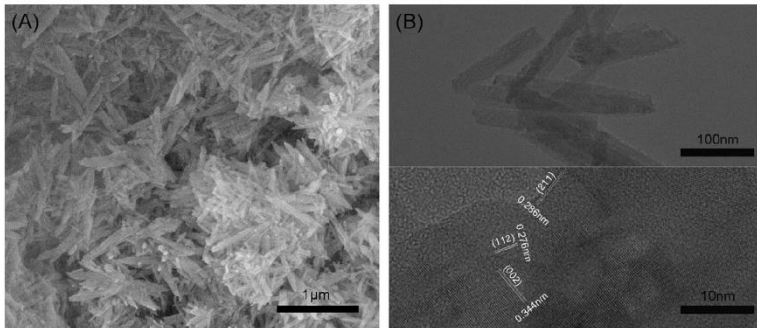


Figure 8.5: (A) SEM image of SF-HA composite powders, (B) TEM images of SF-HA composite powders at different magnifications [10].

SF-HA composite particles were produced via an in-situ mineral precipitation process by using SF molecules as the templates. With sodium alginate (SA) as printing binder, the SF-HA-SA composite scaffolds possessed a relatively high compressive strength combined with high interconnectivity and high porosity [10]. The tuneable pore structure complexity via 3D printing allowing the bone marrow mesenchymal stem cells penetration and spread all over the scaffold network in promoting the cells proliferation and osteogenic differentiation [10].

8.3 APPLICATION OF HYDROXYAPATITE IN BONE TISSUE ENGINEERING

HA is used widely as an additive and as a scaffold for promoting bone regeneration due to its excellent biocompatibility, affinity to biopolymers and high osteogenic potential [4,5]. As an appetite substitute, HA nanoparticles have been used in biomedical applications to promote cell growth and to inhibit cell apoptosis [11]. HA can promote new bone in-growth through osteoconduction mechanism without causing any local or systemic toxicity, inflammation or foreign body response [4].

The uniqueness of in-vivo bone microenvironment with inorganic mineral hydroxyapatite resulted in the need of 3D structures with interconnected pores in engineering bone tissues. [9,12]. Therefore, the incorporation of HA in bone substitutes will result in bone matrix with interconnected pores that facilitate cellular activities by maintaining enough mechanical strength to support cell adhesion, proliferation, and differentiation [12]. The addition of apatite as an inorganic reinforcing component can overcome the mechanical limits of bone substitutes since HA possesses excellent mechanical properties, including high stiffness and toughness [9,12,13].

Hydroxyapatite mineral composition is close to natural bone and less soluble than other calcium phosphates. In addition, hydroxyapatite did not increase the level of soluble calcium and phosphorous in harvested media and suggested the mineral effects was related to cell–material interactions between cell and hydroxyapatite [7]. Nowadays, with many emerging technologies, HA composite has been developed by to be used in enhancing bone tissue engineering.

8.3.1 Hydroxyapatite as Mineralized Matrix for Bone Tissue Vascularization

Vasculature has become a main goal of orthopedic tissue engineers since transplantation and engraftment of engineered tissues requires creation of a vascular supply, either through vasculogenesis or through angiogenesis. [5]. In addition, the microvascular systems have been proposed as efficient 3D in-vitro models for studying complex biological

phenomena in tissues. Similarly, HA has also been examined for its ability to promote both vasculogenesis and angiogenesis with low concentrations of HA have been shown to be compatible with endothelial cells, and to maintain the prototypical morphology and biochemical markers associated with normal endothelial cells function [5]. A study on endothelial networks formation incorporate HA in collagen-fibrin composite was conducted in 24-well plate [5].

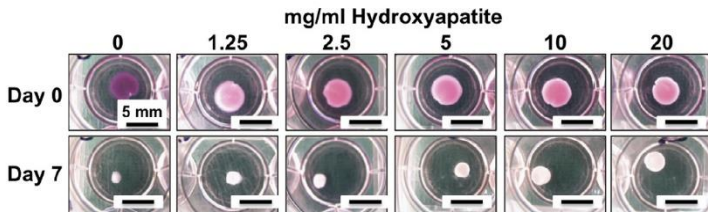


Figure 8.6: Collagen-fibrin-hydroxyapatite constructs in culture wells [5].

The finding has demonstrated that formation of endothelial networks in collagen fibrin hydrogels is affected by the culture method [5]. While the mechanism of HA-enhanced network formation *in vitro* is not clear, the effect of HA did not translate to *in vivo* subcutaneous implants, which were unaffected by the presence of HA [5].

Besides, HA also have been incorporated into microfluidic platforms to mimic the *in-vivo* bone angiogenesis that involved vessel sprouting within mineralized bone matrix, as shown in Figure 7. Fibrin was mixed with HA nanocrystals to mimic real bone tissue matrix with highly porous and interconnected structure of HA-fibrin scaffolds for the newly formed vessel sprouting [12]. Hydroxyapatite nanocrystals with sizes smaller than 200 nm were sonicated in EGM medium for 40 min for particles dilution. For obtaining the fibrin-HA matrix, the appropriate HA solutions were mixed with fibrinogen and aprotinin before mixing with thrombin [12].

The findings show that HA particles distributed homogenously in the fibrin hydrogel and the particles obviously can be seen with the increase of the HA concentrations. To prove that the distribution of HA within the fibrin in the microfluidic channel, fibrin-HA hydrogel was treated with a hydrophilic dye Trypan blue [12]. Trypan blue does not adsorb into fibrin hydrogel, but incorporation of HA in greater dye adsorption to the hydrogel. Trypan Blue that selectively stained the ceramics also was used as a nonspecific indicator of adsorption potential of HA since incorporation of HA able to alter the protein adsorption.

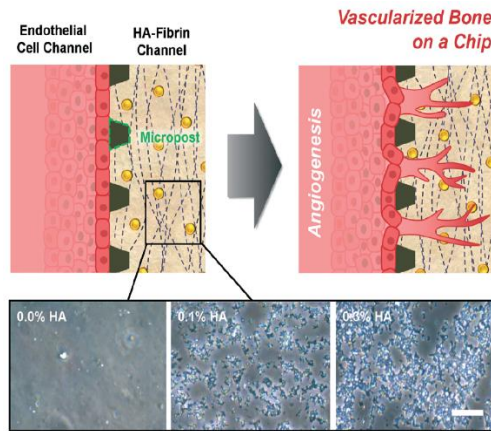


Figure 8.7: Microfluidic vascularized bone tissue model with HA-fibrin. Fibrin and HA after treatment with Trypan Blue. Scale bar: 25 μm [12].

The formation of angiogenesis network was observed with few HA concentrations. Incubation of endothelial cells with crystallized HA favored the cells adhesion, spreading and proliferation, inducing an activation of its cytoskeletal architecture without any cytotoxic effect. HA nanocrystals exhibit high biocompatibility for microvascular endothelium with maintained biochemical markers of healthy endothelium and express markers of functioning endothelium that might contribute to angiogenesis.

The formed network demonstrated the effect of HA on natural derived 3D lumen formation that have a high level of complexity which was composed of endothelial cells repulsion, junctional rearrangement and shape change [14].

Besides the chemical effects such as VEGF, mechanical cue which is matrix stiffening also gave critical effect to the blood vessel formation especially angiogenesis [15]. Hydrogels containing higher hydroxyapatite concentration were significantly stiffer than the pure hydrogel [5]. ECM stiffness can modulate capillary formation as well as barrier integrity by altering endothelial responds towards to the chemical factor [15]. Consequently, more stable and larger lumens were formed with increased gel stiffness in 3D observed on rigid gels [16,17]. Matrix stiffness also influence endothelial cells elongation and sprouting in 3D environment resulting enhancing sprouting and outgrowth [18].

8.3.2 Hydroxyapatite as Mineralized Tumor Microenvironment for Breast Cancer Bone Invasion

Many in-vitro platforms have been developed to increase the understanding of the HA role in cancer metastasis. HA mineralized microenvironment can mediate bone cancer metastasis and consequently can induce secondary breast tumor formation because of the increase in cellular adhesion and proliferation [7,8,19]. The addition of HA nanoparticles into the extracellular matrix has created a more physiological environment of in-vitro breast cancer bone metastasis [7,8,19].

A novel mineralized 3-D tumor model have been developed to investigate the pro-metastatic role of HA under physiologically relevant conditions in vitro. Non-mineralized or mineralized polymeric scaffolds fabricated by a gas foaming-particulate leaching technique were used to culture breast cancer cells [8].

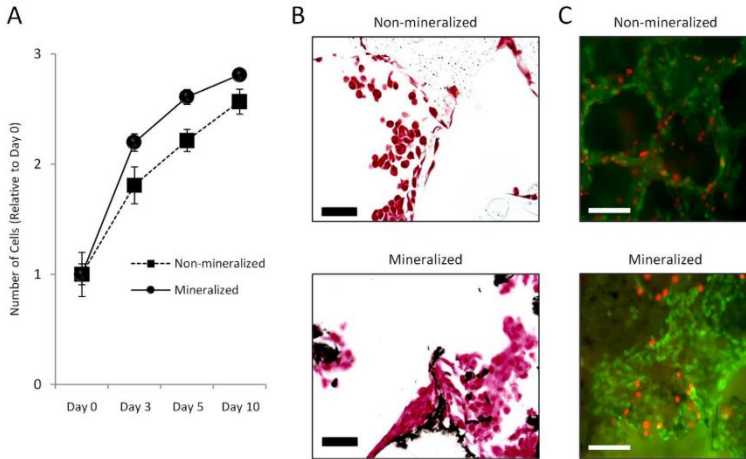


Figure 8.8: Effect of HA on 3-D tumor tissue formation [8].

The findings indicate that HA promotes features associated with the neoplastic and metastatic growth of breast carcinoma cells in bone and that interleukin-8 (IL-8) may play an important role in this process [8]. It was explained as compared to non-mineralized tumor models, tumor cell adhesion, proliferation, and secretion of pro-osteoclastic IL-8 was increased in mineralized tumor model. Furthermore, conditioned media collected from mineralized tumor models promoted osteoclastogenesis in an IL-8 dependent manner. Finally, drug testing and signaling studies with transforming growth factor beta revealed that breast cancer cell behavior is broadly affected by HA [8].

Furthermore, by integration of a novel stereolithography-based 3D printer with a unique 3D printed nano-ink consisting of hydroxyapatite nanoparticles suspended in hydrogel, a biomimetic bone-specific environment for evaluating breast cancer bone invasion has been developed [19]. HA nanoparticles were added to the printable resin in order to create a bone-specific biomimetic environment. Figure shows the image of printed HA nanoparticles.

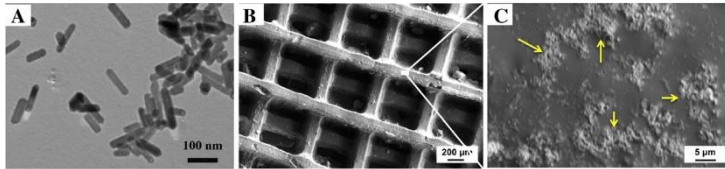


Figure 8.9: (A) TEM image of HA nanoparticles, (B) low and (C) high magnification of 10% HA nanoparticles containing small square geometry showing HA nanoparticles dispersion within the structure [19].

Bone matrices containing HA nanoparticles were printed with the determined optimal geometry, resulted in the highest proliferation and exhibited spheroid morphology and migratory characteristics. The finding demonstrated that the matrix influenced cell proliferation, and that the addition of HA nanoparticles created a more physiological model. Compared with conventional 2D cell culture, breast cancer cells growing on the 3D scaffold exhibited a greater migration capacity. Co-culture of MSCs with cancer cells on the 3D matrix resulted in increased spheroid colony formation. Therefore, this 3D scaffold may provide a promising model to study the behavior of breast cancer bone invasion and the evaluation of new therapies [19]. This 3D bone matrix can mimic tumor bone microenvironments, suggesting that it can serve as a tool for studying metastasis and assessing drug sensitivity [19].

On the other hand, HA was reported has dual effects either as assisting tumor cells metastasis or anti-proliferation of tumors with the inhibitions of HA were much more significant on cancer cells than on normal cells. HA nanoparticles have been reported to have inhibitory function on the proliferation of many kinds of tumor cells, such as breast, colon, gastric cancers and hepatoma cells [20-26]. Therefore, by manipulating the interaction of tumor cells with HA tumor microenvironment, this approach can be suggested as a promising tactic in limiting cancer progression.

8.4 CONCLUSIONS

Hydroxyapatite has been used extensively as a substitute for bone grafts due to similarity in properties with the bone's calcium phosphate. Various approaches have been done to synthesize HA that eventually resulted in the fabrication of many types of HA composites. HA composites have some mechanical advantages due to its biomimetic composition, tunable structure, improved mechanical strength and good biocompatibility. Incorporation of HA in bone matrix contribute to the interconnected pores formation that facilitated cellular activities such as cell adhesion, proliferation and differentiation. HA microenvironment has the ability in stimulating the formation of angiogenesis to mimic in-vivo bone angiogenesis that important in bone development. Besides, HA matrix able to mediate bone cancer metastasis and secondary tumor formation due to the enhancement of cellular adhesion and proliferation. With the great applications of HA in cell and tissue's study, HA has the potential as a promising biomaterial for bone substitutes as the next generation of bone grafts.

REFERENCES

- [1]. Yoshikawa H., Myoui A. (2005). *Bone tissue engineering with porous hydroxyapatite ceramics*. Journal of Artificial Organs 8(3). pp.131-136.
- [2] de Grado G.F., Keller L., Idoux-Gillet Y., Wagner, Q., Musset A.M., Benkirane-Jessel N., Bornett F., Offner D. (2018). *Bone substitutes: a review of their characteristics, clinical use, and perspectives for large bone defects management*. Journal of Tissue Engineering 9. pp. 2041731418776819.
- [3] Appleford M. R., Oh S., Oh N., Ong, J.L. (2009). *In vivo study on hydroxyapatite scaffolds with trabecular architecture for bone repair*. Journal of biomedical materials research Part A 89. pp. 1019-1027.

- [4] Sadat-Shojai M., Khorasani M.T., Dinpanah-Khoshdargi E., Jamshidi A. (2013). *Synthesis methods for nanosized hydroxyapatite with diverse structures*. Acta biomaterialia, 9(8). pp. 7591-7621.
- [5] Rao R.R., Ceccarelli J., Vigen M.L., Gudur M., Singh,R., Deng C.X., Putnam A.J., Stegemann J.P. (2014). *Effects of hydroxyapatite on endothelial network formation in collagen/fibrin composite hydrogels in vitro and in vivo*. Acta Biomaterialia 10. pp 3091-3097.
- [6] Dorozhkin, S.V., 2010. *Nanosized and nanocrystalline calcium orthophosphates*. Acta biomaterialia, 6(3). pp.715-734.
- [7] Pathi S.P., Lin D.D.W., Dorvee J.R., Estroff L.A., Fischbach C. (2011). *Hydroxyapatite nanoparticle-containing scaffolds for the study of breast cancer bone metastasis*. Biomaterials 32. pp. 5112-5122.
- [8] Pathi, S.P., Kowalczewski C., Tadipatri R., Fischbach C. (2010). *A novel 3D mineralized tumor model to study breast cancer bone metastasis*. PLoS One 5. pp. e8849 (1-10).
- [9] Xia Z., Villa M.M., Wei M. (2014). *A biomimetic collagen–apatite scaffold with a multi-level lamellar structure for bone tissue engineering*. Journal of Materials Chemistry B 2. pp. 1998-2007.
- [10] Huang T., Fan C., Zhu M., Zhu Y., Zhang W., Li L. (2019). *3D-printed scaffolds of biomineralized hydroxyapatite nanocomposite on silk fibroin for improving bone regeneration*. Applied Surface Science, 467. pp.345-353.
- [11] Shi Z., Huang X., Cai Y., Tang V., Yang D. (2009). *Size effect of hydroxyapatite nanoparticles on proliferation and apoptosis of osteoblast-like cells*. Acta Biomaterialia 5. pp. 338–345.
- [12] Jusoh N., Oh S., Kim S., Kim J., Jeon N.L. (2015). *Microfluidic vascularized bone tissue model with hydroxyapatite-incorporated extracellular matrix*. Lab on a Chip, 15(20). pp. 3984-3988.
- [13] Lai Z.B., Wang M., Yann C., Oloyede A. (2014). *Molecular*

dynamics simulation of mechanical behavior of osteopontin-hydroxyapatite interfaces. Journal of The Mechanical Behaviour of Biomedical Materials 36. pp. 12-20.

[14] Lammert E., Axnick J. (2012). *Vascular lumen formation.* Cold Spring Harbor Perspectives in Medicine 2. pp. a006619 (1-9).

[15] LaValley D.J., Reinhart-King C.A. (2014). *Matrix stiffening in the formation of blood vessels.* Advances in Regenerative Biology 1. pp. 25247(1-4).

[16] Yamamura N., Sudo R., Ikeda M., Tanishita K. (2007). *Effects of the mechanical properties of collagen gel on the in vitro formation of microvessel networks by endothelial cells.* Tissue Engineering 13. pp. 1443-1453.

[17] Shamloo A., Heilshorn S.C. (2010). *Matrix density mediates polarization and lumen formation of endothelial sprouts in VEGF gradients.* Lab on a Chip 10. pp. 3061-3068.

[18] Mason B.N., Starchenko A., Williams R.M., Bonassar L.J., Reinhart-King C.A. (2013). *Tuning three-dimensional collagen matrix stiffness independently of collagen concentration modulates endothelial cell behavior.* Acta Biomaterialia 9. pp 4635-4644.

[19] Zhu W., Holmes B., Glazer R.I., Zhang L.G. (2016). *3D printed nanocomposite matrix for the study of breast cancer bone metastasis.* Nanomedicine: Nanotechnology, Biology, and Medicine 12. pp 69-79.

[20] Liu Z., Tang S., Ai Z. (2003). *Effects of hydroxyapatite nanoparticles on proliferation and apoptosis of human hepatoma BEL-7402 cells.* World Journal of Gastroenterology 9. pp 1968-1971.

[21] Chen X., Deng V., Tang S., Zhang M. (2007). *Mitochondria-dependent apoptosis induced by nanoscale hydroxyapatite in human gastric cancer SGC-7901 cells.* Biological and Pharmaceutical Bulletin 30. pp 128-132.

- [22] Li J., Yin Y., Yao F., Zhang L., Yao K. (2008). *Effect of nano and micro hydroxyapatite/chitosan-gelatin network film on human gastric cancer cells*. Materials Letters 62. pp 3220–3223.
- [23] Meena R., Kesari K.K., Rani M., Paulraj R. (2012). *Effects of hydroxyapatite nanoparticles on proliferation and apoptosis of human breast cancer cells (MCF-7)*. Journal of Nanoparticle Research 14. pp 1-11.
- [24] Dey S., Das M., Balla V.K. (2014). *Effect of hydroxyapatite particle size, morphology and crystallinity on proliferation of colon cancer HCT116 cells*. Materials Science and Engineering 39. pp 336–339.
- [25] Han Y., Li S., Cao X., Yuan L., Wang Y., Yin V., Qiu T., Dai H., Wang X. (2014). *Different inhibitory effect and mechanism of hydroxyapatite nanoparticles on normal cells and cancer cells in vitro and in vivo*. Scientific Reports 4. pp7134(1-7).

CHAPTER 9

DIFFERENT MATERIALS OF IMPLANT AFFECTING THE BIOMECHANICS BEHAVIOUR OF FIBULA FRACTURE: A FINITE ELEMENT STUDY

*Amir Mustakim Ab Rashid^{1,2} Mohamad Hafiz Mohamad Afandi^{1,2}, Gan
Hong Seng³, Mohammed Rafiq Abdul Kadir^{2,4}, Muhammad Hanif
Ramlee^{1,2}*

¹ Medical Devices and Technology Center (MEDITEC),
Institute of Human Centered Engineering (iHumen),
Universiti Teknologi Malaysia,
81310 UTM Johor Bahru, Johor, Malaysia.

²Bioinspired Innovation Group (BIOINSPIRA),
School of Biomedical Engineering and Health Sciences,
Faculty of Engineering,
Universiti Teknologi Malaysia,
81310 UTM Johor Bahru, Johor, Malaysia.

³Universiti Kuala Lumpur,
British Malaysian Institute,
Jalan Sungai Pusu,
53100 Gombak, Selangor, Malaysia.

⁴Sports Innovation and Technology Center (SITC),
Institute of Human Centered Engineering (iHumen),
Universiti Teknologi Malaysia,
81310 UTM Johor Bahru, Johor, Malaysia.

9.0 INTRODUCTION

Our body possesses skeletal system which is most crucial system. It functions as the protector of our internal organ, frame of our body and crucial in locomotion support. For example, skull act as the protector of our brain and form our face, which divides into cranium and mandible. This study focusing on lower limb which is also part of the skeletal system. Lower limb is very important in aiding our daily activities such as lifting, climbing and other locomotion movements. It was stated by United States hospitals, between 2007 and 2011, ankle has the highest number of fracture at lower limb case, which were 280,933 cases [1].

Malleolar fracture recorded as the highest ranking of occurrence among ankle fracture [1]. Extreme outward movement of foot, which is supination can contribute to the fracture which is located near to the talus and distal of fibula. Abnormal and swollen structure of ankle and hurt during walking are the symptoms of ankle fracture[1, 2]. Ankle fracture also can be easily detect using our hand.

Surgery is the ultimate solution when it comes to the ankle fracture injury[2]. Posterior lateral plating with an antiglide plate or lateral plating of the fibula with an interfragmentary lag screw were the conventional methods in treating these fractures. The surgery will result a success in using these methods if the bone density of the patient is normal. Hence, to use this method with a patient with osteoporosis which have abnormal bone density, it will lead to a failure. Compression between plate and bone will help in maintaining and gaining the stability of the fixation [3]

In treating the fracture, researchers keep searching for the best solution as the technologies rapidly evolving. Locking compression plate; one of the solutions in treating the fracture is a design consist of two different holes on the plate acting as the holder of the fractures. Different conventional-designed screw is use with this design. The stability of the implant was increased as the screw and plate have constant angle[4]. The combination of compression and locking hole was called combi hole.

9.1 FIBULA BONE FRACTURE

National Trauma Data Bank of hospitals in United States recorded that ankle fracture will contribute to fibula fracture. These accidents were assumed occur because of sports activities but most of them occurred at the street. Fibula fractures occurred because of rotational force. A ligament which hold fibula and tibia together is called syndesmosis. Danis-Weber AO Classification classified the fibula fractures into three different classes which is depending on deterioration rate of syndesmosis and the part of fibular involved in the fracture. The fibula fractures were classed into Type A, Type B and Type C. Type A fracture can be defined as a fracture which occurred at the ankle joint but does not cause any harm to the syndesmosis. Type A fracture is a transverse fracture. Meanwhile Type B fracture occurred when the fracture is involving half of syndesmosis injury and occur in a spiral fracture pattern on the fibula. Lastly, Type C fracture defined as a fracture which involve the syndesmosis injury and occurred proximal to the ankle. The classification made it easier to recognize the pattern of fracture and parts involved in the injury[5]). Figure 9.1 shows the classification of Danis and Weber of fibula fracture.

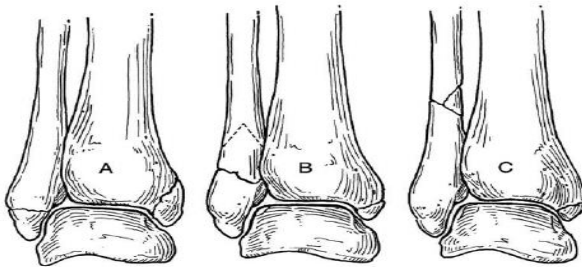


Figure 9.1: Danis-Weber Classification of ankle fractures

9.2 INTERNAL FIXATION METHOD

During an open surgery to apply the implant to the fractured area, internal fixation method was used to fix the fracture hence can improve the healing process and the anatomy of the fractured bone [6]. After certain period, the implant will be removed which allow further healing process to proceed. Structural aspects and some previous issues regarding conventional plate and locking compression plate will be discuss further.

9.2.1 Conventional Plate

Surgeon believed that the conventional plate is the best plate to be used during internal fixation method. There are many types of conventional plates which might vary depend on the location of the fracture. One-Third Tubular(OTT) Plate is the commercial name for the plate that had been used to fix the fibula fracture. This 1mm thickness plate recognized to be helpful to be imply on the area which have less soft tissue. The curve of the inside of the plate was designed for it to fit better with the bone. The length of the plate varies with the number of holes on the plate, for example 57mm length of the plate consists of 5 holes; 2 bicortical proximal screws, 2 unicortical distal screws and 3.5mm non-locking screw. Figure 9.2 illustrate the One-Third Tubular Plate applied at the distal fibula. Based on previous study, Bone Mineral Density found to be the factor of the plate failure [7].



Figure 9.2: The one-third tubular plate is applied on the distal fibula

9.2.2 Locking Compression Plate

Two types of method had been merged to assure the fitting of the locking compression plate on the bone in one design. The conventional plate differs with the locking compression plate in terms of the holes. Locking compression plate allow the surgeon to utilize the screws freely depend on the condition of the patient. Furthermore, the stability of the plate and the bone can be improved through the fixation of the angle of screw and plate. High pull-out force needs to be applied as there is locking screw and the width of the screw is 5mm. However, it is proven that this treatment, does not correlate with BMD. The application of local compression plate and the figures of hole of the screws are shown in Figure 9.3 [8].

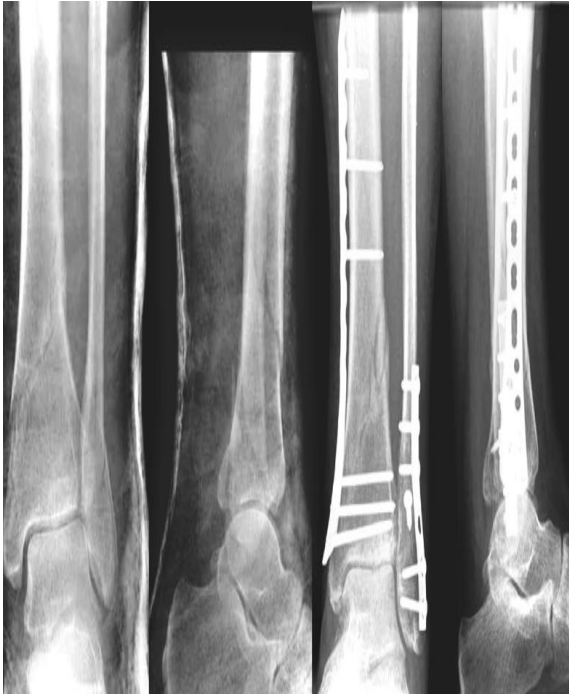


Figure 9.3: The application of LCP on the tibia and fibula bone

9.3 MODEL DEVELOPMENT

9.3.1 Development of Bone

Mimic software was used to develop three-dimensional bone (3D) model from the CT scan. The region of interest has been focused on tibia, fibula and talus. Hounsfield unit need to be altered two differentiate of two types of bones which are compact and spongy bones. Next, the noise removal process had been implied [9]. Next, the 2D images of bone will be changed to 3D images by using calculating tool. Calculating tool is been used to convert from 2D images to 3D model [10].

Meshing need to be done to the bones where the size was set at 3.0mm using tetrahedral mesh[10, 11] and imported to 3-matic for refinement process to get the best mesh size for the bone, hence contribute to accurate result during finite element analysis. Finally, STL format was used to save the model and virtual surgery will be done in Mimic[12]. Step-by-step of bone development is illustrated in Figure 9.4

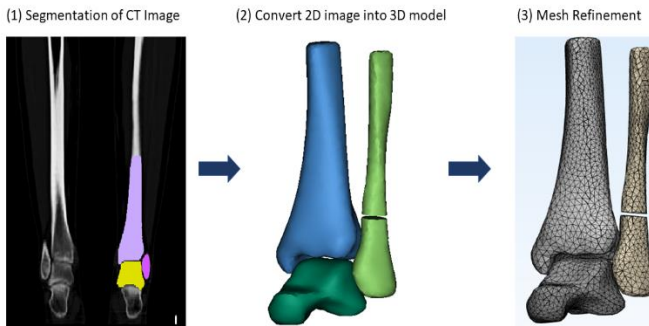


Figure 9.4: The step by step in constructing ankle bone

9.3.2 Development of implant

Both conventional plate and locking compression plate was designed using Solidwork. The plate had been constructed by referring to previous research regarding the parameters, size and distance, which follows the industry standard (Figure 9.5) [13]. The differences of the function and location of the screw will determine the design of the plate. Moreover, the displacement and the stability of the plate can be affected by the number of screws. Even the design of the plate is simple, this plate is crucial in bridging between the fractured parts and the design need to be thoroughly tested. The focus of this project is regarding malleolar fracture.

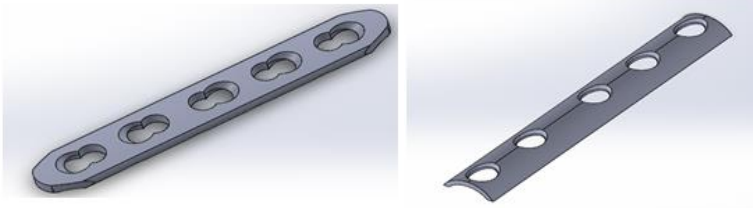


Figure 9.5: LCP and OTT plate

9.3.3 Pathological Modelling

Malleolar fracture condition was modelled for this study. Previous study found that among ankle fractures, malleolar fracture has the highest rate of occurrence[1]. Malleolar fracture consists of injuries of bones (malleoli) and, or, ligaments. Referring to the relationship of the part of the fracture, 3 types of malleolar fracture had been divided which are Type A, Type B, and Type C. Hence, for this study, Type C malleolar fracture had been chosen as it is stated this type of fracture have high rate of occurrence. Fibula and the breakage of ligament is included in this fracture; however, this study only focus on the fibular fracture. By referring to the previous studies, the result obtained still can be utilize for this project and acceptable [14]. Mimic was used to model of the malleolar fracture as shown in Figure 9.6

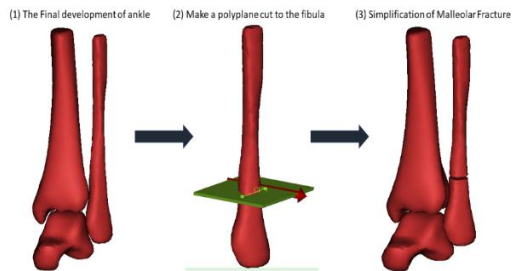


Figure 9.6: Steps of developing fibula fracture

9.3.4 Finite Element Analysis

In finite element analysis, the material properties of the bone and the implant need to be defined at the first stage. Two different materials, which are titanium and stainless steel have been applied to the plates and screws. Young Modulus of the titanium plate was set at 110 000 MPa while the properties was set to homogeneous, linear elastic and isotropic. The Poisson ratio (ν) of the titanium plate was set at 0.3. For stainless steel, the Young Modulus was set at 200 000 MPa. For bone, Young Modulus of 7300 MPa was used, Poisson ratio (ν) set at 0.3 and the properties of the bone are linear elastic, isotropic and homogeneous[11, 15]. On the other hand, axial loading is chosen to be tested on the model due to standing condition. Stiffness of 172 had been distributed to four links representing one ligament and the model was tested using axial loading. The load had been distributed equally to two legs of the patient which weight 70 kg. The load was spread to tibia (93%) and fibula (7%). Boundary condition and full finite element model is shown in Figure 9.7.

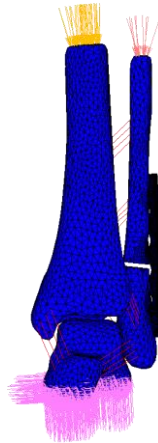


Figure 9.7: The boundary condition of finite element analysis

9.4 BIOMECHANICAL EFFECTS OF DIFFERENT MATERIALS

9.4.1 Von Mises Stress Distribution

Figure 9.8 shows von Mises Stress(VMS). During stance phases, it was founded that the titanium (Ti) model for locking compression plate yielded higher stresses at the fibula bone than the stainless steel (SS). The magnitude of pin-bone interface at the distal tibia showed a close difference during stance phases between Ti model which recorded higher magnitude of stress (70.4MPa) than SS model (67MPa). Higher magnitude of stress also recorded at the pin-bone interface at the distal tibia for Ti model (56 MPa) than the SS model (55.6 MPa)

Focusing on the bone plate, the VMS of the SS bone plate for locking compression plate model generate higher stress compared to Ti model during stance phases as shown in Figure 9.9. It was founded that the bone plate made of SS shown higher stress magnitude (1202 MPa) compared to Ti model of bone plate (667 MPa). Meanwhile, it was also recorded that magnitude of VMS at SS model (133.5MPa) was higher than Ti Model (127.5 MPa).

It was recorded that the yield strength of SS and Ti are 215MPa and 970MPa respectively. From the results obtained the design model of plate that were made from Ti is safe for both LCP and design. Meanwhile, for implant that made from SS, only OTT implant design is considered safe to be use. The evaluation made based on the peak VMS value which not exceeded the yield strength of the material which will lead to mechanical failure of the implant.

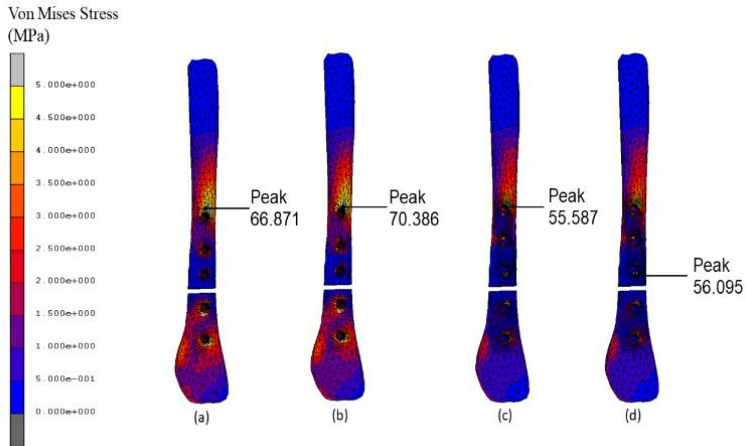


Figure 9.8: Von Mises stress contour plots at bone for a) LCP using SS, b) LCP using Ti, c) OTT using SS and d) OTT using Ti

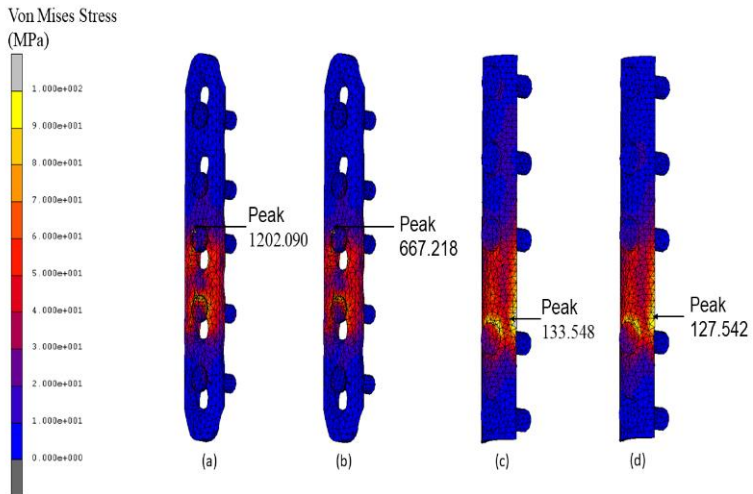


Figure 9.9: Von Mises stress contour plots at plate for a) LCP using SS, b) LCP using Ti, c) OTT using SS and d) OTT using Ti

9.4.2 Displacement

Figure 9.10 shows the contour plots of displacement of full construct for both models. The peak magnitude was observed at the proximal tibia whereas it was shown that the fixation of Ti model for locking compression plate resulted in greater displacement compared to SS model. 3.514mm and 3.513mm of maximum displacement recorded for Ti and SS model, respectively. In contrast for OTT model, higher displacement recorded for locking compression plate with fixation of SS model compared to Ti model, whereas the peak magnitude recorded at the proximal tibia. 3.75mm and 3.72mm of maximum displacement value recorded for SS and Ti model, respectively.

From the displacement results recorded, it was stated that LCP design of plate provide better stability to the bone compared to the OTT plate design. This is because there is approximately 0.2mm displacement differences between LCP and OTT design. However, further study need to be conduct in determining the stability, as the maximum displacements of the bones occurred in different area of the bone.

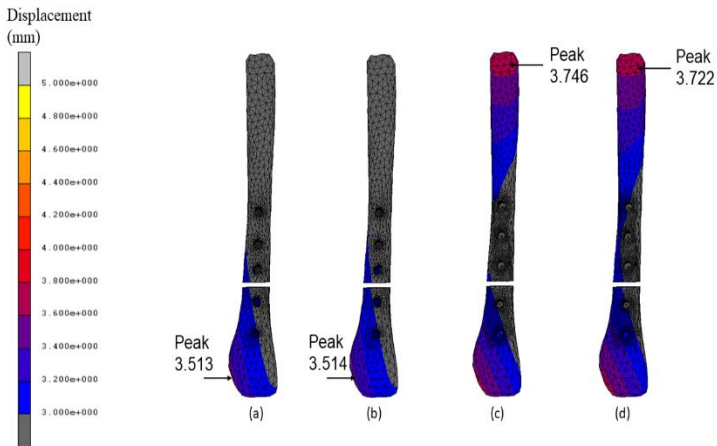


Figure 9.10: Contour plots of displacement at plate for a) LCP using SS, b) LCP using Ti, c) OTT using SS and d) OTT using Ti

9.5 CONCLUSION

This study had successfully in establishing a finite element model an ankle joint, to investigate the biomechanical properties of Locking Compression plate and Conventional Plate for treating fibula fracture and to compare the stability and stress distribution for Locking Compression Plate and Conventional Plate. From the result of this study, the finding can be further used and provide some additional information to medical surgeons on how and why on choosing a suitable plate for treating fibula fracture in terms of biomechanical aspects. This research can give a clear idea to medical surgeon on how this design functioning and affecting the patient. On the other hand, this project also can provide preliminary results to enhance the design of fibula plate based on the biomechanical overview.

ACKNOWLEDGEMENT

The authors would like thank to the Medical Devices and Technology Centre, School of Biomedical Engineering and Health Sciences, Faculty of Engineering and Universiti Teknologi Malaysia for the research facilities and laboratories. This work was financially supported by the Universiti Teknologi Malaysia under the Research University Grant (20H20, 4J358, 15J84 and 20H26), Ministry of Energy, Science, Technology, Environment and Climate Change (EF0618I1166 and 4S144) Fundamental Research Grant Scheme (FRGS) Ministry of Education Malaysia (278784-294883).

REFERENCES

1. Shibuya, N., M.L. Davis, and D.C. Jupiter, *Epidemiology of foot and ankle fractures in the United States: an analysis of the National Trauma Data Bank (2007 to 2011)*. J Foot Ankle Surg, 2014. **53**(5): p. 606-8.
2. Labronici, P.J., et al., *Medial Malleolar Fractures: An Anatomic Survey Determining the Ideal Screw Length*. Ann Med Health Sci Res, 2016. **6**(5): p. 308-310.
3. Kim, T., et al., *Fixation of osteoporotic distal fibula fractures: A biomechanical comparison of locking versus conventional plates*. J Foot Ankle Surg, 2007. **46**(1): p. 2-6.
4. White, N.J., et al., *Locked plate fixation of the comminuted distal fibula: a biomechanical study*. Can J Surg, 2013. **56**(1): p. 35-40.
5. Singh, R., et al., *Ankle Fractures: A Literature Review of Current Treatment Methods*. Open Journal of Orthopedics, 2014. **04**(11): p. 292-303.
6. Mundermann, A., D.J. Stefanyshyn, and B.M. Nigg, *Relationship between footwear comfort of shoe inserts and anthropometric and sensory factors*. Medicine and science in sports and exercise, 2001. **33**(11): p. 1939-1945.
7. Nguyentat, A., et al., *A Biomechanical Comparison of Locking Versus Conventional Plate Fixation for Distal Fibula Fractures in Trimalleolar Ankle Injuries*. J Foot Ankle Surg, 2016. **55**(1): p. 132-5.
8. Lund, J.N., et al., *The effect of insole hardness distribution on calf muscle loading and energy return during a forward badminton lunge*. Footwear Science, 2017. **9**: p. S136-S137.
9. Ramlee, M.H., et al., *Finite element analysis of the wrist in stroke patients: the effects of hand grip*. Medical & Biological Engineering & Computing, 2017.
10. Ramlee MH, S.M., Garcia-Nieto E, Penaranda DA, Felip AR, Abdul Kadir MR, *Biomechanical features of six design of the delta external fixator for treating Pilon fracture: a finite element study*. Medical & Biological Engineering & Computing, 2018. **56**(10): p. 1925-1938.

11. Raja Izaham, R.M., et al., *Finite element analysis of Puddu and Tomofix plate fixation for open wedge high tibial osteotomy*. Injury, 2012. **43**(6): p. 898-902.
12. Ramlee, M.H., et al., *The effect of stress distribution and displacement of open subtalar dislocation in using titanium alloy and stainless steel mitkovic external fixator- a finite element analysis*. Malaysian Journal of Fundamental and Applied Sciences, 2017: p. 477-482.
13. MacLeod, A.R., A.H. Simpson, and P. Pankaj, *Reasons why dynamic compression plates are inferior to locking plates in osteoporotic bone: a finite element explanation*. Comput Methods Biomech Biomed Engin, 2015. **18**(16): p. 1818-25.
14. Carroll, E.A. and L.A. Koman, *External fixation and temporary stabilization of femoral and tibial trauma*. Journal of Surgical Orthopaedic Advances, 2011. **20**: p. 74-81.
15. Ramlee, M.H., et al., *Finite element analysis of three commonly used external fixation devices for treating type III pilon fractures*. Medical Engineering & Physics, 2014. **In press**.

INDEXS

B

Biodegradable 1, 34, 74
Biomechanics 21, 35, 169
Bone 21, 165, 176

C

Calcination 40, 91, 120
Cellulose 1, 15, 121
Characterization 8, 58, 156
Collagen 2, 122, 160

D

Degradation 8, 44, 56
Dyes 37, 55, 100

E

Effect 2, 43, 102
Engineering 1, 81, 178

F

Fibula 27, 169, 180
Film 1, 87, 126
Fracture 20, 69, 175

G

Glycol 37, 60, 156

H

Hydroxyapatite 77, 153, 170
Hyperelastic 97, 101, 118

I

Implants 61, 160, 181

M

Magnesium 65, 88, 96
Material
Musculosketel 3, 8, 177

N

Nanoparticle 18, 41, 157
Nitrogen

P

Papaya 7, 88, 90
Photocatalytic 37, 59, 95
Polyethylene 23, 37, 60
Polymer 2, 64, 132
Polyurethane 20, 117, 151
Pullulan 1, 15, 19

S

Scaffold 84, 140, 160
Seed 1, 6, 139
Synthetic 3, 34, 132

T

Tensile 1, 86, 157
Thermogravimetry 1, 8
Tibia 20, 36, 180
Tissue 61, 120, 163
Titanium Dioxide 38, 49, 88

Z

Zinc Oxide 37, 49, 59